Worcester Polytechnic Institute
Digital WPI

Doctoral Dissertations (All Dissertations, All Years)

Electronic Theses and Dissertations

2018-12-05

Utilizing Compliance To Address Modern Challenges in Robotics

Selim Ozel
Worcester Polytechnic Institute

Follow this and additional works at: https://digitalcommons.wpi.edu/etd-dissertations

Repository Citation

Ozel, S. (2018). *Utilizing Compliance To Address Modern Challenges in Robotics*. Retrieved from https://digitalcommons.wpi.edu/etd-dissertations/494

This dissertation is brought to you for free and open access by Digital WPI. It has been accepted for inclusion in Doctoral Dissertations (All Dissertations, All Years) by an authorized administrator of Digital WPI. For more information, please contact wpi-etd@wpi.edu.

Utilizing Compliance To Address Modern Challenges in Robotics

A DISSERTATION PRESENTED
BY
SELIM OZEL
TO
THE PROGRAM OF ROBOTICS ENGINEERING

IN PARTIAL FULFILLMENT OF THE REQUIREMENTS
FOR THE DEGREE OF
DOCTOR OF PHILOSOPHY
IN THE SUBJECT OF
ROBOTICS ENGINEERING

WORCESTER POLYTECHNIC INSTITUTE
WORCESTER, MA
DECEMBER 2018

Approved by:

____
Prof. Cagdas D. Onal, Advisor, Worcester Polytechnic Institute

____
Prof. Gregory S. Fischer, Committee Member, Worcester Polytechnic Institute

____
Prof. Zhi Li, Committee Member, Worcester Polytechnic Institute

____
Prof. Pietro Valdastri, Committee Member, University of Leeds

©2018 – Selim Ozel
all rights reserved.

Thesis advisor: Professor Cagdas D. Onal | Selim Ozel

Utilizing Compliance To Address Modern Challenges in Robotics

Abstract

Mechanical compliance will be an essential component for agile robots as they begin to leave the laboratory settings and join our world. The most crucial finding of this dissertation is showing how lessons learned from soft robotics can be adapted into traditional robotics to introduce compliance. Therefore, it presents practical knowledge on how to build soft bodied sensor and actuation modules: first example being soft-bodied curvature sensors. These sensors contain both standard electronic components soldered on flexible PCBs and hyperelastic materials that cover the electronics. They are built by curing multi-material composites inside hyper elastic materials. Then it shows, via precise sensing by using magnets and Hall-effect sensors, how closed-loop control of soft actuation modules can be achieved via proprioceptive feedback.

Once curvature sensing idea is verified, the dissertation describes how the same sensing methodology, along with the same multi-material manufacturing technique can be utilized to construct soft bodied tri-axial force sensors. It shows experimentally that these sensors can be used by traditional robotic grippers to increase grasping quality.

At this point, I observe that compliance is an important property that robots may utilize for different types of motions. One example being Raibert's 2D hopper mechanism. It uses its leg-spring to store energy while on the ground and release this energy before jumping. I observe that via soft material design, it would be possible to embed compliance directly into the linkage design itself. So I go over the design details of an extremely lightweight compliant five-bar mechanism design that can store energy when compressed via soft ligaments embedded in its joints. I experimentally show that the compliant leg design offers increased efficiency compared to a rigid counterpart. I also utilize the previously mentioned soft bodied force sensors for rapid contact detection (≈5-10 Hz) in the hopper test platform.

In the end, this thesis connects soft robotics with the traditional body of robotic knowledge in two aspects: a) I show that manufacturing techniques we use for soft bodied sensor/actuator designs can be utilized for creating soft ligaments that add strength and compliance to robot joints; and b) I demonstrate that soft bodied force sensing techniques can be used reliably for robotic contact detection.

Contents

1 INTRODUCTION 2

2 SOFT-BODIED CURVATURE SENSOR 9
  2.1 Methods 15
  2.2 Results and Discussion 24
  2.3 Conclusion 32

3 SOFT-BODIED MODULE CONTROL 34
  3.1 Composite Soft Bending Module 39
  3.2 Experimental Results 45
  3.3 Conclusion and Discussion 50

4 SOFT-BODIED FORCE SENSORS 53
  4.1 Sensor Design and Fabrication 60
  4.2 Learning Sensor Model using a Neural Network 62
  4.3 Experimental Results 68
  4.4 Conclusion and Future Work 78

5 COMPLIANT LEG MECHANISM DESIGN 87
  5.1 Compliant Five-bar Leg Design 92
  5.2 Vertical Jump Theory and Raibert Controller 99
  5.3 System Overview 104
  5.4 Experiment Results 107
  5.5 Discussion 110

6 CONCLUSION 116

REFERENCES 133

Listing of figures

1.1 Compliant robotics, timeline. 3

2.1 Curvature sensor and soft snake. 10
2.2 Curvature sensor simulations. 17
2.3 Crosstalk simulations. 19
2.4 CAD model for molds and photo of the real curvature sensor. 20
2.5 Test platform. 21
2.6 Curvature profiles for test platform. 23
2.7 Calibration functions. 25
2.8 Static response. 26
2.9 Speed test results. 27
2.10 Speed test response without low pass filtering. 28
2.11 Peak to peak response of speed tests. 30
2.12 Error and hysteresis results from speed tests. 31

3.1 Soft, bending actuator with curvature sensor. 36
3.2 Manufacturing steps for soft bending acuator. 37
3.3 Simulated curvature sensor calibration curve. 40
3.4 Detail view of curvature sensor obtained from CAD model. 41
3.5 Sensor calibration data. 43
3.6 Bending actuator test platform. 44
3.7 Open loop response: Resistive sensor. 46
3.8 Open loop response: Hall effect sensor. 46
3.9 Step up response of modules with resistive and hall sensors. 47
3.10 Close loop response: Resistive flex sensor. 49

4.1 Tri-axial force sensor. CAD Model. 55
4.2 Manufacture steps. 57
4.3 Effect of rigid components on material compliance. 60
4.4 Experimental setup for the force sensor. 62
4.5 Validation Dataset Error Analysis 69
4.6 Force sensing results with Ecoflex 0030. 70
4.7 Force sensing results with Dragonskin 30. 71
4.8 Rectangular and pyramid shape comparison for force sensing. 72
4.9 Dynamic testing results for the force sensor. 74

4.10 Grasp with Jaco arm and the force sensor. 76
4.11 Custom robotic hand CAD model. 79
4.12 Grasp experiment snapshots with the custom robot hand. 82
4.13 Results with shear detection. 83
4.14 Results without shear detection. 85

5.1 CAD model of the hopper robot. 89
5.2 Manufacturing steps for the leg design. 91
5.3 Kinematic Diagram 96
5.4 Fivebar mechanism optimization. 98
5.5 Vertical hopper energetic. Analytical simulations. 100
5.6 System architecture. 101
5.7 Ground contact detection with tri-axial, soft force sensor. 106
5.8 Vertical hopper energetic obtained from the real platform. 114
5.9 Single jump cycle of the hopper robot. 115

Listing of tables

2.1 Root mean square errors for the curvature sensor. 30

3.1 Comparison of sensors from maximum pressure activation 48

4.1 MSE Loss in training during widening operation on Pyramidal Sensor 64
4.2 MSE Loss in training during deepening operation on Pyramidal Sensor 64
4.3 Results on the Test Dataset during widening operation on Pyramidal Sensor . . . 64
4.4 Results on the Test Dataset during deepening operation on Pyramidal Sensor . . . 65
4.5 Comparison of commercial and published force sensors along with soft tri-axial sensor design. 86

5.1 Comparison between the three different cases tested 107

Thesis is dedicated to my Dad.

Acknowledgments

First, I would like to thank Cagdas for providing mentorship, funding and the inspiring environment at the Soft Robotics Lab. This thesis would not have been written without those components. I also would like to thank my committee members Zhi Li, Pietro Valdastri, and Gregory Fischer for their valuable comments and taking their time to read through my thesis.

My friends at Worcester Polytechnic Institute, Soft Robotics Lab, Boston, Worcester and back in Istanbul supported me both professionally and personally. I would like to thank all of them. I was fortunate to work with great colleagues at Freefly Systems at the third year of my PhD for an internship and again at the last part of my PhD. I would like to thank everyone over there for their support. I would also like to thank my friends Emre Eskimez, Behnam Partopour and Junius Santoso for their thoughtful comments and feedbacks on the final draft.

Finally, I would like to thank my Mom, uncle, brother and sister in law for their never-ending support in every path of life.

Contents

1

Introduction

Robotics is a new field and making robots more agile and safe to interact with is one of its open research areas. It is useful to overview the history of robotics in order to thoroughly comprehend how the field has progressed towards developing more agile robots. The field has not truly existed until the second half of the twentieth century. Although there are historical machines that are occasionally presented as early examples of robots, such as the toy horse machine[76], one of the first papers

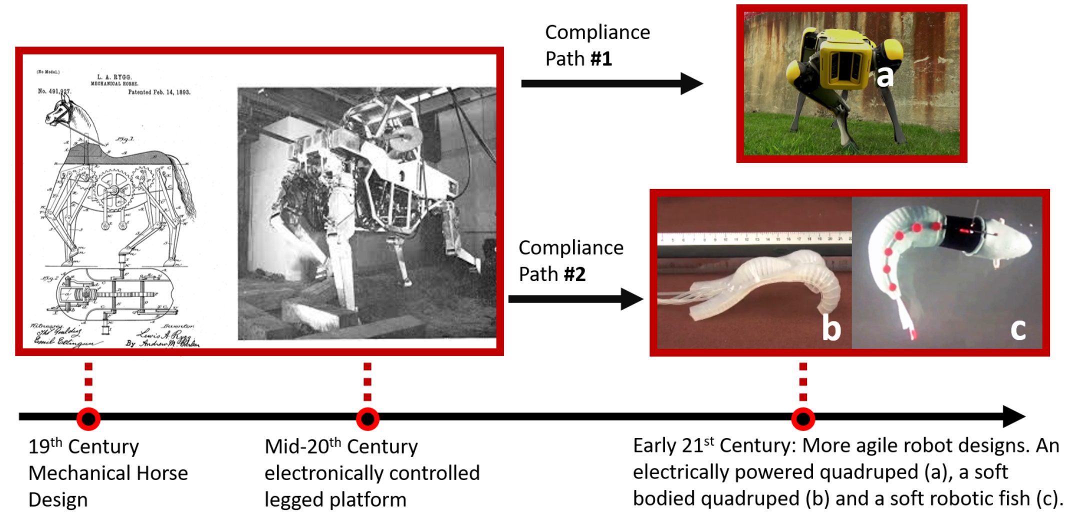
Compliance
Path #1
a
Compliance
Path #2
b
c
19th Century Mechanical Horse Design
Mid-20th Century electronically controlled legged platform
Early 21st Century: More agile robot designs. An electrically powered quadruped (a), a soft bodied quadruped (b) and a soft robotic fish (c).

Figure 1.1: Left: A mechanical horse design. Horse-like motion is achieved through complicated usage of gearboxes and mechanisms. Unfortunately such a mechanism would only have a single mode of operation and it would create routine motions. Middle: One of the first trials in making robots more agile is by combining mechanical leg designs with control electronics. Right: Two different paths to creating agile robots. Path 1 utilizes high quality electrical actuation with precise motion planning and Path 2 utilizes soft material design in smart ways.

explicitly mentioning electronic control of multiple actuators for manipulation and locomotion is published in 1969[63]. Figure 1.1 shows a brief history of robotics, emphasizing on the trend to create agility via two paths: Path-1 is an introduction of compliance via motion planning and electrical drive trains with high torque/velocity bandwidth, and Path-2 is to introduce agility via new material design techniques. Two examples in the right bottom part of Figure 1.1 use extremely soft materials to achieve new types of agile robotic motion.

Before going further into details, it is also beneficial to think about why robotics has taken off in the last decades and how compliance can help to achieve even more. It is possible to think of historical mechanical machines as predecessors of modern robots but I tend to think that this is misleading. There is the problem of computation. Without silicon-based chip technology, it is not possible to pack enough processing power to make a machine control its movements, sense its environment, and reason at a high level about its tasks. Therefore, without the computational power there is no connection between mechanics and electronics of the system. The nineteenth-century industrial revolution was based on machines that either had mechanical or steam based feedback loops and these machines were designed at the factory to do one thing well. Compare that to our PCs, which can allow us to trade online, write books, listen to music, or communicate. Only through the integration of computational power with mechanics, we have seen the first examples of what one might call robots.

A fundamental question can be framed as follows: With the increase of computational power why aren't we seeing more capable robots? Today, we have microcontroller units clocked at 400 MHz that are small enough to be packed inside human-sized robots. It would be possible to attach a high-frequency microcontroller not just to each robot but to each joint/actuator of every robot. We are capable of creating amazingly fast, distributed robotic control systems. Each one of these microcontrollers could run video games of the 1990s while performing mission-critical functionality at the same time. Unfortunately, an increase in processing power did not translate directly into making robots more capable. The question this thesis asks is how we can benefit from material properties to improve the agility of modern robots given that we have enough processing power.

I believe that mechanism stiffness, compliance, and flexibility are parts of the answer to creating more agile machines. One reason for this is that we do not have a clear understanding of how much of what humans and animals in nature achieve is due to computational power and how much of it is due to mechanism properties. For example, the rainbow trout[3] swims upstream even when it is dead, so it certainly does not compute a complex motion trajectory and it cannot execute a set of motor commands. To swim upstream, it amazingly relies on complex environmental dynamics and compliance coming from its own body configuration.

Another example comes from two different schools of thought in legged robotics. Zero Moment Point[96] (ZMP) based walkers versus dynamic walkers/hoppers inspired by Raibert[74]. The ZMP is a precise and computationally heavy approach. One needs to find a stable set of ZMP trajectories and then map them to the robot's center of mass positions and eventually obtain actuator commands from the stable mapping. This approach works but usually comes with mechanistic and inefficient locomotion patterns. On the other hand, Raibert's hoppers utilize a linear spring, which is the compliant part in the mechanism, to reason about how much the robot body would travel during stance period to compute foot trajectories. This computationally simple approach works remarkably well for creating dynamic legged machines.

We also have the emerging trend in completely soft-bodied robots. These are machines that use, most of the time, quite simple control algorithms to achieve seemingly complex tasks. Achieving fish-like escape maneuvers using soft-bodied actuators is one example[64,95,52,100]. If one looks at the examples out there, it seems agility emerging from robot compliance is a good direction to start searching for smarter robots. Throughout the thesis, I will walk the reader on how I used my practical and theoretical knowledge in building compliant mechanisms to create soft-bodied modules and integrate novel material designs into existing robotic systems and control algorithms.

At this point, it is convenient to write about how I became interested in compliance in robotics, too. I started academic research by working on a completely rigid bipedal robot named SURALP[22].

The mechanism had 29 independent degrees of freedom driven by brushed DC motors attached to gearboxes. It is not very hard to imagine how such a machine would create artificial and non-compliant motions. Some of the rigidity comes from mechanical design and some from the algorithm that forces the system to track believed-to-be-stable state trajectories via high gain tuning of brushed gearbox motors. Looking back now, these type of robots were the exact opposite of what I worked with for my doctoral research. However, having first-hand experience with them led me to think about the problem of compliance in robotics for the first time.

When I arrived in the Soft Robotics Lab at Worcester Polytechnic Institute, I shifted my research direction. Instead of rigid components, I was working with soft polymers: Trying to embed electronics into them for measurements and trying to figure out different ways to actuate them and eventually control them. The main reasoning behind compliant mechanisms was the hope that we could achieve what was difficult or even impossible to accomplish with rigid bodies. As an example the snake built in the Soft Robotics Lab (SRL) at Worcester Polytechnic Institute (WPI) would create undulatory[47] locomotion with simple open-loop valve on-off signals. Traditionally, such motions would be much harder to replicate with standard robotic parts. Not surprisingly, during the first part of my PhD, I worked on improving the control architecture of the newly developed snake system. I developed soft-bodied curvature sensors that could be embedded into the snake system for real-time sensing[68]. One of the claims of the proposed sensor was its ability for feedback control of each individual soft snake module. I demonstrated experimentally that it was possible to do feedback control with the soft sensors by mapping the data from the sensors as pulse width modulation (PWM) duty cycles to the valves[69]. Finally, we showed in the lab that multiple modules could be cascaded to create an autonomous soft-bodied snake[46].

Personally, I thought combining my hands-on experience with both soft robotics and legged locomotion could give me a chance at solving the problem of introducing agility into robotics. I was impressed by Marc Raibert's original control algorithm developed for single legged hoppers and how it utilized compliance to its benefit. A spring attached to a rigid leg and a hip actuator, as it turns out, was all the required actuation hardware to achieve impressive dexterous jump/run patterns. The controller running inside the original hopper is very simple. One could code it in less than 200 lines and make it work, assuming the hardware is functional.

So I started thinking about how to make use of my skills in soft robotics to make an advancement in dynamic locomotion. Soon, I figured soft-bodied manufacturing and soft-bodied sensing work I have conducted so far could be useful in two points: a) A soft-bodied force sensor that is fast enough to handle high frequency impacts during hopping b) A compliant leg mechanism manufactured via methods quite similar to what I use for building the soft sensors/actuators.

The result of my work was a hopping platform built with off-the-shelf electronic components. It included a fivebar mechanism manufactured via folding a polyethylene terephthalate (PET) sheet. The folded mechanism was reinforced with fiberglass mat to increase its strength. The introduction of fiberglass mat with a certain resin I used also created the compliance that was also needed in the original Raibert hopper. As opposed to a robot leg manufactured with rigid materials and a discrete mechanical spring, compliance introduced by the folded leg design came with reduced overall weight. Finally, I demonstrate experimentally, the effect of passive compliance on the hopping efficiency of the mechanism. The folded fivebar mechanism, which is functionally the leg of the system, introduces efficiency at a lower weight.

The contributions of each chapter to the academic body of robotics literature can be summarized as follows:

- Robust and precise curvature feedback with rapid response for soft-bodied robots.
- Feedback control of soft bodied bending segments.
- Tri-Axial force measurements via soft bodied mechatronics design for grasping and ground contact detection
- Utilization of soft bodied material design for manufacturing an extremely lightweight hopper leg design
- Efficiency benefits of the compliant leg design.

The rest of the thesis is organized as follows. First, I write about details of soft-bodied sensing, actuation, and control based on the work I have done. The soft-bodied curvature sensor and control of a soft-bodied segment are shown in Chapters 2 and 3. The soft-bodied force sensor, which is an extension of the magnetic sensing idea I utilized in the curvature sensor, is presented in Chapter 4. Finally, the compliant leg mechanism and the hopper platform is presented in Chapter 5. This mechanism uses the soft force sensors for high frequency contact detection, and its leg mechanism is inspired by the ideas I learned while building soft-bodied modules. For the conclusion, I will discuss the state of soft and compliant robotics, how my work contributed to the field and my thoughts on the future of the field.

2

Soft-Bodied Curvature Sensor

Soft-bodied robots are interesting but they are not capable of achieving a wide range of useful tasks. This is not because they are inherently incapable of achieving them and the reason can be likely attributed to the fact that we as humans and as engineers like to linearize things and try to find solutions to linearized versions of complex problems. Sometimes this approach works remarkably

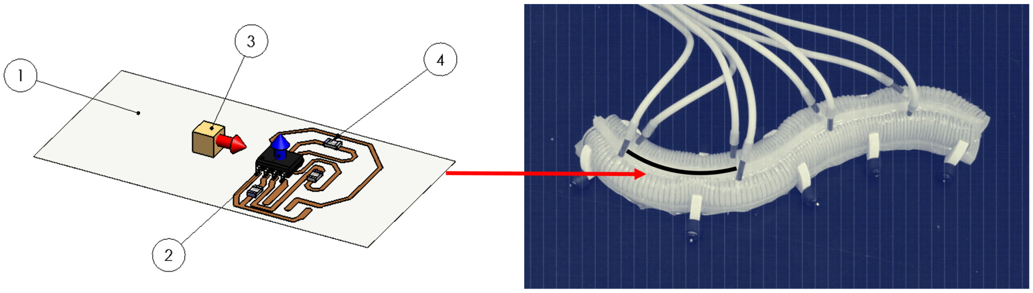

Figure 2.1: The soft-bodied snake robot design, which is completed by a group of students working in WPI Soft Robotics Lab, is shown. Curvature sensors are embedded in each soft module for sensing robot configuration. The platform I designed in SRL allowed me to address the design challenges in extremely flexible mechanisms and paved ground for introducing a hall sensor based curvature sensor design. Left: Computer Aided Design of the sensor assembly is shown. Number definitions: 1) Flexible substrate, 2) Hall effect IC, 3) Magnet, 4) Circuit paths and components. Red and blue arrows indicate horizontal (x-axis) and vertical (y-axis) directions respectively. Right: The sensor is built to be integrated into the middle of the soft snake robot for proprioceptive curvature measurements.

well: As in designing a 7 DoF robot manipulator and linearizing its dynamics and inversing them in real time so the controller can cancel them out and the control engineer can write the equation governing the motion of the mechanism. This is the fundamental idea behind many, if not all industrial robots, working in the real world. It does not work well with more organic designs, as of today.

The snake robot in Figure 2.1 is one example where a well engineered approach is not found for control purposes. We do not know how to model continuously deformable dynamics as well as we know how to write the Lagrangian function of atomically discrete sets of masses. Even if we had a set of dynamics equations we could understand and manipulate, we are further constrained by lack of actuators and sensors that can be integrated into them. Not surprisingly, my first work when I arrived in Soft Robotics Lab was to design a sensor for the snake robot[68] that could replicate the functionality of an encoder in a traditional robot.

As it turns out, obtaining kinematic configuration information of soft-bodied robots is one of the current challenges in the field. The traditional approach to determine the configuration of a rigid kinematic chain is to obtain discrete angle measurements from each joint. In contrast, soft-bodied robots possess indefinitely many passive degrees of freedom [91,78] as a result of continuously deformable segmented bodies [29,45], emphasizing the need for new sensing techniques.

This chapter explores the capabilities of a novel embedded soft curvature sensor designed to capture configuration information from soft robotic bending segments [68]. It is equally important to mention that constant curvature assumption for individual bending segments hold true under certain assumptions. Fro example, if we were to include 3D motions, as opposed to planar motions in the snake robot, a single curvature value for each segment would not be enough to determine the shape of the segment. As mentioned in the opening, the emerging field of soft robotics suffers from a lack of modeling and control efforts for both kinematic configuration and dynamic properties. Soft manipulators and soft-bodied mobile robots can expand their capabilities through accurate models, and corresponding feedback controllers. For example the octopus arm [12] could utilize high resolution curvature/spline sensors attached to its tentacles. Similarly, the soft manipulator [51] can utilize curvature sensor attached to its segments. Eventually, robots with soft segments [80,42,87] can improve their autonomy by improved sensing technologies. Inspired by the approach to model the configuration of a soft robot based on defining the bending deformation of soft segments as curvatures [45,65,50] instead of discrete angles I present a curvature sensor for soft-bodied modules. When one thinks of a soft module in this way the orientation and position of every point on a continuously deformable segment becomes uniquely defined with respect to its curvature. Robot configuration is then modeled as a kinematic chain of segments, where each segment is defined by a single curvature value. In prior work, my colleagues in SRL were able to model and reproduce lateral undulation for a soft robotic snake comprising four soft bidirectional bending segments[47,65].

Encouraged by the preliminary work, my early research[68] details the design, fabrication, and experimental verification of a soft curvature sensor comprising a miniature magnet and a Hall effect measurement integrated circuit (IC). The magnet is positioned in a specific way with respect to the Hall element on a flexible circuit (see Figure 2.1) to measure the curvature of bidirectional out-of-plane deformations in a standalone package, without the need for external electronics. This is a versatile approach, which can be adapted to measure other physical deformations in a soft body. For example, a setup consisting of a magnet mounted over a Hall Effect sensing component can be used for measuring normal forces. In this work, I focus my attention to curvature sensing due to its practical applications on the soft robotic snake[47,65].

Hall elements are compact, accessible, and inexpensive. The quick response (less than 10 microseconds is listed as response time for MLX91207) and accuracy of Hall elements for traditional robotic applications have previously been verified for joint angle proprioception[7,18] as well as tactile exteroception[90,31]. Contact-free sensing capabilities are highly desired for soft robotic research[17]. Thus, a unique advantage of my non-contact magnetic field measurement approach is its negligible effect on material stiffness. As a trade-off, isolating the magnetic field generated by the magnet is a challenge to be considered during design. Industrial designs guarantee this by isolating the sensor and magnet couple mechanically.

Alternative solutions to curvature sensing include commercial resistive flex sensors, optical fiber Bragg gratings, and embedded liquid metals. Resistive flex sensors offer a compact and straightforward solution for embedded sensing in soft robotics. Nevertheless, I conclude that they suffer from dynamic artifacts, such as delayed response and drift.

Optical fiber Bragg grating is a powerful sensing solution for deformable bodies which is used successfully for force measurements on a soft finger[70], and shape reconstruction[99]. Fabry-Perot interferometer based curvature sensors[58] are also an option for optical curvature sensor measurement. Although these technologies facilitate highly accurate curvature measurements using a thin and flexible optical fiber, the required supporting hardware disables embedded operation especially for tetherless mobile robots with many degrees of freedom.

A novel and specialized sensor technology for soft robots is the use of liquid metals embedded in rubbers, a technology stemming from mercury-in-rubber strain gauges[27]. Thus, dimensional changes due to deformations in the substrate are reflected as resistance changes by the liquid metal. Recent work incorporates fluidic channels inside silicone rubber filled with eutectic Gallium-Indium (eGaIn) to measure joint angles of a finger[37] and for a tactile sensing array[38]. The eGain sensing has matured and there exists a short survey on sensors[94]. An interesting work that applies eGaIn sensors to a suit for gait detection was published[56]. Main limitation of eGaIn sensor is a relatively complicated fabrication phase. They require a 3D mold with channels. Afterwards eGaIn is injected from one side of the mold while air inside the channels is vacuumed from the other side. Thus, repeatability and complexity in manufacturing these sensors may be a challenge.

To address the fundamental challenge of providing accurate and dynamic proprioceptive feedback for soft-bodied robots, this chapter proposes a novel soft curvature sensor, based on the state of the art in flexible sensing technologies. Specific contributions of my work were as follows:

- Robust and precise curvature feedback with rapid response for soft-bodied robots.
- Integrated measurement of kinematic configuration for soft-bodied arms and mobile robots composed of soft bending segments.
- A custom test platform for soft-bodied curvature sensors.

Nearly two years after publishing my work on curvature sensors, I observe the following: First, I think generating magnetic fields inside soft materials is a strong medium for sensing flexible body configuration. The same idea is actually proven to be quite useful in industrial applications where a magnetic field is utilized via encoders to measure absolute joint angles. Second, the knowledge obtained for manufacturing composite for materials can be adapted to different sensor designs; furthermore, it can be used to create multi-material compliant mechanisms as well. These implications are discussed in the following chapters of the thesis.

The following section explains the fundamentals of design, modeling, and fabrication. I provide detailed information on positioning of the magnet-sensor pair, design specifications, and manufacturing steps. I also present results of numerically simulating the sensor response to different curvatures. The simulation results inform the positioning of discrete elements, gain and offset adjustment. I present a test platform to repeatably characterize and verify soft curvature sensors under static and dynamic loading conditions. Section 2.2 displays and discusses results obtained from the proposed curvature sensor using the custom test platform, reporting experimental results on calibration, repeatability, as well as static and dynamic verification of the proposed soft curvature sensors.

2.1 METHODS

2.1.1 CURVATURE SENSOR DESIGN

The main requirements for a curvature sensor for soft robotics are flexibility and minimal effect to material stiffness. Along with structural specifications, accurate, precise and fast responses are also required for feedback control applications based on proprioceptive curvature sensing.

I adopted locomotion parameters of a soft-bodied snake robot[45] as a set of design specifications to achieve an embedded curvature sensing module that is consistent and compatible with the literature. The soft robotic snake deforms between 0.2 cm^{-1} and 0.4 cm^{-1} and the frequency of traveling curvature waves to achieve undulatory locomotion is around 2 Hz. Thus, a curvature sensor working at frequencies above around 3 Hz without dynamic attenuation is expected to provide an accurate reconstruction of the robot configuration.

An accurate mapping is required to convert measurements to curvature values. Two desired properties of the calibration function are linearity and injectivity. To show that such a mapping exists, I developed a simulation platform that considers both finite element analysis of a magnet and its theoretical model. Once the sensor is calibrated, and a mapping is obtained, curvature measurements are absolute (i.e. not subjected to initial conditions or temporal variations).

Theoretical modeling of magnetic flux density vectors around a magnet provides intuition on the curvature sensor response. A simple dipole model of magnetism approximates these vectors, but it does not include volumetric constraints. A more accurate 2-D analytical model of a rectangular magnet also exists[1]. According to this model, the Cartesian magnetic field vector components in the magnet frame can be written as:

$$B_x(x,y) = \frac{\mu_0 M_s}{2\pi}\left(\arctan\frac{2h(x+w)}{(x+w)^2+y^2-h^2} - \arctan\frac{2h(x-w)}{(x-w)^2+y^2-h^2}\right), \tag{2.1}$$

$$B_y(x,y) = \frac{\mu_0 M_s}{4\pi}\left(\ln\frac{(x+w)^2+(y-h)^2}{(x+w)^2+(y+h)^2} - \ln\frac{(x-w)^2+(y-h)^2}{(x-w)^2+(y+h)^2}\right). \tag{2.2}$$

In the equations above, B_x and B_y are magnetic flux density vector components in different (x, y) positions with respect to the magnet. The coordinates and the origin of the frame, in which equations are defined, can be seen in Figure 2.2. X-axis and Y-axis are parallel to horizontal and vertical lines respectively, and the origin of the magnet frame is attached to the middle of the cube magnet. μ_0 is the relative magnetic permeability of the medium. M_x is the surface magnetization magnitude of the magnet. Finally, h and w are the height and width of the rectangular magnet.

To maximize accuracy, I used the magnetic flux density vector data obtained from finite element analysis (FEA), using the COMSOL package, to develop a kinematic simulation within the working range of the sensor. COMSOL allows users to model magnets with respect to remnant magnetic induction. Also, it is trivial to get a 3D surface with magnetic flux density vectors around the magnet. Figure 2.2 displays magnetic field density vectors around a magnet along with the trajectory covered by the Hall element during the simulation. The design space of this sensing approach comprises multiple parameters such as: magnet size and orientation, the distance between the sensor and the magnet, and the sensitivity of the Hall element. For example, if the magnetization axis of the magnet is not perpendicular to sensing direction, the mapping from voltage to curvature would not be bi-

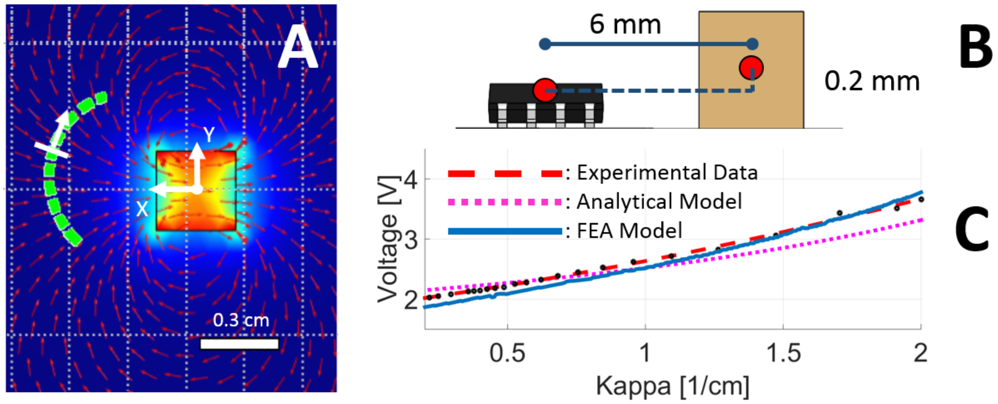

Figure 2.2: (A) FEA data obtained from a simulation of sensor motion. The dashed green curve is the trajectory of the sensor from $-1.5\ \text{cm}^{-1}$ to $1.5\ \text{cm}^{-1}$. Arrow indicates the sensing direction that is always tangential to the trajectory. An inherent offset due to vertical level difference between magnet and sensing surface can also be observed from the mid-point of the trajectory. (B) shows the vertical and horizontal offset between the magnet and the sensor. (C) Sensed magnetic flux density vector magnitude was computed between $0.5\ \text{cm}^{-1}$ and $2.0\ \text{cm}^{-1}$. The dashed red curve is a least squares fit obtained from voltage measurements from 30 different curvatures. The solid blue curve is the voltage versus curvature result from the FEA simulation. The dotted purple curve is the simulation result obtained from the theoretical model between $0.5\ \text{cm}^{-1}$ and $2.0\ \text{cm}^{-1}$. Both in simulations and in the application, I use a cube magnet with a side length of 3 mm. The magnetization value for simulations is $8.0\text{x}10^5$ A/m.

directional. This numerical approach provided us with rapid evaluation of all design parameters to serve as preliminary values for fabrication.

I exported the FEA data to MATLAB as a lookup table for magnetic flux density vectors at different positions around the magnet. The position of the Hall element with respect to the magnet is a function of curvature expressed as:

$$\begin{aligned} x &= \frac{1}{\varkappa}\sin(\varkappa s), \\ y &= \frac{1}{\varkappa}(1-\cos(\varkappa s)), \end{aligned} \tag{2.3}$$

where x and y are positions along the length of the segment, κ is the curvature of the segment in cm^{-1} units, s is the normalized arc-length, $s \in [0, 1]$[65]. x and y positions are defined in the magnet frame and axis representations can be seen in Figure 2.2. The Hall element measures the magnetic flux density vector component in the perpendicular direction to its surface, which is taken into account in the both analytical calculations and numerical simulations.

Figure 2.2 displays simulated magnetic flux density vector magnitude on the Hall element for curvature values between 0.2 cm^{-1} and 2 cm^{-1}. The horizontal distance between magnet and sensor in this simulation was picked as 6 mm and the vertical distance was picked as 0.2 mm. The horizontal distance was obtained by looking at the simulated and the real sensor data making sure distance between sensor and magnet is small enough while not saturating the voltage measurements. The vertical distance emerged from the package of the sensor and the size of the cuboid magnet. Horizontal and vertical distance definitions can also be seen in Figure 2.2. Results from this simulation suggest that there exists a one-to-one, nearly linear mapping between the measured component of the magnetic field vector and curvature.

Sensitivity and offset of the magnetic field measurement circuitry depend on the positioning of the magnet, as well as the vertical distance between the magnet and the Hall element. Simulation results suggest that the sensitivity of magnetic field measurement should be around 40 mV/G, to utilize 70 % voltage range between $0 - 5$ V in positive and negative directions. Due to directional bias, a voltage offset of 0.35 V was added to achieve bi-directional measurement without saturation.

I also looked into the effects of crosstalk between other sensors or ferromagnetic materials in the environment inside the simulation. I placed another magnet at three different distances in the

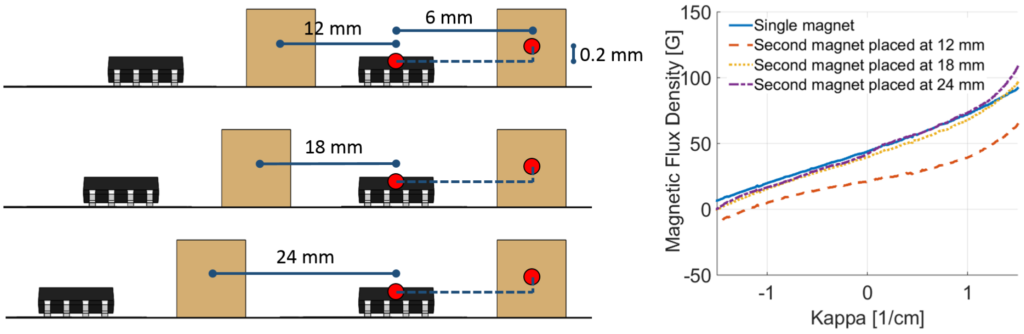

Figure 2.3: A second magnet is placed at distances 12, 18, and 24 mm near the Hall element to analyze the effects of a cascaded sensor system. Results suggest that another sensor pair can be placed at 18 mm, and it will not create significant interference in the sensed magnetic flux density. The sketch on the left is not to scale.

horizontal direction and observed their effect on the Hall element. The horizontal distance between the surface layer and the magnet is 6 mm. Through simulations, I discovered that crosstalk between sensors might become an issue when another sensor is placed between 12-18 mm. I also discovered that crosstalk has an effect on measured data in high curvature values around -1.5 cm^{-1} and 1.5 cm^{-1}. Results can be seen in Figure 2.3.

2.1.2 Manufacturing

Manufacturing of the curvature sensor is composed of two stages: printing electronics and molding silicone rubber. Electronic circuitry is printed on two substrates, copper-clad FR4 and copper-foil laminated polyester, using a standard solid-ink printer. The flexible substrate is then etched to obtain circuit traces and discrete components are populated manually to result in a fully custom-printed flexible circuit. The Hall Effect IC is AD22151. A B222G-N52 magnet is bonded to the etched sheet at the desired location based on my simulation results.

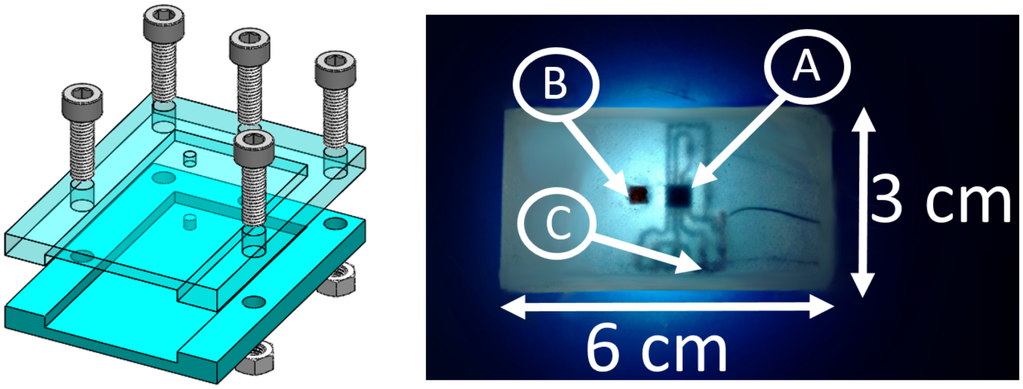

Figure 2.4: Left: Isometric view of the mold is shown. Silicone rubber is poured into the inner chamber from the open space that can be seen in front and isometric views. The length, width and thickness of the inner chamber are 60 mm, 30 mm and 5.6 mm respectively. The length, width and thickness of the overall mold are 50 mm, 70 mm and 11 mm, respectively. Right: A curvature sensor prototype is shown. The Hall effect IC (A), the magnet (B), and circuit traces (C) can be seen in the figure. A flexible circuit layer is positioned in the middle of the silicone layer. The Hall effect IC has an internal op-amp for offset and sensitivity adjustments. Circuitry and resistances are also embedded inside the silicone. The total thickness of the sensor is 7 mm.

For greater compatibility with bending type soft actuators, the curvature sensor circuit is embedded inside EcoFlex 0030 silicone rubber from Smooth-On. The choice of material was made by considering the material choice for the soft snake robot, which is also EcoFlex 0030. It is possible to use another soft silicone, such as Dragon Skin, as well. Although mixing soft materials with different tensile strengths will create different dynamic behaviors when they are actuated via air pressure. 3-D printed mold design for the sensor is shown in Figure 2.4. Screws passing through the flexible sheet and two pieces of the mold guarantee the flat mounting. Silicone rubber is then introduced inside the mold and cured at 60 °C for 40 minutes. The curing operation finalizes the manufacturing of the sensor. An example of the soft sensor segment can be seen in Figure 2.4.

Provided with electronic components, circuit design, and molds; overall manufacturing time to

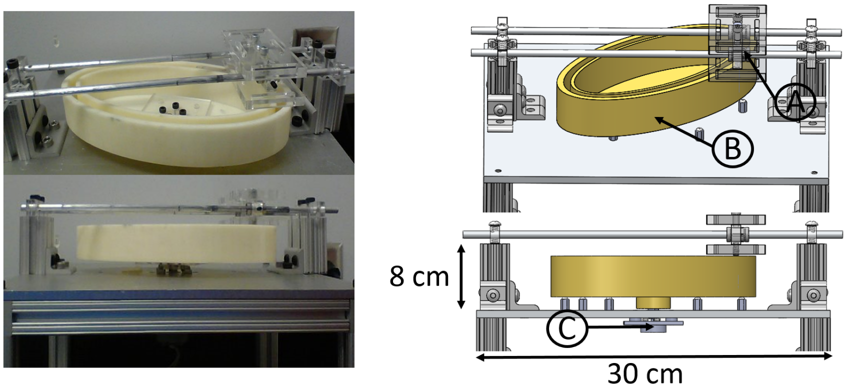

Figure 2.5: Left Panel: Actual test platform with the ellipse track is shown. Right Panel: CAD models of the platform are shown. (A) is the mounting platform for the sensor. It can move in a single direction along the aluminum rods. The connection is made with linear bearings to reduce friction. There is a rod coming down from the platform that is attached to the sensor. This rod pulls the sensor inside the track as the motor turns it. (B) 3D printed elliptical track. (C) A motor is mounted below the square shaped aluminum platform and it is coupled to the 3D printed track. The edge length of the platform is 30 cm. The thickness of the elliptical track is 4.5 cm including the motor coupling.

build the sensor from scratch is approximately two hours. Printing circuit traces and etching takes 30 minutes. Components can be manually soldered in under 15 minutes and curing silicone rubber takes around 40 minutes. Note that all these processes can be automated and performed in parallel to speed up the manufacturing process for larger volumes.

2.1.3 TEST PLATFORM

Deforming a silicone rubber segment into known curvatures, repeatedly and precisely is not a trivial task. One way to achieve it is to attach soft bending actuators[65] powered by pressure to the sensor segment, and actuate it with different pressure values. The deformation could be tracked with a visual system to compute the curvature of the segment.

A test platform composed of a soft actuator and sensor segment is undesirable. Pneumatic soft actuators typically possess relatively low bandwidth. Therefore, it constitutes a bottleneck for measuring dynamic responses of the sensor. Moreover, the magnet-Hall couple requires precise and repeatable calibration. Using soft actuators would introduce unnecessary complexity during the calibration phase.

To calibrate the sensor independent of external effects, and verify its static and dynamic response, I consider a custom test platform shown in Figure 2.5. Form-closed modular tracks that constrain the sensor segment to deform into exactly known curvature values are designed. The tracks can be rotated to desired angles or at desired velocities by a DC motor. A platform on top of the track holds the curvature sensor on a pin (see Figure 2.5), which pulls the sensor as the track advances.

The sensor needs to be deformed into known curvature values and kept at those values for calibration. For this task, I use an Archimedean spiral track and conduct static curvature tests. To verify accuracy and precision under dynamic curvature waveforms, I use an elliptical track. Figure 2.6 shows the spiral and ellipse plots along with their CAD models.

The curvature on any point on the spiral and the ellipse can be obtained by (2.4) and (2.5), respectively. Here, a and b are standard ellipse and spiral parameters, $\vartheta \in [-\pi, \pi]$ is the angle of rotation around the center, and $t \in [-\pi, \pi]$ is a parametric variable for the ellipse, where $\tan(t) = (a/b)\tan(\vartheta)$. Simultaneous angle measurements were taken to calculate the expected curvature values during all experiments. The spiral track was used to collect data points for calibration, and for static response tests. Dynamic response tests were performed with the elliptical track.

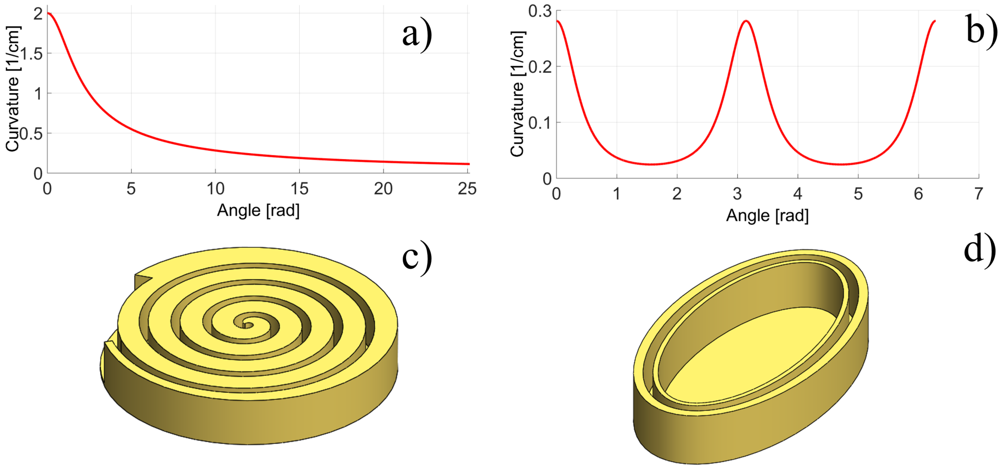

Figure 2.6: Curvature profiles inside spiral and ellipse are shown as functions of an angle in a) and b). The spiral parameters are $a = 15$ cm and $b = 35$ cm. Parameters for ellipse are $a = 10$ cm and $b = 5$ cm. Standard polar equations for spiral and ellipse are used for calculations. Solid surface models of the shapes are given in c) and d). Curvature profiles are passing through the midpoint of paths in both solid surface models.

$$\varkappa_s = \frac{1}{\sqrt{a^2 + b^2 + b^2\vartheta^2 + 2ab}} \tag{2.4}$$

$$\varkappa_e = \frac{ab}{[(b\cos t)^2 + (a\sin t)^2]^{3/2}} \tag{2.5}$$

A Maxon graphite brushed 200-W DC motor with 81:1 reduction was used for calibration. Accurate tracking was obtained with a 500-counts-per-turn optical encoder. Controller for this motor was programmed in an Arduino UNO board. Reference speed and angle values can be given to the controller through a user interface running on a PC through serial communication. PC-side user interface, and serial communication were programmed in Processing.

For speed tests, a 50-Watt motor with 19:1 reduction was used. An optical encoder with 64 counts per turn was used for tracking the angle. For analyzing the dynamic response of the sensor, the elliptical track was turned under different speeds in open loop, using a constant voltage input to the electric motor. Data from the soft curvature sensor and motor encoder was obtained through an NI SCB-68A board. The sampling rate of data acquisition was 10 kHz.

Spiral and elliptical tracks are made of 3D printed ABS tracks. Initially, I performed tests with Ecoflex as the contact surface with the ABS tracks. This choice resulted in high friction. To overcome this issue I covered the sensor segment with 12.7 μm thick PET film and used industrial grease to further reduce friction.

2.2 RESULTS AND DISCUSSION

This section discusses my results from calibration, static loading and dynamic loading cases. I also give out characterization data of the proposed sensor design in Section 2.2.4.

2.2.1 CALIBRATION

Based on simulations and previous experimentation with the sensor, the horizontal distance between the magnet and Hall element was set as 6 ± 0.5 mm. The vertical distance between the center of the magnet and the surface of the Hall element was dictated by the components to be approximately 0.2 mm. Horizontal and vertical distances can be seen in Figure 2.2. I also verified the static response of the curvature sensor using the test platform as a tool for automated calibration.

For automated calibration, sensor is driven to 30 points with different curvatures inside the spiral. This process was repeated three times for accuracy. A non-linear least squares fit was obtained

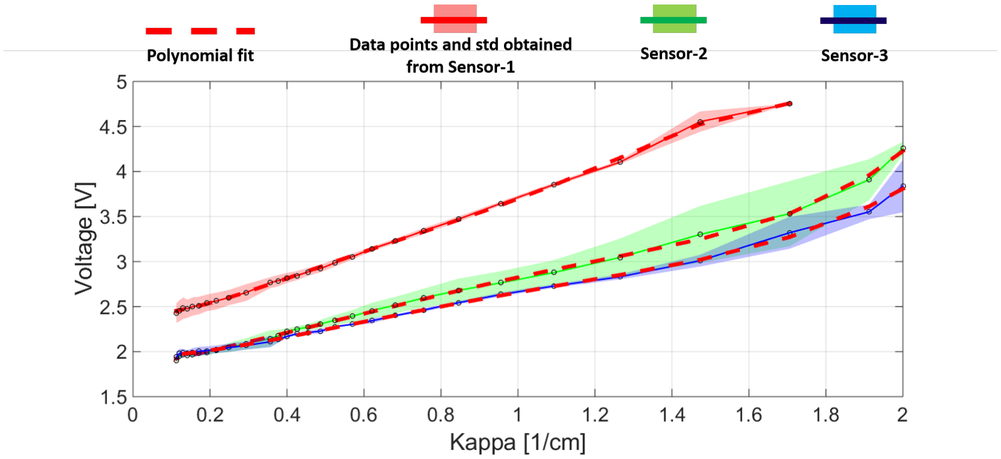

Figure 2.7: Calibration function obtained from data points inside a spiral. It shows change in voltage from 0.1 cm^{-1} to 2 cm^{-1}. Calibration is made for a single direction. Three different voltage datasets are obtained from 30 different curvature points inside the spiral for three different sensors.

between voltage and curvature values. A representative calibration fit for one of the tested sensors is shown in Figure 2.7. The calibration function is a third order polynomial with the following coefficients. $c_0 = 2.32$, $c_1 = 0.98$, $c_2 = 0.61$ and $c_3 = -0.20$.

Each sensor needs to be calibrated individually due to small manufacturing tolerances. Figure 2.7 shows mean and standard deviation of three calibration results from three sensors. Differences in magnet-sensor orientation and distance result in variations in calibration functions, although after a single initial calibration step, the curvature measurements are absolute. Results show that a precise positioning process would ensure repeatability.

2.2.2 STATIC RESPONSE

To verify the static response of a calibrated curvature sensor, I drove the sensor inside the spiral track. To show repeatability, results are demonstrated from two sensors. The calculated curvature inside

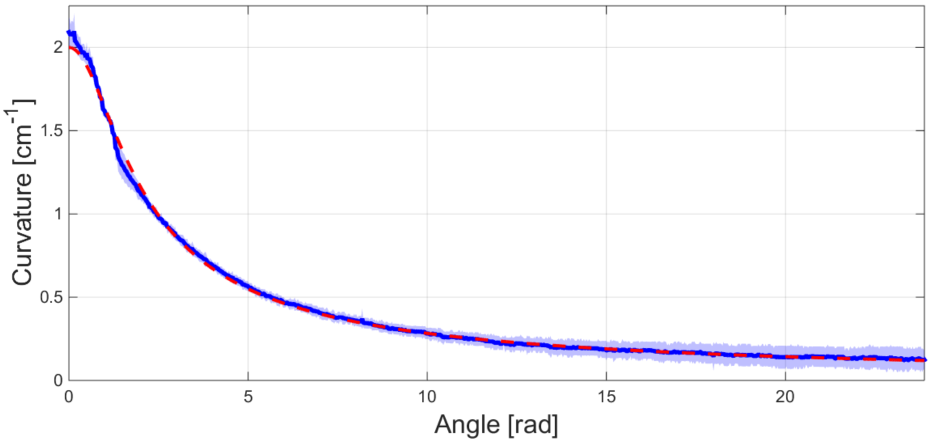

Figure 2.8: Static response of two different curvature sensors inside the spiral track using 5° increments. Each sensor was driven inside the spiral track three times. The dashed red curve is the actual curvature and the solid blue curve is the mean of the measured curvatures. The shaded area displays the standard deviation of curvature measurements.

the spiral is given in (2.4) and Figure 2.6 displays the curvature of the spiral track for a rotation angle range of 0° — 1440°. A calibrated sensor is expected to follow a similar path. To this end, sensors were driven inside the spiral, with 5° increments and waited 5 seconds at each curvature value for four full turns. The measured curvatures inside the spiral in comparison to expected values displayed in Figure 2.8 verify the ability of my sensor to measure curvatures accurately in a static setting.

2.2.3 Dynamic Response

After verifying the ability of the proposed curvature sensors for static measurements, I tested the accuracy of its response under dynamic deformations. For speed tests, I used the elliptical track instead of a spiral. Just as the spiral track, walls of the ellipse controllably and repeatably deform the sensor into different and known curvature values, as a DC motor turns the platform, subjecting the sensor

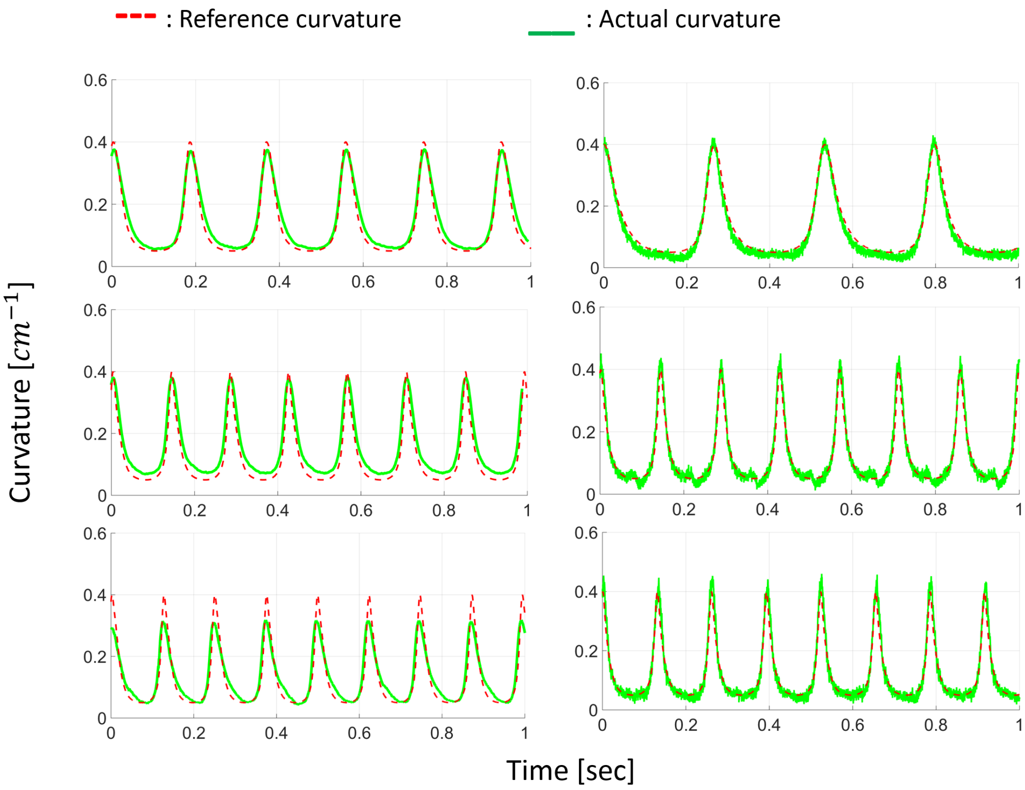

Figure 2.9: A close up of the sensor response for speed tests. The left column shows data obtained from the sensor without a low-pass filter; the right column shows the response after the filter. Ellipse surface is turned at constant voltages of 8 V, 12 V, and 16 V, corresponding to average angular velocities of 11.6 rad/sec (3.69 Hz), 21.8 rad/sec (6.93 Hz), and 23.8 rad/sec (7.57 Hz) for the left column, and 16.9 rad/sec (5.37 Hz), 22 rad/sec (7.00 Hz) and 24.6 rad/sec (7.83 Hz) for the right column, from top to bottom.

to a periodic curvature waveform.

A curvature sensor, moving inside the elliptical track is expected to register the periodic curvature changes continuously in a dynamic setting. A detailed explanation of the elliptical shape and the curvature values can be seen in Figure 2.6. I drove the elliptical track under different input voltages resulting in different angular velocities. I collected angle information from the attached encoder

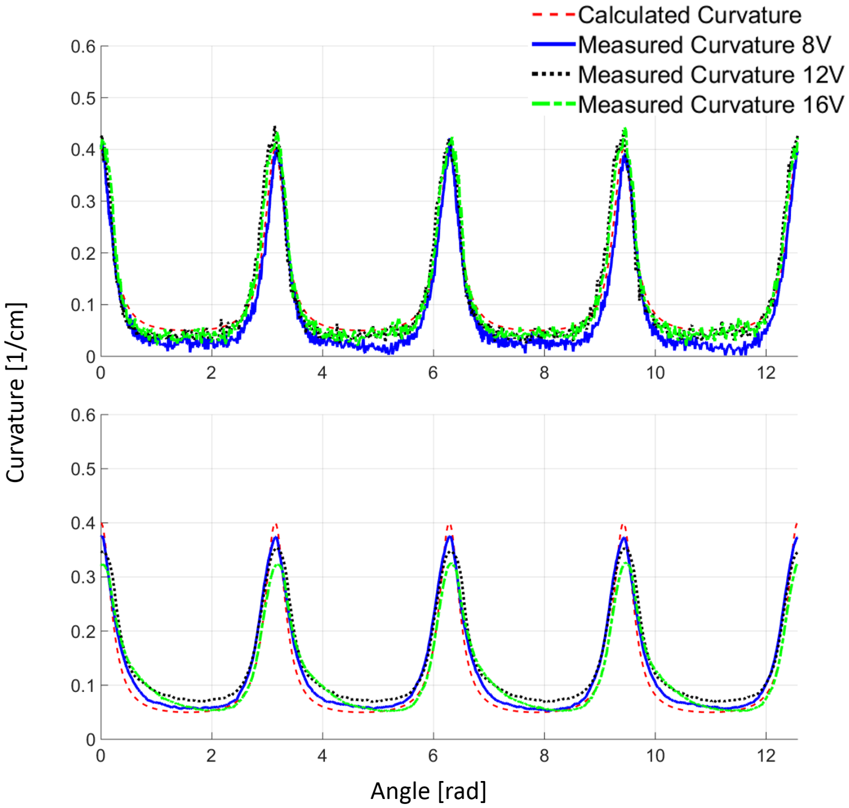

Figure 2.10: Measured and calculated curvature values are displayed with respect to the rotation angle of the elliptical track. The top panel shows data obtained from a sensor without a low-pass filter; the bottom panel shows a response after the filter. The elliptical track was turned at constant voltages of 8 V, 12 V and 16 V. The corresponding angular velocities were 11.6 rad/sec (3.69 Hz), 21.8 rad/sec (6.93 Hz) and 23.8 rad/sec (7.57 Hz) for top panel, and 16.9 rad/sec (5.37 Hz), 22 rad/sec (7.00 Hz) and 24.6 rad/sec (7.83 Hz) bottom panel.

and curvature information from the sensor itself, to compare measured and calculated curvature values. Using (2.5), angle data can be readily converted to calculate the expected curvature. Likewise, voltage information from the curvature sensor is passed through the calibration function to obtain measured curvature values. Raw curvature measurements are displayed in Figure 2.9 for two sensors in the elliptical track running at different velocities. These sensors represent two extremes: without any filtering, and using a low-pass filter circuit with a very low cut-off frequency. The root mean square (RMS) errors of all dynamic tests can be seen in Table 2.1.

High noise can be observed in the left panel of Figure 2.9. The low-pass filter attached to the output channel reduces noise, as shown in the right panel of Figure 2.9. I used 3.2 Hz as cutoff frequency to study its effect on the dynamic response. The filtered sensor was successful in yielding reduced noise, at the expense of an attenuated response to higher frequency deformations. A lagged behavior can be observed in the right column of Figure 2.9. As expected, when the sensor is deformed faster, it is not able to settle on the calculated curvature values. Thus, a low pass filter with an appropriate cutoff frequency is required. The intended application, the soft snake robot undulates at frequencies up to 2 Hz and my choice of 3.2 Hz cutoff is sufficient. Measured curvature versus angle of the ellipse results are shown in Figure 2.10. When the low-pass filter is used for noise cancellation, a deterioration in peak to peak difference is observed. The peak-to-peak amplitude response of both sensors with noise cancellation to bending under different frequencies is displayed in Figure 2.11.

In addition to verifying the measurement capability of the proposed curvature sensors, experimental studies also informed us with details on manufacturing requirements. For example accurate and repeatable positioning of the magnet and Hall element pair is crucial for obtaining the expected calibration function, since the curvature response due to magnetic field measurements is very sensitive in the proposed arrangement. However, I have shown that, even for manual fabrication, a monotonically increasing, one-to-one mapping function exists.

During dynamic bending experiments, it was determined that among the two substrates, copper-

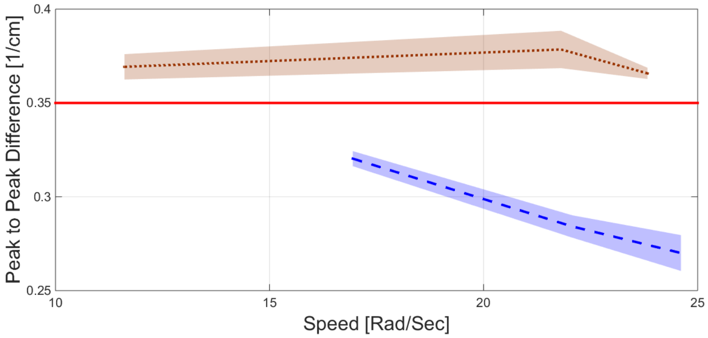

Figure 2.11: Peak-to-peak curvature responses of each sensor in Figure 2.10 is given along with the calculated peak-to-peak response from ellipse surface. Overshoot in the sensor without filter (dot) and decay in the filtered sensor (dash) due to delay can be observed. The variance of peak to peak curvature responses is indicated as shaded areas.

	With Filter	Without Filter
8 V	0.021	0.026
12 V	0.037	0.023
16 V	0.030	0.024

Table 2.1: Root mean square errors between measured and reference curvature data from Figure 2.9. Unit of measurement is cm^{-1}. The elliptical platform is driven in an open loop with three different constant voltage values: 8 V, 12 V and 16 V.

clad FR4 sheets exhibited reduced strength. For periodic loading of curvature waves, the chemically bonded copper traces eventually failed due to bending stresses and fatigue, especially for larger frequencies in Figure 2.9. However, copper foil tape laminated on polyester (PET) films exhibited improved endurance to this failure mode (the first curvature sensor made using this substrate is still functional), since the flexible adhesive layer can deform and absorb the bending stresses. Thus, all dynamic tests were performed on curvature sensors printed on copper foil laminated PET substrates for reliability.

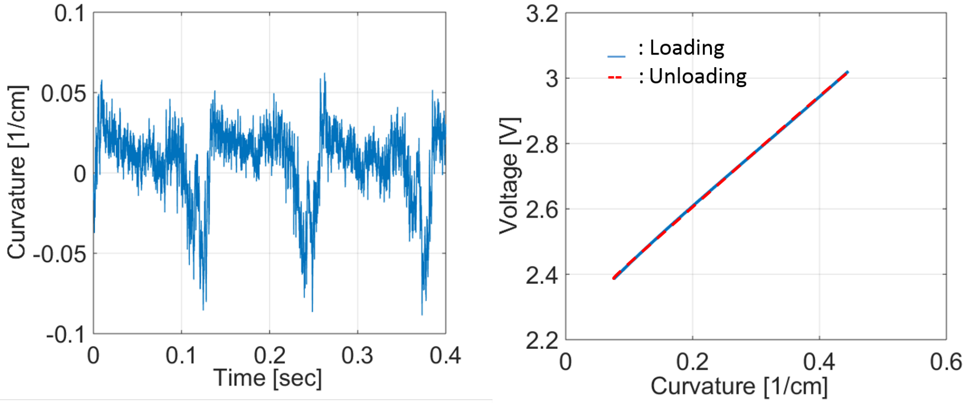

Figure 2.12: Left: Error between reference curvature and measured curvature when the elliptical track is turned with an angular velocity of 23.8 rad/sec. No filtering is applied. Right: Relationship between voltage and curvature when curvature is bent from 0.05 cm^{-1} to 0.45 cm^{-1} and back to 0.05 cm^{-1}. No hysteresis is detected.

2.2.4 DISCUSSION

Hysteresis, linearity and accuracy of the sensor are shown in Figure 2.12. No hysteresis was detected when the elliptical track was rotated at different speeds. A linear relationship between the voltage output from the sensor and curvature is also observed in the right panel in Figure 2.12. The root mean square for the error signal between the actual curvature and reference curvature is 0.0239 cm^{-1}. The slope of a linear fit on the curve in Figure 2.12 is 0.00056 cm^{-1}/mV. This suggests that curvatures as small as 0.0012 cm^{-1} can be measured using a 12 bit digital-to-analog converter. In reality, that level of accuracy cannot be achieved without reducing the noise in the sensor. During the speed tests for dynamic loading, the maximum peak to peak value of intrinsic noise without filtering was measured as 0.05 cm^{-1}, which also represents the minimum detectable curvature in my current settings without filtering.

2.3 CONCLUSION

In this chapter, I presented a novel soft curvature sensor concept and its rigorous testing. The soft sensor is specifically designed to be used with a soft snake for measuring curvatures, although it can be adapted to measuring various deformations in soft bodies through minor modifications.

The proposed curvature sensor system can be built on assembly lines. Consecutive phases in manufacturing, such as printing circuit traces, etching, populating components, and molding silicone rubber can be connected by basic pick-and-place operations. I also discovered that hand calibrating each sensor using a calibration ruler is prone to human error and requires a skilled individual for accurate calibration. For an automated calibration phase as well as repeatable dynamic testing of curvature sensors, I described a custom test platform using continuously changing form-closed tracks.

I demonstrated the accuracy of the sensor under dynamic loading. Results suggest that the proposed sensors are accurate and reliable. They can be used to reconstruct configuration for control applications that require accurate sensing.

The same idea behind the sensing modality can be adapted to measuring different physical quantities, such as force applied on a soft structure as a function of distance. My future work considered a tri-axis, soft-bodied force sensor. Interestingly, the potential application for the tri-axis force sensor, I had in mind with my adviser when this work was published was to use them for human health monitoring.

Instead, I have used the force sensors in robotic grasping and detecting contact state of dynamic hopper mechanism. Details of those works are described in the following chapters. The force ranges in both works were quite different. Grabbing a 250 gr bottle requires measurement of forces nearly an order of magnitude smaller when compared to detecting forces of a hopping robot weighting 250-500 gr. Just by swapping materials, from Ecoflex 00-30 to Dragonskin 30 (manufactured by Smooth-On), I was able to make measurements for both tasks. Moreover, it was shown that undesired effects such as hysteresis did not affect the sensing quality.

3

Soft-Bodied Module Control

Once the sensing problem is at a reasonable state, it is meaningful to think about preliminary control algorithms on soft-bodied materials. As I have shown in my curvature sensor work, the sensors are able to map differences in magnetic field change to curvature values and feed them into a microcontroller at a sufficient bandwidth for control.

Pneumatic actuation is a common choice in soft-bodied robots[87,47]. Usually, a network of cavities can be embedded inside soft material during manufacturing. The design space during cavity network creation can result in unconventional motions (snake movement[46], elephant trunk[26] or octopus arm[12]) that are of interest to researchers. The increase in design space comes at a cost, as with most things in life and engineering. The compliant nature of these robots, which is one of their most significant advantages, stymies traditional efforts to sense their state due to the infinite passive degrees of freedom provided by flexible links. In addition, the dynamic behavior of soft actuators includes a non-linear and non-trivial time delay as pressurized air is introduced through solenoid valve commands. Thus, new methods of on-board sensing and control need to be developed to allow soft robots to be used in real environments to solve practical problems.

To address a lack of proprioceptive sensing in soft robotics research, my paper introduced[68] a soft bending actuator module with embedded curvature measurements as a solution to sensing and control challenges related to soft robots. This is a significant step towards autonomous soft robots with self-contained modules.

Figure 3.1 displays the proposed module design. Among alternatives, integrated sensing can be achieved through Hall effect elements or resistive flex sensors embedded in the constraint layer (neutral bending axis) for curvature measurement. For segment control, we previously presented an approach that used pulse width modulation (PWM) of miniature solenoid valves to regulate pressure inside chambers[81]. The work in this chapter utilizes this controller with embedded sensing to control the curvature of a soft segment.

Numerous novel motions that were previously not achievable by their rigid counterparts were

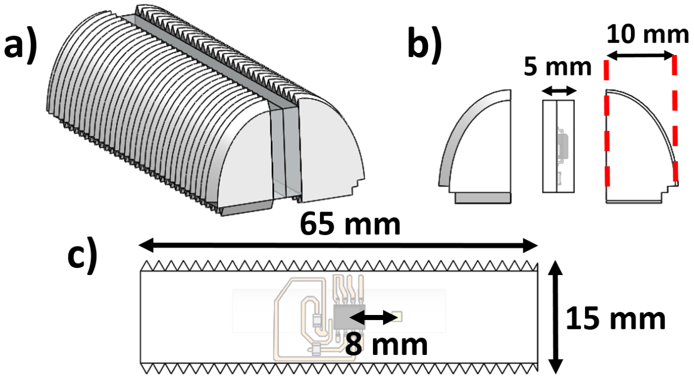

Figure 3.1: Isometric (a), right (b) and front (c) views of the sensor assembly are shown. It is composed of three distinct parts: a soft bending actuator, a constraint layer in the middle of (a) and a curvature sensor. Pictured here is my custom Hall Effect sensor, though the flex sensor fits into the same layer. Circuit tracks for my sensor are etched on a flexible sheet. A hall effect and magnet pair is used for measurements and they can be seen in (c).

recently demonstrated using soft-bodied robot designs: serpentine locomotion[65], octopus arm inspired soft manipulator[53,54], deformable manipulation system[51], a soft bodied legged mechanism[87], soft robotic fish[52]. We believed, in WPI Soft Robotics Lab, the field to be mature enough and it required a stronger understanding of controllers, sensors and actuators that would help soft robots achieve an increased level of autonomy. Soft robots can have very different configurations depending on the design. Indeed one advantage of soft robots is the ability to achieve relatively complex motions such as quadruped locomotion through simple designs[80]. Nevertheless, more complex tasks or locomotion in uncontrolled, open environments would eventually need feedback controllers. In this chapter, I focus attention on developing low-level curvature controllers and corresponding sensor systems appropriate for the recent soft robot designs[46,50].

Accurate and embedded sensing along with a controller for regulating deformation are required for robots made out of soft bending actuators. Our snake robot[65,46] is able to move without feed-

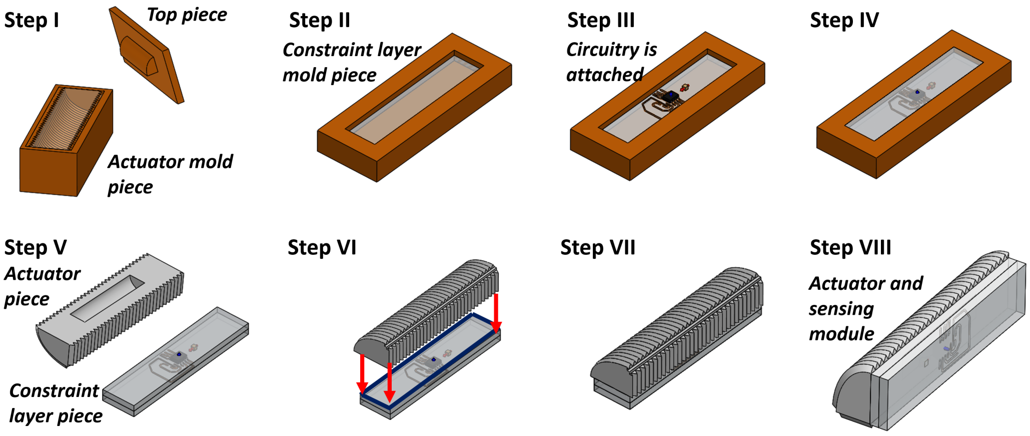
Step I
Top piece
Actuator mold piece
Step II
Constraint layer mold piece
Step III
Circuitry is attached
Step IV
Step V
Actuator piece
Constraint layer piece
Step VI
Step VII
Step VIII
Actuator and sensing module

Figure 3.2: Manufacturing steps of the actuator are shown in the figure. The figure shows mold designs for the actuation chamber and the constraint layer along with information on how to attach them. The actuator in Step VIII can only bend in one direction, a second actuation chamber can be attached to the opposite side for bi-directional actuation.

back control using a predefined gait pattern to generate a traveling curvature wave of its segments. Nevertheless, even simple tasks, such as steering, or finding its way through constrained environments and narrow spaces, would require some sort of feedback for motion control and planning. In a serial arrangement of bending segments, positions of points on each segment can be defined by a single curvature value. This is due to a uniform bending moment being applied on the segment by our fluidic soft actuators[47]. Thus, kinematically stitching constant-curvature arcs, the configuration of the whole body can be obtained using curvature measurements of each segment. This particular arrangement assumes no external forces including out of plane gravity and contact forces. When an external force is applied the constant curvature assumption breaks.

There are a number of approaches to sensorizing soft-bodied segments[38,56,94] and they also provide ways of measuring the curvature of bending soft bodies. For example, a specific type of elastomer curvature sensor[49] uses conductive liquids to address this issue. Finding appropriate channel geometries for required curvature ranges and manufacturing difficulties are two reasons for avoiding conductive liquids in my work. Creating channels inside silicone and injecting liquid material is a challenge. Optical fiber Bragg grating is another technology used for curvature measurements[99]. Authors[17] use light sensors along with mirrors and a light source to detect concavity and convexity to measure deflections. This solution is not practical for my system. The sensors have to be embedded inside silicone rubber and effect of material properties on opacity and dispersion may be uncertain. Commercially available resistive curvature sensors were recently used to detect soft finger curvature[28]. These sensors use materials that change resistance under strain to measure bending of a substrate. Resistive sensing, while convenient, is expected to suffer from thermal and drift effects, especially under dynamic loading. To test this last point, this chapter compares my proposed approach with a resistive curvature sensor (Spectra Symbol, Flex Sensor).

For the scope of the module control work, I specifically picked a magnetic Hall-effect sensing modality due to its accessibility, simple manufacturing steps, accurate response, and lack of external processing circuitry requirements. With a magnetic operational principle, this sensor is capable of accurately measuring curvature at a high bandwidth. Moreover, I have already showed that a flexible layer sensorized by a magnet and a Hall effect IC (AD22151 - Analog Devices) can deliver accurate curvature measurements under repeated loadings as fast as 7 Hz.

To achieve a complete soft-robotic system in the future, this chapter details the design of a soft module composed of a pneumatic soft actuator, a soft-bodied curvature sensor, and a control algorithm designed specifically for soft segments. I propose a composite bending soft actuation module with embedded curvature sensing located at the neutral bending axis to show that such a module can be controlled reliably using on-board feedback.

3.1 COMPOSITE SOFT BENDING MODULE

3.1.1 ACTUATION

The mechanical design of the composite module is based on an already developed soft bending actuator[47]. The actuator design can endure pressures up to 10 psi. Settling time for maximum deformation is approximately 0.8 seconds. Compared to serpentine air channels in our earlier work[64], these improved performance values were due to the addition of external threading along with a single chamber design.

Manufacturing steps of the soft actuator and integrated sensing elements are shown in Figure 3.2. The actuator body is composed of three separately molded components: two semi-circular actuation chambers and one constraint layer. Nylon sewing is tightly wrapped around the actuation chambers and bonded using a layer of silicone. In the constraint layer, I embed electronics on a flexible PCB to achieve a composite structure. The electronics layer is inextensible. It is created by applying a copper foil tape (0.01 mm thick) on to a thin PET film (0.12 mm thick). The circuit traces are printed on the copper foil using a Xerox ColorQube printer and it is etched in a Ferric Chloride tank.

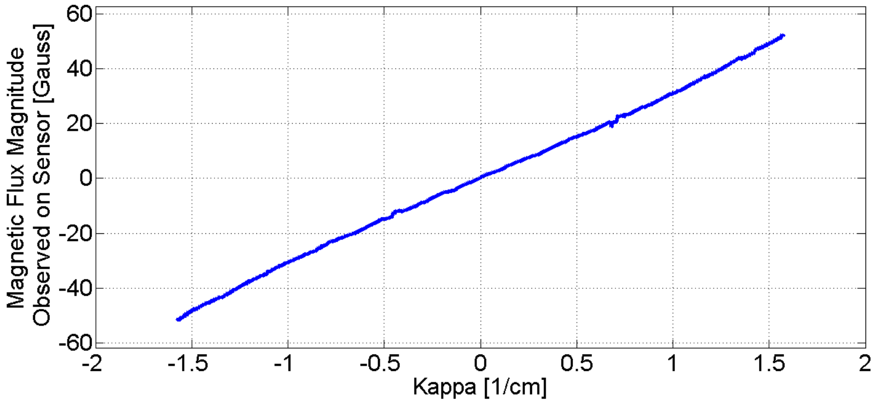

Figure 3.3: Observed magnetic flux density is shown for different curvature values. Magnetic Flux Densities are obtained from finite element analysis as a look-up table. Position calculations are coded in Matlab. The distance between the magnet and the Hall element is 8 mm.

3.1.2 Sensing

As mentioned previously, I embedded two different curvature sensors inside the constraint layers of the self contained segments in Figure 3.2. The first is my custom design with a Hall effect sensor and a magnet couple. The second one is the commercially available resistive flex sensor. The resistive flex sensor is positioned in the middle of the curvature sensing segment, same as the hall effect based design.

The operational principle of the proposed magnetic curvature sensor is based on the measurement of magnetic flux density around a magnet using a Hall element, when a soft segment bends into different curvatures. The sensor and magnet couple are displayed in Figure 3.4. The measured voltage is then inserted into a calibration function which maps voltage measurements to curvature values. This concept requires one-to-one mapping and monotonic increase to produce useful results. Magnet position and orientation settings, which would result in such mapping are discovered

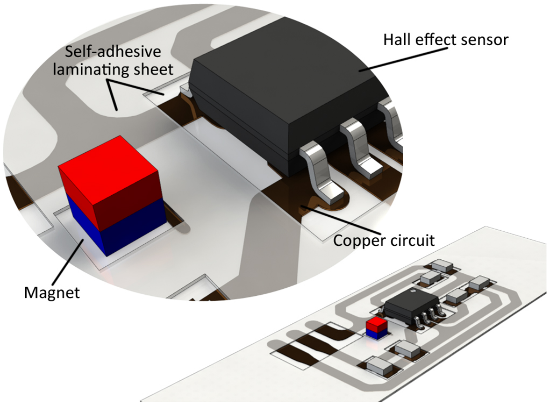

Figure 3.4: An adhesive copper sheet is placed between two self laminating sheets. The top laminating sheet has laser cut holes for component placements. The assembly is passed through a lamination machine. Magnet and the Hall-effect IC are shown. Red and blue color labels of the magnet indicate north and south poles respectively. The edge length of the cube magnet is 0.8 mm and the overall thickness of the curvature sensing segment is 1.5 ± 0.15 mm.

through modeling the magnet using COMSOL Multiphysics and simulating the model parameters in a constant-curvature bending simulation of the silicone rubber segment. To show that this approach is suitable for actual implementation, I present the results of a simulation in Figure 3.3. A more detailed discussion about this curvature sensing approach and experimental analysis of its response is provided in 2.

The magnetic curvature sensors are manufactured on custom flexible circuits using a copper tape with a printed circuit trace pattern and plastic laminate film. The copper tape is bonded onto the laminate sheet and covered by another laminate sheet layer to increase the strength of the traces for protection. Openings for circuit components are laser-cut on the top laminate sheet to allow for a proper fit. Figure 3.4 shows the detailed view of the flexible sensor. Once the flexible circuit board is completed, circuit components are populated using manual pick-and-place, which takes approximately 30 min.

For calibration, I use infrared reflective markers for tracking four points on the segment by a motion capture system, to monitor the angle of both ends of the segment. Experimental setup for the segment with markers is shown in Figure 3.6. Assuming a constant curvature along the arc-length of the segment (due to uniform moment loading), obtaining the curvature of the segment from these four points is a simple geometric operation. The voltage data and reference curvatures are matched in Matlab with a fourth-order calibration polynomial, which can be seen in Figure 3.5.

The flex sensor changes resistance as a function of curvature, which can be measured using a simple voltage divider given by:

$$V_o = \frac{R + C\Delta\varkappa}{R + R_e + C\Delta\varkappa} V_{in}, \tag{3.1}$$

where R is the internal resistance and it is treated as an unknown. R_e is the known external resistance of the voltage divider. C is a constant parameter, which relates curvature to resistance change. C was calculated using calibration data and a least-squares fit in a similar way to the magnetic curvature sensor.

The resistive flex sensor output is measured by a simple voltage divider, so a linear model was found to be an accurate calibration function. On the other hand, the Hall-effect response was more non-linear than I expected. Therefore, I use a higher order polynomial. The non-linearity in the magnetic sensor response can be reduced through design optimization by varying magnet position and orientation, and a more repeatable manufacturing method. During the experiments, calibration coefficients of each sensor was slightly different due to differences resulting from manual manu-

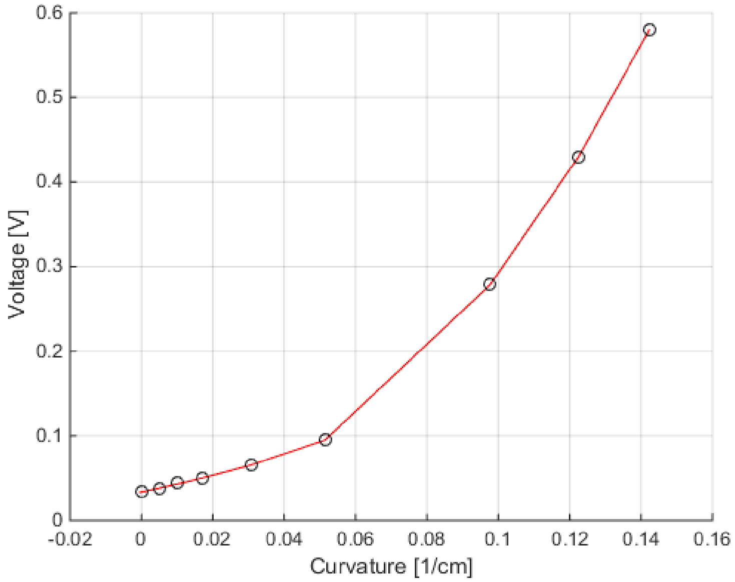

Figure 3.5: Nine different data points are matched between curvatures from visual tracking and analog voltage measurements. Black circles represent these points. Eventually, they are used to fit a fourth order calibration polynomial.

facturing. It would be possible to use the same calibration polynomial for all sensors with an automated manufacturing process.

3.1.3 Control

I use a constant pressure source in my setup along with high-speed, on-off solenoid valves. Our previous work in SRL demonstrated that average pressure inside soft actuation chambers can be regulated through PWM using valves[81]. The segment is driven by two actuation chambers. Incoming pressure, which is not measured in real time for the purpose of feedback control, to the chambers is regulated using the PWM duty cycles of the solenoid valves at a frequency of 40 Hz. Thus, this is a system with two inputs (the PWM duty cycles on the valve of each actuator) and a single

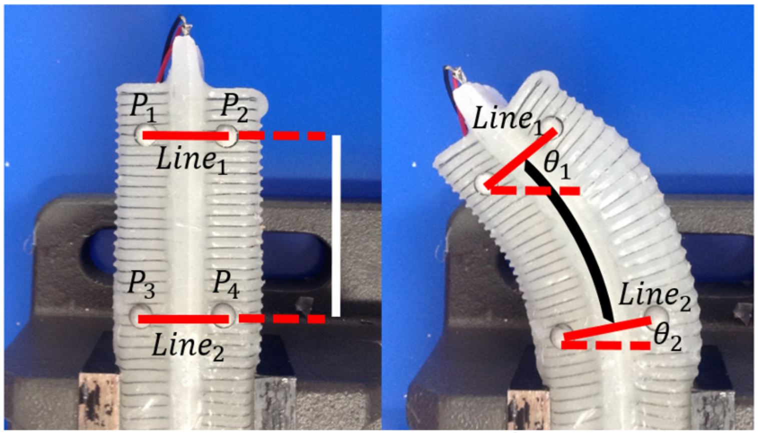

Arc Length: 3.5 cm
Curvature: 0.0 [1/cm]

Arc Length: 3.5 cm
Curvature: 0.15 [1/cm]

Figure 3.6: The visual markers for four points are shown in the left figure. Angles of two lines segments are calculated from them. These angles can be used along with the arc length for computing curvature of the segment under circular deformations. This is the approach I implement for calibrating the hall effect sensor through visually tracked points. The distance between the top and bottom lines are 3.5 cm. The arc length does not change when the segment is actuated because the sensor layer acts as an inextensible constraint layer in the middle. When actuated with full duty cycle under 8.0 psi, the segment can bend up to 0.15 [1/cm].

output (the curvature of the segment). For simplicity, we developed a scheme where only a single actuator was being driven at a time to reach a desired curvature value. Using this simplification, the two-actuator system could be reduced to a single control input, which was translated to actuation of Actuator A when positive, and Actuator B when negative.

To control the curvature of the bending actuator, we adapted an iterative sliding mode controller[81], the final control law of which is given as:

$$u(t) = u(t - \Delta t) + K(\dot{e}_x + D_x e_x), \tag{3.2}$$

where $u(t)$ is the control input, $u(t - \Delta t)$ is the control input from the previous time step, $e_x = \varkappa_{desired} - \varkappa_{measured}$ is the curvature error, $\dot{e}_x$ is the derivative of the error, and K and D_x are control weights. $u(t)$ is given to the system as the PWM duty cycle and it is saturated between $0.0 - 1.0$.

3.2 Experimental Results

To characterize the sensors, I perform step loading experiments showing the behavior of each sensor when actuated to a constant curvature before returning to its original straight configuration. The results of these experiments can be seen in Figure 3.7 for the resistive flex sensor and Figure 3.8 for the magnetic curvature sensor.

The resistive flex sensor in Figure 3.7 seems indifferent to small changes once the actuator is pressurized up to 8 psi (after around 4 seconds). This is the first limitation of using a resistive sensor. Another interesting part of these experiments was when the actuator was depressurized and the seg-

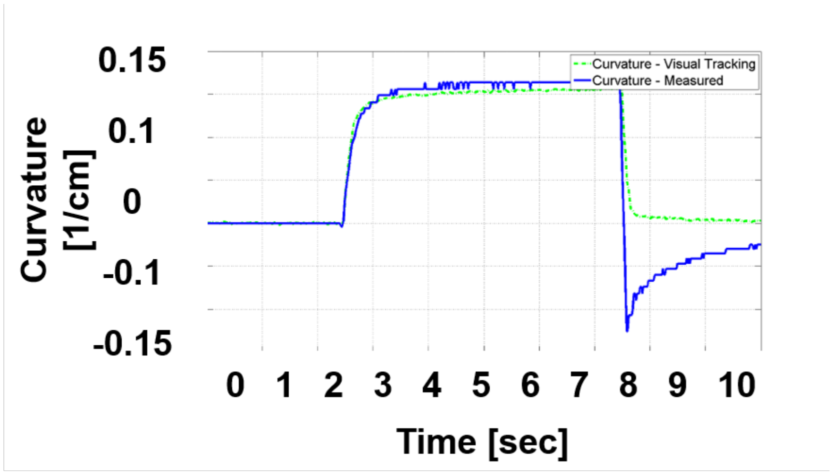

Figure 3.7: A segment with the resistive flex sensor is activated for five seconds under 8 psi. Mean value of visually tracked curvature is 0.1545 cm^{-1}, when the segment is activated. Mean value of measured curvature between $2.5 - 7.5$ seconds is 0.164 cm $\pm$ 0.008 cm^{-1}. A large overshoot of approximately %75 is observed as the pressure is released.

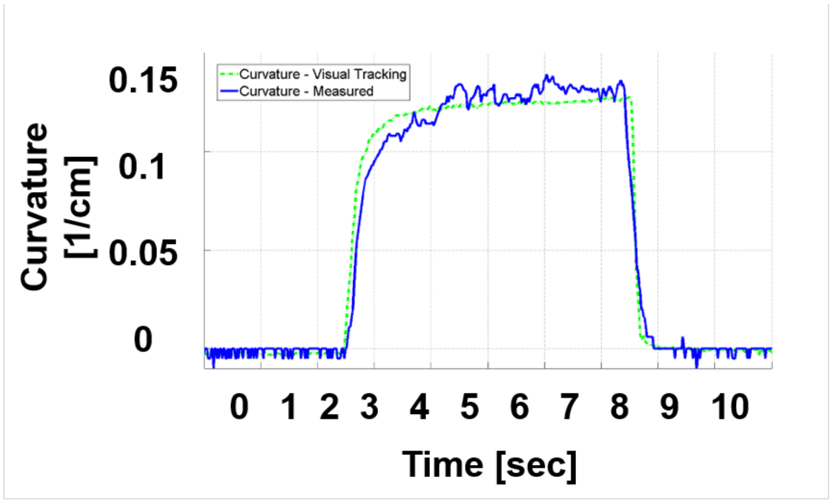

Figure 3.8: In this figure, the segment with the custom magnetic curvature sensor is activated for five seconds under 8 psi. No overshoot is observed on the way back. Mean value of visually tracked curvature when activated is 0.1247 cm^{-1}. On the other hand mean value of curvature measurement from the magnetic curvature sensor is 0.1308 $\pm$ 0.015 cm^{-1}. No overshoot is observed.

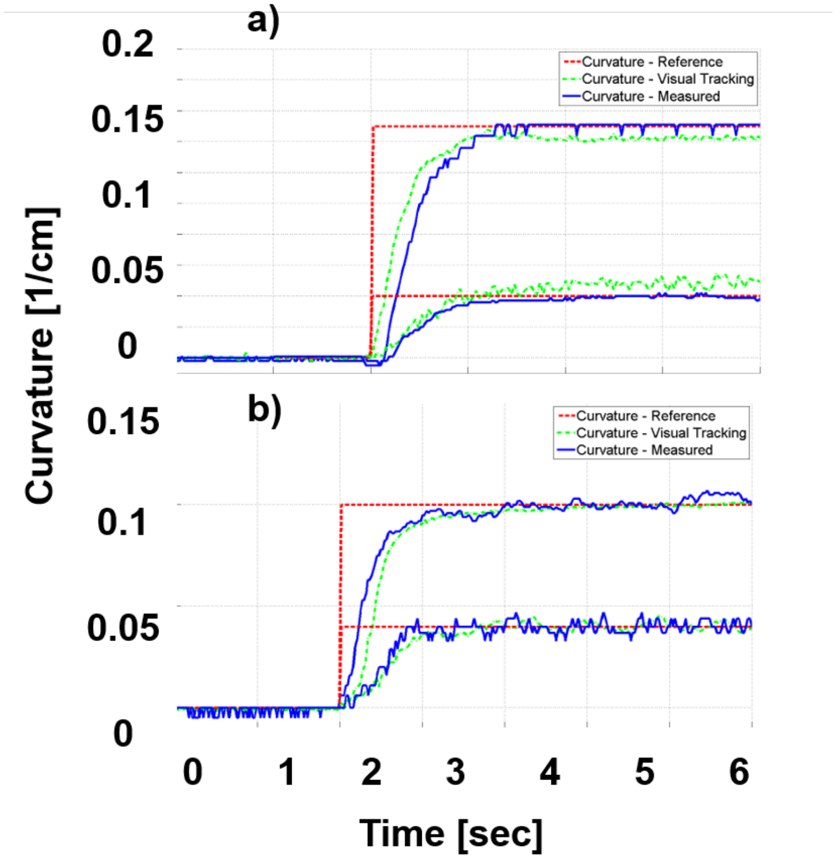

Figure 3.9: Two step waves with magnitudes 0.04 cm^{-1} and 0.15 cm^{-1} are tracked using the flex sensor (a) and 0.04 cm^{-1} and 0.1 cm^{-1} with the hall effect sensor (b). A damped controller with same control gains is implemented for both sensors: $K_p = 0.25$ and $K_d = 60$. Maximum pressure is 8 psi for both of the experiments and average pressure is regulated through PWM. Feedback controller is implemented on top of PWM. Differences between visually tracked curvature and measured curvature for high amplitude step wave were 0.008 cm^{-1} for flex sensor and 0.0014 cm^{-1} for the Hall Effect sensor. The measured 5% settling time for the large step signal tracking with the Hall effect sensor is 1 sec.

Table 3.1: Comparison of sensors from maximum pressure activation

	Flex Sensor	Magnetic Sensor
Sensor overshoot	75 %	0.0 %
Steady state measurement error [1/cm]	0.01	0.005
Peak-to-peak noise magnitude [1/cm]	0.008	0.015

ment returned to its original state. When this occurred, the Hall effect sensor followed accurately, though still exhibiting noise. The resistive flex sensor, on the other hand, significantly overshot to a negative value of curvature nearly equal in magnitude to the pressurized curvature, before slowly settling back towards 0 to match the actual segment behavior. From Fig. 3.7, it can be observed the flex sensor still doesn't return to reading the correct value even 2.5 seconds after the segment reached 0 curvature. In fact, it takes 10 seconds from depressurization for the flex sensor to reach 5% of the actual value, indicating significant limitations in the accuracy of resistive measurements under dynamic conditions.

Next, to investigate the effect of using both sensors on feedback control, I perform closed-loop control with the system using step reference curvatures for both the resistive flex sensor and the magnetic curvature sensor, while simultaneously recording ground-truth curvature values using external motion tracking to evaluate the accuracy of the two curvature sensing modalities. Results can be seen in Figures 3.9-a and 3.9-b for the flex sensor and magnetic curvature sensor, respectively.

These results show that the control scheme is functional as it supplies the necessary control inputs for both segments to reach the desired curvatures based on their on-board curvature sensor measurements. The Hall effect sensor has noisy data, but it brings the segment to the correct cur-

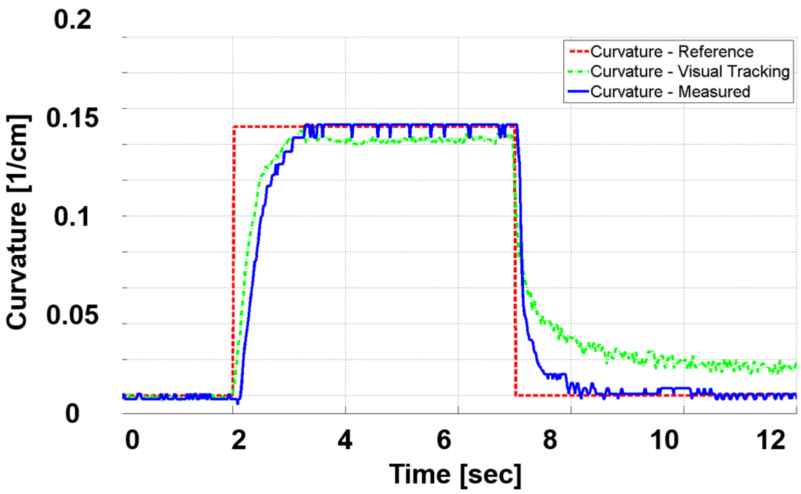

Figure 3.10: Overshoot in the response of the flex sensor is showed during active control. The controller drives the system to zero curvature based on reference signal after 6.5 seconds. Nevertheless, the actual curvature of the segment, which is measured by the visual tracking, floats around 0.02 [1/cm] for a significant period of time.

vature. The flex sensor, on the other hand, returns clean but somewhat inaccurate data; its final curvature being at a small offset from the desired value by around 0.008 cm^{-1}. This offset is in different directions for the trials shown, indicating its complexity as well as highlighting the difficulty of compensating for this sensor behavior. The analysis of the sensor responses is given in Table 3.1.

Figure 3.10 shows the inconsistency between the visually tracked curvature and the sensed curvature through the flex sensor once the system is referenced to go to zero curvature. In addition, the active control test showed that the overshoot in the resistive flex response caused the segment to stop short of the actual 0 curvature point by a significant margin, though less than the negative spike from the open-loop experiment in Figure 3.7.

3.3 Conclusion and Discussion

This chapter introduces the design, fabrication, and experimental evaluation of a new composite soft bending actuation segment with embedded curvature sensing to enable proprioception and closed-loop control in soft robotics. I fabricate two different versions of the segment: one with a commercially available resistive flex sensor and the other with a magnetic curvature sensor of my own design, and used a motion capture system to calibrate and verify the validity of these two sensors. In addition, I use an iterative sliding mode controller to drive the segment through step reference functions to demonstrate the performance of the proposed composite sensing and actuation segments as well as compare the usability of the two sensors.

I find that the segment is capable of reaching specified curvatures with speed and precision using the controller for both sensors. Moreover, it is observed that my magnetic sensor returned noisy but accurate data, while the resistive flex sensor had an offset at steady state. When returning to the neutral position, the resistive flex sensor exhibits a large overshoot in the negative direction before slowly returning to the actual curvature. I perform additional experiments on this and I show that this phenomenon caused feedback control of the segment to significantly undershoot when returning to the zero curvature position. This demonstrates that the magnetic curvature sensor represents an improvement for use in soft robot closed-loop control, perhaps using an appropriate low-pass filter to reduce noise will be useful in future implementations.

Even though the measurement scheme with the constant curvature assumption is useful for planar movements under no external forces, effect of gravity would significantly complicate the sensing and the control system. If an external force was applied to the segment in the plane of actuation, the segment would no longer have a constant curvature. Thus, a single curvature sensor measuring a single degree of freedom would be unable to accurately describe the kinematic state of the segment. A flexible array of sensors inside the segment would be needed to reconstruct this complex shape. Similarly, to extend the sensing approach to 3-D bending measurements, a potential solution is to use 3-D magnetometers to detect the full magnetic field vector, and hence 3-D bending and potentially other deformations.

On the practical side, I experienced cracking of circuit traces when the sensor circuitry was excessively bent. This problem was observed when the flexible circuit board substrate was 0.1 mm-thick FR4. To overcome this issue, I use copper foils laminated to plastic sheets. The change in structural material of the circuit resulted in circuits that were more durable under repeated bending.

I also had a number of problems with the segments, particularly with regards to pressure leakages. The problem areas were the interfaces between the pressure chambers and the pressure lines as well as the seal between the pressure chamber and the inextensible constraint layer. A redesigned system for improved reliability, will allow to perform more detailed experiments as well as use them more effectively in soft robots.

This point in my progress as a researcher also marks the shift from soft bending modules and robots that utilizes them to my interest in combining soft and compliant technologies with legged locomotion. Even though my work on both curvature sensors and their control was used by Luo[46], I did not have a deep understanding of material science to improve the condition of actuation. For example, the snake robot utilized passive wheels for locomotion. This was convenient for preliminary results but it limited the robot to planar surfaces only, reducing its autonomy significantly. A skin-like material that would replicate the ideal friction behaviour of the wheels (high friction in the direction perpendicular to segment neutral axis and low friction in the axis parallel to neutral axis) is currently unknown outside of biological lifeforms such as snakes. Moreover I was skeptical of the utility of soft actuators inspired by nature and preceding robotic arms. Also, I was thinking, that developing control structures mimicking the previous rigid bodied robots could be seen as preparing for the previous war: as in new control structures for new type of soft robots could be fundamentally different from what we had imagined before, therefore rendering our over-engineered control efforts fruitless.

Because of these risks I shifted my attention to a topic I already had both theoretical and practical knowledge: dextrous legged locomotion. I knew that the approach utilizing zero moment point and exact control of center of mass trajectories in robot locomotion gave interesting results but I was also aware of more dynamic mechanisms that utilized mechanism compliance to achieve what was once believed to be complex motions with simple algorithms. I shifted my research focus to integrating my knowledge in soft robotics to creating compliant structures for more efficient legged locomotion. Before going into the details and results of that work, next chapter goes over the details of a soft-bodied force sensor. The work on force sensor is one of the connection points between soft robotics and designing compliant mechanisms to achieve more dexterous robot motions.

4

Soft-Bodied Force Sensors

The robots and mechanisms discussed so far existed without a well defined application space. This chapter introduces the soft-bodied sensing technology to a core problem in robotics: contacts. By a contact I mean any rigid bodied collision event. They are both hard to model mathematically and equally hard to detect and handle via real time controllers. From my work on magnetic curvature sensor, I already knew the sensing bandwidth was high enough for preliminary control tasks and I hoped that if one could find a mapping between magnetic field measurement and curvature values, it would also be possible to find a similar well-behaved function for mapping magnetic field measurements to forces. So the force sensor in this chapter is created due to the need for them in robotics and my realization that soft-bodied sensing was a good candidate for the task.

Direct force and tactile sensing remains an open technical problem in robotics[14,59,101]. To address this problem, new sensing mechanisms and modeling approaches need to be developed to achieve compliant, safe, and aware interactions between robots, human users, and the environment. I observe three fundamental challenges that impede progress[13]. First, it is difficult to obtain a reliable sensing modality between external forces and a measurable change in a physical medium, without detrimental nonlinearities or other artifacts such as hysteresis or time delay. Second, modeling to obtain a reliable map between the external force and the measured physical change is challenging, especially for multi-dimensional measurements. Finally, scalability tends to be a challenge, to obtain useful spatial resolution over a surface, while avoiding crosstalk between sensing elements. This chapter addresses each challenge by presenting a magnetic sensing modality and neural network based modeling of a small tri-axial soft sensing element.

In terms of sensing medium, tactile sensing literature may be classified into: 1) stimuli responsive and/or composite materials that mainly employ resistive or capacitive measurements, and 2) using embedded discrete electronic components or other physical quantities such as optical or magnetic signals within the sensor body. Resistive sensing has been a popular method, although it may suffer from dynamic artifacts[32,61,34,82]. Wood et al.[95] uses a conductive fluid (eGaIn) placed in channels cre-

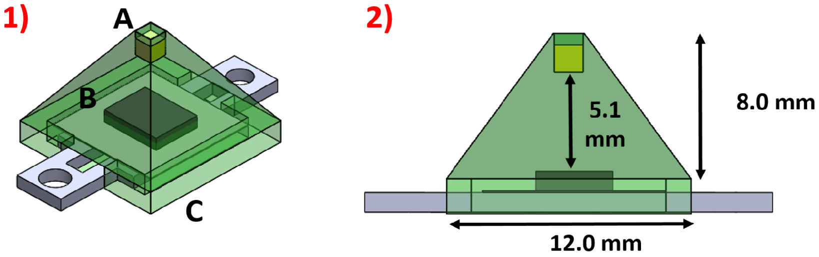

Figure 4.1: 1) Design of the proposed tri-axial soft force sensor utilizes a miniature magnet (A), Hall Effect IC (B), and a circuit layer on an acrylic sheet (C), embedded in a pyramid shaped silicone rubber substrate. 2) The sensor prototype is 8 mm tall with an 12 mm wide square base.

ated on a soft matrix to measure applied forces. These are multi-axis force sensors and can measure forces in normal and shear directions. But fabrication using eGaIn involves a number of challenges[33]. Alternatively, pressure (or force) can be measured in the normal direction by the change in capacitance between two PDMS layers filled with carbon nanotubes[43]. A similar measurement idea is realized via conductive textiles[93]. Authors[98] present pressure and position sensors made of conductive elastomers co-printed into a soft actuator in a single process without assembly. These sensors are capable of providing feedback because of their innovative design and the piezoresistive effect of conductive elastomers. The micro, tri-axial force sensor[71] is an example where sensing medium is reflective measurements obtained from optical fibres.

In another work[86], a commercially available barometric IC is embedded in a soft elastomer, to perform as a 1-D tactile sensor to measure normal forces. Yi et al.[99] presents a tactile sensor using optical fiber Bragg grating based on phase modulation of the optical source to determine the forces applied on the sensor. Sohgawa et al.[82] proposes a resistive tactile sensor using piezo-resistive cantilevers embedded in a soft matrix. It is important to note that these existing solutions suffer from various inherent challenges such as a lack of 3-D force sensing capability, relatively complex fabrication and signal processing circuitry, or hysteresis and time delay.

Regardless of the sensing medium, modeling and obtaining a reliable mapping between the force and the measured physical change is crucial and challenging, especially for multi-axis force sensing. Youssefian et al.[102] employs multiphysical finite element analysis (FEA) to describe the behavior of a dome-shaped magnetic tactile sensor. Using FEA models are useful but in a multiphysics environment small errors and initial settings reflect heavily during the actual experimental testing of the sensors and since elastomers (e.g. Ecoflex 0030) are known to be highly nonlinear, FEA modeling is not straightforward. In addition, such models are usually not applicable for real-time computation.

Authors[94] approximate the sensor's resistance change response as linear and create a calibration matrix using least mean squares method. A similar approach was taken by Cho et al.[10], where a linear regression model was employed to find the relationship between force applied and the corresponding change in voltage. The linearity approximation makes these models simple enough to calculate the force mapping in real-time, but they are highly simplistic and thus, prone to errors. Response reliability is also important. Lipomi et al.[43], mentions carbon nanotubes not being aligned after repetitive loading. The resulting hysteresis can be reduced by depositing carbon nanotubes at a pre-stretched state, which may increase complexity and repeatability issues. These limitations motivated us to consider approaches that use machine learning as a method for estimating the complex relationship between the applied force and the measured change in the magnetic field vector in the proposed sensor to offer both accurate modeling and real-time computation for the nonlinear sensory mapping.

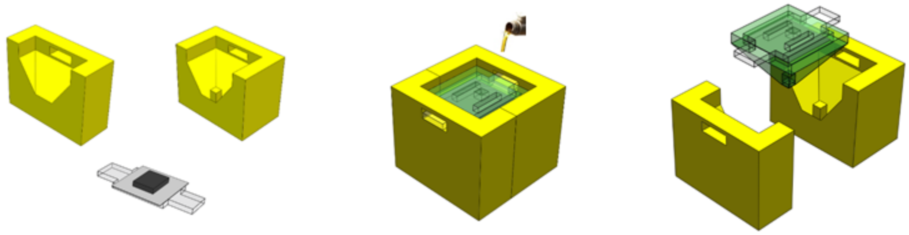

a) 3D printed molds required for fabricating the sensor are shown in yellow (top). A custom flexible PCB is bonded to an acrylic carrier (bottom).

b) The molds are clamped together with the acrylic circuit carrier and liquid silicone rubber precursor is introduced.

c) Cured silicone rubber sensor body is demolded with a cavity for the magnet.

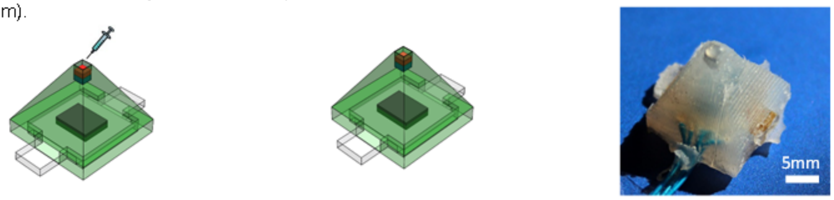

d) Magnet is placed in the cavity and liquid silicone rubber is injected to seal it in place.

e) Cured and finished force sensor module CAD model.

f) Actual force sensor prototype.

Figure 4.2: Manufacturing process of the proposed tri-axial soft force sensor

Using an embedded miniature magnet and flexible electronics in a soft substrate, I have previously shown that sensing local changes in magnetic field is suitable for accurate and high-speed measurements on the curvature of a flexible bending body[68]. In previous research, my objective was to obtain curvature measurement from soft silicone rubber segments for a specific type of bending soft actuator utilized in a snake robot[46]. This article employs similar design principles to force/contact measurements on a soft deformable substrate and in a small form factor.

Hall effect based sensors have gained prominence recently[101,39,30,88,90,89]. Tomo et al.[88] presents a soft sensor which utilizes a magnet for detecting forces in multiple axes. 16 Hall-effect ICs are used in total for one sensor module, hence adding to the complexity of the design. Valdastri et al. also has shown similar succesful results in 3D force sensing via MEMS[92,4]. In this work, I present accurate force measurement results using a single IC with a magnet on top. The sensors also do not need any explicit noise filter thus enabling them to retain a faster response.

The sensor design utilizes a 3-axis Hall effect sensor IC and a small magnet placed over it at a defined location, embedded inside a soft elastomer substrate. This gives the composite mechatronic structure the compliance required for force sensing. A 3-D model is shown in Figure 4.1. Any force applied on the soft matrix produces a deformation on it, which changes the position of the embedded magnet and this in turn causes changes in the magnetic flux values around the Hall element. This measured change has a non-trivial relation to the force applied on the sensor module. A limitation of magnetic force sensing is shielding the sensing volume from external magnetic and ferromagnetic influences. The proposed sensor design needs to be mechanically shielded for real world implementation. For example: proper shielding would be needed if sensor is utilized for picking up ferromagnetic objects.

I introduce two main novel contributions with this chapter. With the help of a master student, who was quite interested in finding a way to implement machine learning inside novel robot hardware design, we used a neural network to calibrate the force sensor in 3-D and demonstrate its generalization ability to other materials and loading conditions. We showed that the network is able to learn to respond to a large range of force directions whereas only small number of training forces are applied at pre-determined directions. We also showed that the same network can be used with sensor prototypes that were not in the training set. This means that the network is able to overcome minor manufacturing differences and it can be used to scale up the sensing resolution without scaling up the calibration efforts. Recently the usage of machine learning has seen great interest for capturing complex relationships between the input space (forces) and the output space (the sensor measurement)[23]. Fully connected neural networks (FCNs) are explored for characterization[88]. However, the results show that the network is not able to generalize beyond the training conditions. Here, we present FCNs based on the Net2Net initialization technique[9], which provides better regularization of the network. We show that the network is able to generalize very well in Section 4.2.

The second novelty is the pyramid shape. One of the main factors that affect the dependability of a tactile magnetic sensing element is its shape[41]. The shape of the contact surface that tapers to a point helps in restricting and channeling the movement of the magnet inside the soft matrix. There are other shapes used for designing force sensors as well, we see a dome-shaped magnetic soft sensor with the magnet immediately below the dome which helps in obtaining a highly accurate model of the sensor[101]. In another work, the shape of the soft matrix is a cuboid and the magnet is placed over the Hall element[88]. A considerable problem with these designs is that the applied force may cause rotation of the magnet about its own axis in unmodeled ways, thus requiring additional calibration data and also reducing measurement dependability. In this work, I utilized the shape of a pyramid with the magnet embedded within the pyramid (as close to the centroid as practically possible). The advantage of this shape is that off-center forces acting on the sensor would tend to act about the centroid of the sensor and thus the tendency of rotation of the magnet about its own axis is reduced, greatly improving reliability.

This chapter is organized as follows: In Section 4.1 I discuss the design and manufacturing methods for the proposed soft 3-D force sensor. I include detailed information on electronics and fabrication process. In Section 4.2 I discuss in detail how data is collected for characterization and how it is used to map the function space of the sensor by a Neural Network. In Section 4.3, I discuss the re-

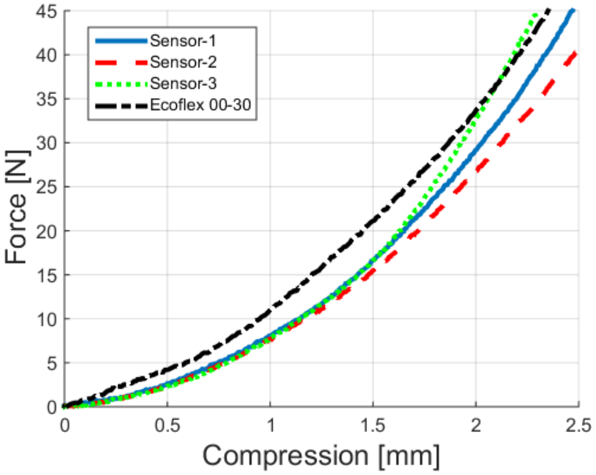

Figure 4.3: Force versus compression data is obtained from three sensors and compared to a solid Ecoflex 0030 segment, indicating minimal effect on the material compliance by the embedded magnet and electronics.

sults for the dynamic response tests on the sensor and also present a use case application of the force sensor by performing force control on the fingers of a Jaco arm. Finally, I conclude the chapter and discusses future plans in Section 4.4.

4.1 Sensor Design and Fabrication

The proposed 3-D force sensor utilizes tri-axial measurement of the magnetic field vector created by a miniature permanent magnet embedded in a pyramid shaped silicone rubber body as shown in Fig. 4.1. Magnetic fields are measured locally using a Hall element on an embedded custom circuit board. The magnet is displaced under external forces, which creates a corresponding change in the 3-D magnetic field measurement. The sensor has a pyramidal shape, which ensures that the sensor contacts the environment mostly with its tip. In addition, the magnet is embedded deep within the pyramidal shape. This location is chosen to limit the motion of the magnet under off-center forces (to ensure that the magnet translates with minimal rotation).

The sensor is fabricated using a multi-stage composite molding process as shown in Fig. 4.2. For embedded electronics, a custom printed circuit board (PCB) was printed and etched. Standard circuit components and the Hall Effect IC (Melexis MLX90363) were soldered manually. The circuit communicates with a master device using the Serial Peripheral Interface (SPI) protocol. Once programmed, the circuit sends 8-byte messages of magnetic flux measurements in three axes with 14-bit resolution in each axis. An Arduino control board as the master data acquisition device was used and the information was sent to MATLAB where data processing is performed.

The first step of the fabrication process is bonding the custom PCB to an acrylic plate which has been cut into the shape of the PCB but with extensions on two sides. These extensions help maintain the orientation of the PCB during molding, after which they can be snapped off. The remaining acrylic provides a rigid base to the PCB. This custom acrylic PCB is assembled with two 3-D printed molds, which also includes an extruded negative of the magnet shape to create a cavity for the magnet. As silicone rubber (Smooth-On Ecoflex 0030) is cured in this mold assembly, the sensor is demolded, the magnet is placed in its place, and a layer of silicone rubber is injected in the cavity above the magnet to seal it completely within the sensor body.

A major concern in soft sensing is to ensure that the additional embedded components do not drastically modify the mechanical response of the soft body. To validate this property for the sensor design (comprising an acrylic plate, a miniature magnet, electronic components and silicone rubber substrate), a compressive testing of three prototypes was performed. The mechanical force-

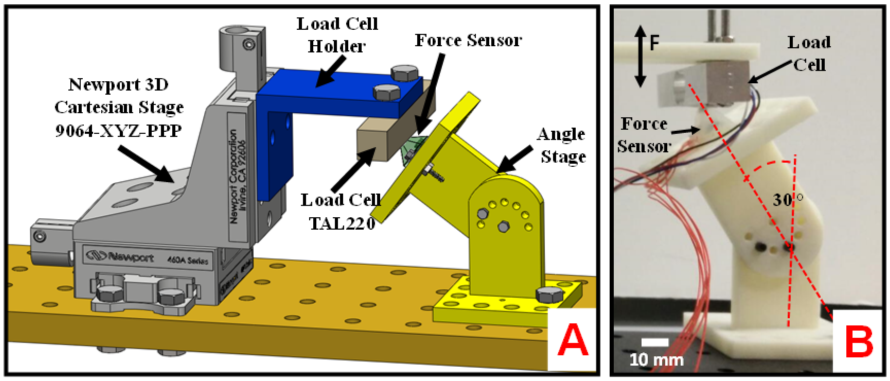
Load Cell
Holder
Force Sensor
Newport 3D
Cartesian Stage
9064-XYZ-PPP
Angle
Stage
Load Cell
TAL220
Newport Corporation
Irvine, CA 92606
Newport
460A Series
A
F
Load
Cell
Force
Sensor
30°
10 mm
B

Figure 4.4: Experimental setup for static loading shown as a CAD model (A) and the real system during operation (B). The force sensor placed below the load cell. The bottom stage can be rotated to a desired angle to create shear forces at a defined angle. Load generation on the sensor is achieved through lowering the load cell on the sensor by the motion stage. Thus, even though the load cell measures single axis force data, it is decoupled into normal and shear components using the angle set at the bottom stage .

displacement response of these complete prototypes to the material response of solid silicone rubber (Ecoflex 0030) was compared with the same geometry but without the embedded components. The results in Fig. 4.3 show that material properties are similar between different batches of the sensor. A significant change in material response due to the composite structure was not observed.

4.2 Learning Sensor Model using a Neural Network

A multi-layer perceptron (MLP) also known as fully-connected neural (FCN) network was used to learn the function space for sensor characterization. This function space is high-dimensional and nonlinear. For instance, the soft material deformation can be described using a hyper-elastic material model such as Mooney-Rivlin or Ogden, which requires multiple experimentally characterized parameters. In addition, since the relation between the magnet pose and magnetic flux is a nonlinear transformation, an analytical physics based model is intractable and a multi-physical finite element model may prove computationally expensive to operate in real-time. Thus, this work considers the use of MLPs to represent the sensor response under force loading.

Let $f_W(X_i)$ be the function that maps Hall Effect voltages to 3-D forces. The input space is the Hall Effect voltages measured by the sensor, where $\vec{X}_i = [V_x, V_y, V_z]' \in R^{3\times 1}$ and the force vector corresponding to these magnetic flux values is defined as $\vec{y}_i = [F_x, F_y, F_z]' \in R^{3\times 1}$. The goal of the network is to learn a set of weights W for f_W in the generic expression: $y_i = f_W(X_i)$.

4.2.1 DATA ACQUISITION

The training data was obtained by applying known forces on the proposed soft force sensor prototypes and then measuring the corresponding Hall Effect voltage readings. The applied forces were measured using a load cell (TAL220) and corresponding amplifier circuit (Sparkfun HX711). This setup measures loads up to 10 N with errors up to 5 mN. The load cell on a tri-axis Cartesian stage (Newport 9064-XYZ-PPP) was mounted as shown in Figure 4.4. An articulating base was designed and used to mount the sensor at desired angles with respect to the load cell, thus the force vector is decomposed into normal and shear components at known combinations. The load cell, the tri-axis stage, and the articulating base were made up of materials which do not interfere with the magnetic flux measured by the sensor.

Experimental data was collected from four different sensor prototypes. The data from three sensors were used to train the neural network and the fourth sensor was used for validating the network. Four different loading configurations were considered. These include pure normal force loading (at 0°), and shear loading at angles of 30°, 45°, and 60° with respect to the sensor normal. For pure normal loading, the sensor was subjected to a maximum of 1.1 N, and for shear loading the maximum load applied was 1.5 N. These limits were chosen based on the saturation range of the Hall element and the amplifier circuit and correspond to tactile contact-level forces. Data for forces at 45° shear loading was retained only for the validation dataset and was not part of the training data. This was to see how well the trained mapping function is generalized to forces at different loading conditions.

Table 4.1: MSE Loss in training during widening operation on Pyramidal Sensor

Number of Neurons in First Hidden Layer	2	4	8	16	18
MSE Loss (N^2)	0.0678	0.0325	0.0084	0.0045	0.0041

Table 4.2: MSE Loss in training during deepening operation on Pyramidal Sensor

Number of Hidden Layers	1	2	3	4	5
MSE Loss (N^2)	0.0041	0.0023	$7.07\text{x}10^{-4}$	$2.45\text{x}10^{-4}$	$1.16\text{x}10^{-4}$

Table 4.3: Results on the Test Dataset during widening operation on Pyramidal Sensor

Number of Neurons in First Hidden Layer	2	4	8	16	18
MAE (N)	0.23	0.13	0.092	0.053	0.052
Mean Error (N)	-0.0016	-0.0026	-0.0037	-0.0048	0.0039
σ(N)	0.2606	0.179	0.0917	0.0664	0.0632

Table 4.4: Results on the Test Dataset during deepening operation on Pyramidal Sensor

Number of Hidden Layers	1	2	3	4	5
MAE (N)	0.052	0.0258	0.015	0.007	0.0056
Mean Error (N)	0.0039	0.0028	0.0033	0.00094	0.00025
σ(N)	0.0632	0.0464	0.0262	0.0112	0.0092

4.2.2 LEARNING APPROACH

The technique used for learning the unknown mapping function was based on the Net2Net initialization technique[9], which performs learning in a sequential manner starting with small MLPs and then scaling the neural network up to a larger size in width and depth by using the previous smaller network as a teacher to the new larger student network. This approach avoids the usage of a very large initial network and then re-learning the entire network from scratch if the performance is not suitable. In addition, it was expected this approach would help avoid overfitting and provide mapping functions that generalized well to different loading conditions and sensor prototypes. The scaling of the network is performed by initialising the student network with the weights of the teacher network and then widening or deepening it. Widening involves adding additional neurons to a layer. Deepening involves adding a new hidden layer to the network. The advantage of the method is that it ensures that the student network improves upon the teacher network.

4.2.3 METRICS FOR EVALUATION

The neural network performance was measured using mean absolute error (MAE) and standard deviation (σ). Specifically, as each sensor data (X_i) is passed through the network, a prediction (p_i) is obtained and the error (e_i) is defined as the difference between this prediction and the actual force (y_i). $e_i = p_i - y_i$ where, $p_i = f_W(X_i)$. MAE and σ are calculated in standard form:

$$MAE = \frac{\sum_{i=1}^{N} e_i}{N}, \tag{4.1}$$

$$\sigma = \sqrt{\frac{\sum_{i=1}^{N} e_i^2}{N}}. \tag{4.2}$$

4.2.4 TRAINING, TESTING, AND VALIDATION

The total data points were split into training and testing datasets following the 80-20 convention. Data points obtained from the fourth sensor prototype and for 45° loading were excluded from this dataset.

The technique used for training all the Net2Net networks utilized the following hyper parameters. All the models were trained with Adam as the optimizer and mean-squared-error (MSE) was used as the cost metric to train the network since this is a regression problem. The learning rate was scheduled with initial value being the default $1e-3$ (for Adam optimizer). A reduction in learning rate by a factor of 10 was effected whenever the loss failed to reduce in 3 consecutive epochs. When the “Learning Rate Scheduler” function is evoked, the best weights (in terms of least loss) obtained until the function call are loaded and training is continued from there. Training was performed for 550 Epochs for each teacher network. Scaling of the network was done by widening the network first and then deepening it. Widening operation was done to a maximum of 18 neurons and then deepening operations were performed up to 5 hidden layers. The final network used for learning the sensor model contains 5-hidden layers with 18 neurons at each layer. The network implemented models using the software package Keras[11].

4.2.5 TRAINING RESULTS

The MSE obtained during training is shown in Table 4.1 (for widening operation) and Table 4.2 (for deepening operation). Data from Table 4.1 indicate that the training loss converges and does not improve from 16 neurons to 18 neurons during the widening operation. This is the primary reason why the widening operations were not pursued after 18 neurons. As hidden layers are added, the training loss is almost halved for every added layer. The reduction shows that the network is learning the function space effectively based on the training data. After adding the 5th hidden layer it was concluded that further increase in depth will be prone to overfitting. However, this does not provide any insight into the capability of the network to generalize for different loading conditions and sensor prototypes. Section 4.3.1 will demonstrate the response of the neural network for loading conditions and sensor prototypes that were not included in the training set.

4.2.6 Testing Results

Table 4.3 shows the results obtained on the test dataset during widening operations. As the neurons in the first layer were scaled, it was observed that the Mean Absolute Error (MAE) and the Standard Deviation (σ) were reduced. This decrease was very rapid initially and then slowly converged to steady state at a layer width of 18 neurons. Comparing the MAE results from the 16 Neuron and 18 Neuron architectures, we see that there was negligible difference between them. This pattern was also seen in the training data and this trend showed that further increase in the number of neurons would not provide better results. Hence widening operation was stopped at 18 Neurons and we move to performing deepening operations with 18 Neurons in each hidden unit.

Table 4.4 shows the results when deepening operation is performed while keeping the number of neurons in each layer constant at 18 Neurons. It was seen that MAE and σ are halved everytime a new hidden layer is added. Increase operation was stopped at 5 hidden layers as adding more layers would affect the time taken for prediction during test time. At the 5th layer, a MAE of 5.6 mN and a σ of 9.2 mN was observed which demonstrated strong prediction capability of the proposed network after both widening and deepening operations of Net2Net learning.

4.3 Experimental Results

To validate the accuracy and utility of the proposed 3-D soft force sensor and neural network based modeling approach, three sets of experiments were performed. First, known static and dynamic forces were applied on the sensors and compared the outputs from the neural network with the

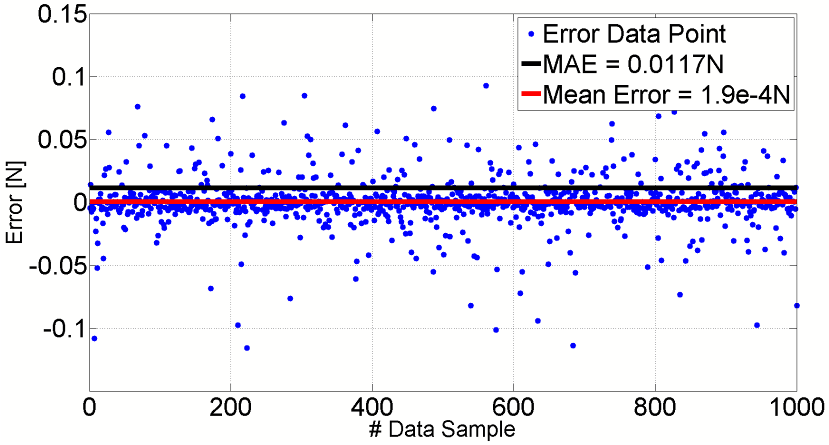

Figure 4.5: Validation Dataset Error Analysis

applied forces in a validation dataset. Next, a proof of concept force controlled pick and place experiment was performed using the proposed soft triaxial force sensor mounted on the gripper of a commercial robotic manipulator to demonstrate a usage scenario where this common manipulation task greatly benefits from real-time 3-D force measurements.

4.3.1 Static Validation Results

As previously discussed, the data obtained from the fourth sensor was not included in the training set and it was reserved for validation. The final neural network with 5 hidden layers was used to predict the forces for this sensor, and 1000 randomly sampled error points are shown in Figure 4.5. Figure 4.6 displays the actual forces (on the horizontal axis of these curves) that were applied on the sensor for pure normal loading, and shear (plus normal) loading at 30°, 45°, and 60°, all about the XZ plane and with the corresponding forces measured by the sensor using the neural network model (shown on the vertical axis). Only the relevant forces which were subject to change are plot-

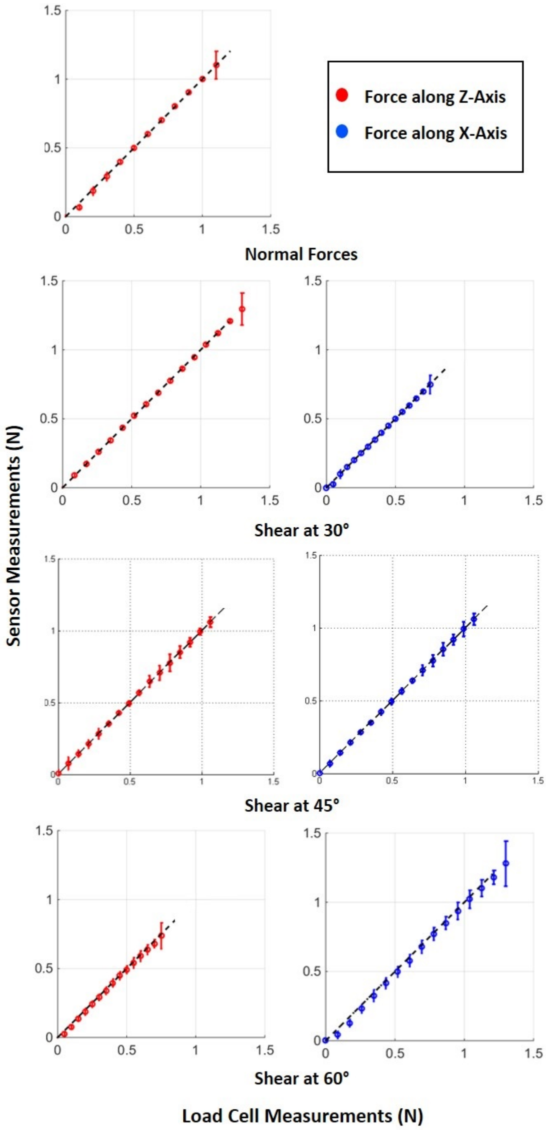

Figure 4.6: Forces measured from load cell are plotted on X-axis whereas forces measured from the soft force sensor are plotted on Y-axis. The circles represent the mean measurement value and a standard deviation for each point is also provided. The top row presents the Normal Forces case. The second, third, and fourth rows represent 30, 45 and 60 degree cases, respectively. Since the shear forces were applied in the XZ plane, forces along Y-axis and in Normal Force case can be omitted, which remain close to zero.

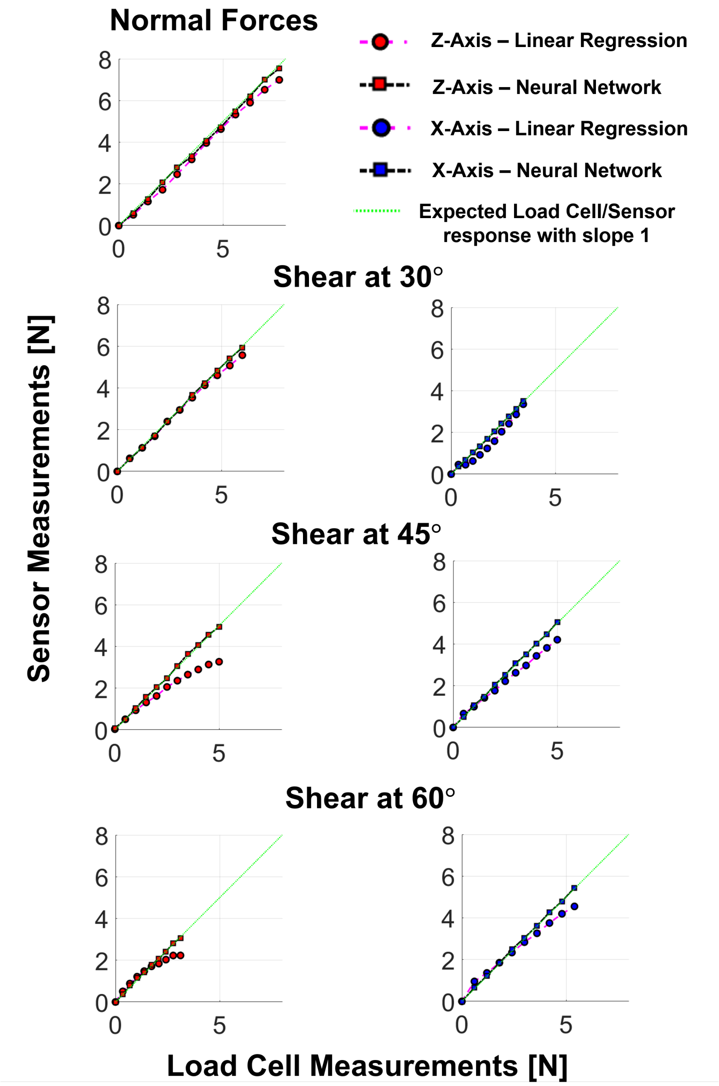

Figure 4.7: Pyramidal sensor with Dragonskin 30 as the soft substrate. The comparison of linear regression (dashed magenta lines with circle markers) and trained neural network forces (dash-dot black lines with square markers) are overlaid. Forces measured from load cell are plotted on the X-axis whereas forces measured from the soft force sensor are plotted on the Y-axis. The top row presents pure normal loading. The second, third, and fourth rows represent 30, 45, and 60 degree loading cases, respectively. Since the shear forces were applied in the XZ plane, we omit forces along Y-axis and in Normal Force case we omit forces along both X and Y axes.

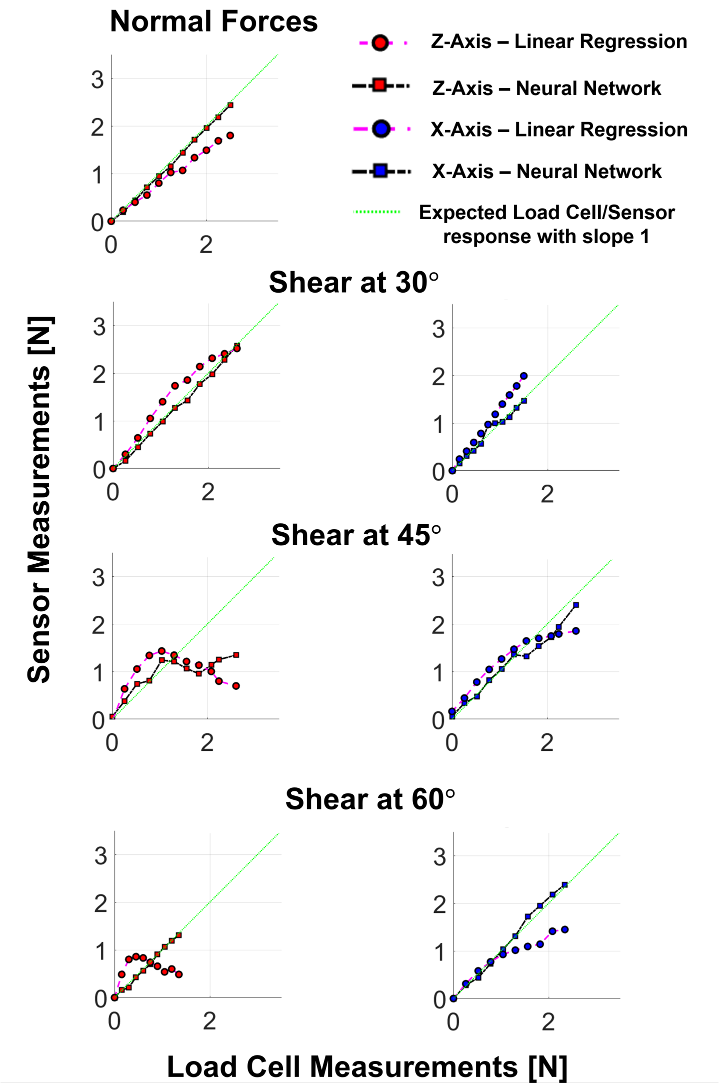

Figure 4.8: Rectangular sensor with Ecoflex 0030 as the soft substrate. The comparison of linear regression (dashed magenta lines with circle markers) and trained neural network forces (dash-dot black lines with square markers) are overlaid. Forces measured from load cell are plotted on the X-axis whereas forces measured from the soft force sensor are plotted on the Y-axis. The top row presents pure normal loading. The second, third, and fourth rows represent 30, 45, and 60 degree loading cases, respectively. Since the shear forces were applied in the XZ plane, we omit forces along Y-axis and in Normal Force case we omit forces along both X and Y axes.

ted in the figure (i.e. the shear measurements in Y-axis remain at zero and are not shown). We see that the actual to measured force curve closely follows the expected diagonal line with a slope of 1, thus showing that the applied forces are measured accurately by the sensor using the proposed neural network model. We also see that the deviation of the measurements from actual forces is minimal at low forces and more pronounced at higher loads. This could be due to the Hall element approaching the saturation limit and reducing its linearity between voltage to magnetic field values. A MAE of 11.7 mN was obtained on the magnitude of the forces on this dataset. Also, the FCN network is able to accurately measure the forces for shear loading at 45°, (a loading condition for which it was not trained and on a sensor prototype which was not included in training). From these experiments, it can be concluded that the network is able to generalize very well on new sensors and loading conditions. The time required for predicting forces during validation for each input vector (three Hall voltages) to the neural network was 0.34 msec and thus the FCN does not introduce time delay into the sensing system during real-time operation. One point we did not test was sensor response to coupled forces coming from edges of the pyramidal shape. Although the results obtained suggest that those cases can be learned as well, force measurements not acting along cardinal planes would be needed to verify the claim.

It is true that complex modeling schemes are usually undesirable and thus, there is a need to justify the choice of using a neural network model to calculate the 3-D forces from Hall voltage signals. To show neural network modeling is useful for soft force sensors with complex shapes and hyper elastic materials, sensor measurements from the neural network were compared with a simpler calibration approach, linear regression. The results are shown in Figure 4.7. Sensed forces from the

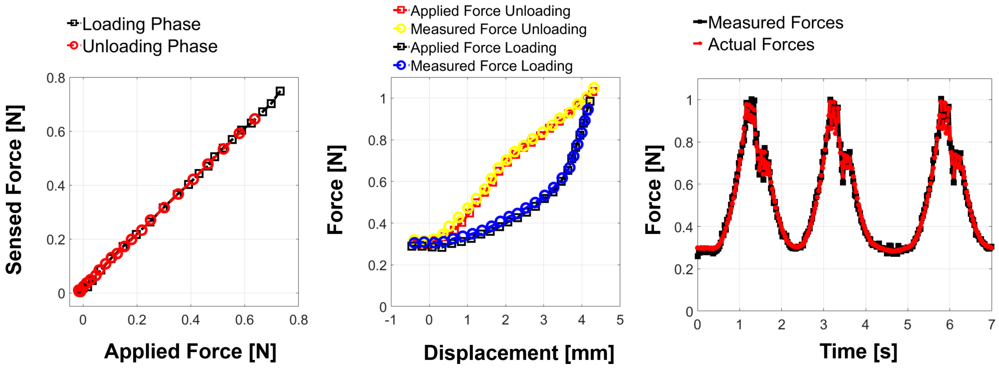

Figure 4.9: Dynamic testing results indicate that applied and measured forces follow a 1-1 diagonal (left). Hysteresis of loading and unloading for the applied and measured force-displacement data are in agreement (middle). The tracking of applied and measured forces during dynamic loading overlap in time axis (7 seconds shown from the 150-second experiment) (right).

FCN outperformed linear regression results in all cases. An MAE of 1.23 N was observed on the validation data when trained with linear regression. The MAE from the the neural network on the same dataset was 0.3014 N. In the 45° case, which was not included in the training set for either approach, linear regression significantly underperformed as well.

The sensor data shown in Figure 4.7 was obtained from a sensor made with Smooth-On Dragonskin 30 as opposed to Ecoflex 0030. Since Dragonskin 30 is a stiffer material, a corresponding increase in the measured force range is observed. The results indicate that the same neural network calibration approach adjusts well to different material types with the same sensor shape.

In addition, a justification is needed for the choice of using a pyramid shape for the sensor since it is more complex than a simple rectangular block design. To this end, the same set of experiments were made on a rectangular sensor design made from Ecoflex 0030 and kept the distance between the magnet and the IC surface same as in the pyramidal shape sensor and following the same calibration routine. Experimental results are shown in Figure 4.8. Just as with the Dragonskin 30 pyramid design, forces obtained from neural network are more accurate as opposed to linear regression where MAE on validation dataset was 0.1110 N and 0.2827 N, respectively. However, small deviations in 30°, 60° and a large deviation in z-axis measurement in 45° suggests rectangular shape to be undesirable for accurate force measurements. These deviations were attributed to free magnet rotations when pushed at an angle on the rectangular surface. The pyramid shape, on the other hand, allowed us to position the magnet near the centroid and reduce undesired rotations of the magnet, enabling repeatable and accurate force measurements.

4.3.2 Dynamic Validation Results

Dynamic loading experiments were performed using an Instron Electroplus-e1000 Linear-Torsion force testing instrument at WPI Biomedical Engineering Department. Only normal compressive forces were applied on the sensor and the frequency of the applied forces was set at 0.6 Hz (limited by the speed of the instrument) and the forces applied were between 0.3 N and 1.0 N as shown in Figure 4.9. The sensor was pre-compressed using a force of 0.3 N to eliminate any potential shifting of the sensor during the experiments. The application of dynamic forces on silicone rubber results in hysteresis due to viscoelastic effects (i.e. the deflection of the material differs for the same force during loading and unloading). The hysteresis plot is shown in Figure 4.9-Middle Panel. This curve indicates that the measured forces follow the actual force closely. In other words, the proposed sensor is able to map the effect of hysteresis very well and provide a measure of dynamic forces accurately. Figure 4.9-Right Panel shows the time response during a representative dynamic loading

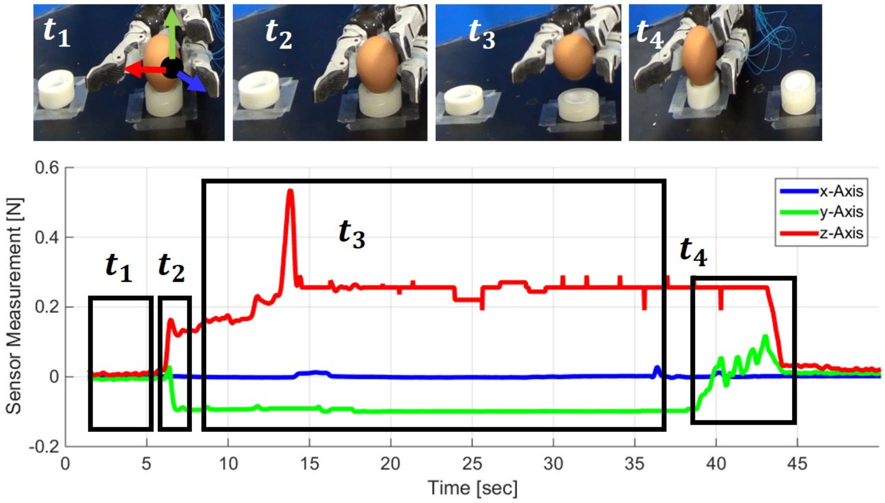

Figure 4.10: Significant time intervals from the grasp experiment are shown. At t_1 robot is at its initial state and no force is measured on the sensor. Shear force and normal force are detected as fingers get in contact with the object during t_2. The interval t_3 represents the movement of the object from initial point to the target point. The peak in this interval is due to stabilization of the egg between two fingers. Finally the object is released by detecting the change in y-axis force in interval t_4. A coordinate frame attached to the first snapshot at t_1 represents the measurement axes of the force sensor.

experiment, where the sensor output tracks the applied dynamic forces. The accuracy of dynamic force measurements is better inferred from Figure 4.9-Left Panel, which shows measured force with respect to corresponding applied force. Here we see that the relationship between the measured and applied forces follows a line with a slope equal to 1.0 with minimal variation.

4.3.3 Force Controlled Pick and Place Case Study

The proposed force sensor can be used to grasp soft or delicate objects with manipulators that are not designed to handle such objects. To demonstrate this application, a pick and place experiment with the Jaco arm (Kinova robotics, Boisbriand, QC, Canada) was performed for the purpose of grasping an egg. The arm is a 6-degree-of-freedom (DOF) manipulator with a 3-finger gripper. With the proposed soft tri-axial force sensor contact detection was done sensitively and thus the manipulator was able to transport the egg from one location to another without breaking it.

The arm was programmed to perform the pick and place task between two known locations on a tabletop. The goal was for the arm to sense the forces applied on the egg in real time to establish and maintain a gentle grip and release the egg when it touches the table top at the destination. The software to operate the arm was developed using Robot Operating system (ROS)[72]. The manipulator arm was configured to follow a trajectory in multiple phases. The corresponding forces measured in the phases are shown in Figure 4.10. Here, the sensor was placed on the finger pad, where normal contact forces coincide with the z-axis (local normal) of the sensor and gravity is along the y-axis (local shear). There are no expected forces along the x-axis, which is reflected in the measurements.

The gap in the gripper when fingers are fully closed was bigger than the size of the egg. Hence, the gripper fingers were padded with a silicone rubber layer in order to reduce this gap. The weight of the egg was 50 g. The arm could lift the egg without any damage following a simple force-control process as shown as snapshots in Figure 4.10. The four phases during this task are defined as follows:

Gripper Closing Phase: Shown by the period t_1 in Figure 4.10, here the gripper is at the initial pose and the fingers start closing. All forces remain at 0 N throughout this period, taking about 6 seconds before the fingers make contact with the egg.

Grasping and Lifting Phase: Shown by the period t_2 in Figure 4.10, here the gripper initiates contact with the egg as seen by the increase in F_Z. The fingers continue closing until a predefined threshold is reached to produce a normal grasping force between contact surfaces to hold on to the object due to friction, with negligible deformation. The value of the safe limit was determined through prior trials to be 0.15 N to 0.35 N (as measured by the force sensor) for the egg. After grasping the object, the arm starts lifting up the egg at around 7 seconds. In this phase, the force sensor experiences an increase in the shear force F_Y due to gravity.

Relocating Phase: Shown by the period t_3 in Figure 4.10, here the arm moves the gripper along with the egg over to a destination location while keeping the gripper position 10 cm above the desk level. Slight disturbances are seen in this time period which could be attributed to a shaky movement of the Jaco arm. The short pulse in this phase at 14 seconds coincides with a slight shift in the position of the egg between the fingers.

Placing Phase: Shown by the period t_4 in Figure 4.10, the gripper moves down towards the table. As the egg makes contact with the table top, the shear force decreases. This decrease in shear force allows the arm to recognise that the egg has been placed at the destination spot. At this time, the Jaco arm opens its grip to release the egg and the arm goes back to the starting position.

The sensing of the shear forces while placing an object helps the manipulator to sense that the object has made contact with the ground surface and allow it to place the object safely and gently at the destination spot without dropping the object or strongly hitting the ground surface.

4.4 Conclusion and Future Work

In this chapter I describe the design, fabrication, characterization, and experimental validation of a Hall effect based 3-D soft force sensor in a pyramid shaped soft elastomer matrix. For the scope of this work, we train a fully-connected neural network for characterization and mapping of measured

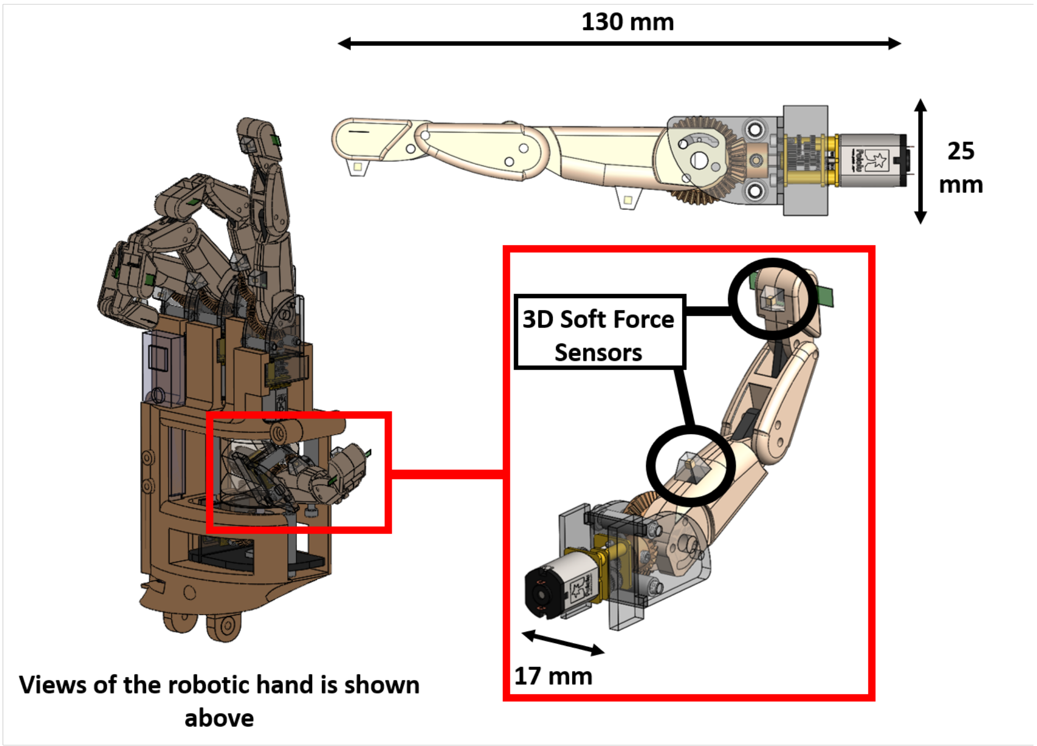

Figure 4.11: Complete 5-Fingered robotic hand is shown. All fingers are identical mechanisms. They are actuated by a single motor and curling motion is generated by two cascaded four-bar mechanisms. 3D Soft Force sensors attached to finger tip and body are shown in detail.

voltages to 3-D forces, in WPI Soft Robotics Lab. We show that the resulting mapping generalizes well for sensors and loading conditions that are not part of the training dataset. The experimental results show that the proposed sensor is highly accurate and it can measure forces in normal and shear directions within a range of 0 N to 1.1 N and ±1.5 N with an error of 2% and 2.2% of the full scale reading in normal and shear, respectively. The bandwidth of the Melexis sensor IC can work up to 400 Hz. Dynamic loading experiments indicate that the sensor is able to accurately follow dynamic forces applied at 0.6 Hz despite the hysteresis exhibited by the material.

A comparison of the pyramidal Ecoflex 0030 sensor with commercially available and published force sensor designs is presented in Table 4.5. Hysteresis in piezoelectric and capacitive commercially available sensors seems negligible but findings suggest viscoelasticity of soft materials adds significant hysteresis and therefore other works that use similar materials are expected to exhibit hysteresis effects. In most cases the range of the sensor can be adjusted by picking different soft materials or adjusting the gains of the amplifier attached to the sensor. The pyramidal Ecoflex 0030 sensor is quite sensitive, measuring forces as small as 5 mN (error range of the load cell used for calibration) within a suitable range of 0-1 N for tactile applications. In Table 4.5, Single Tact Sensor and embedded microfluidic channel based sensor design stand out as high sensitivity sensors within their maximum force range. Single Tact Sensor, however is only capable of measurements in a single dimension. As for sensitivity the Ecoflex 0030 Pyramid sensor (5 mN) is only outperformed by the commercial OMD-10 sensor (2.5 mN). In terms of package size the Ecoflex 0030 Pyramid sensor has a volume of 380 mm^3. Sensors having a smaller volume are Tekscan and Single Tact Sensor, which only provide normal force measurements. This volume difference is expected since both sensors are fabricated on a thin sheet and do not have soft substrates over them. Furthermore, package size of a magnetic force sensor can be decreased by picking even smaller magnets, changing the sensitivity of the hall element and reducing the distance between magnet and the IC. Overall, it can be concluded that the pyramid sensor shape, magnetic field measurements, and a soft substrate as the force measurement medium provides a good combination of size, measured axes, and sensitivity.

I mostly used a passive voice describing the experiments, design and results in this chapter, because the tri-axial force sensor idea was the first time where I managed a group of master students to publish results in a peer reviewed venue[21]. It was apparent to me when I designed the curvature sensor that the technical knowledge could be transferred into tactile sensing units. I also realized this was a challenge where grasping, manipulation and legged locomotion could benefit from. However, contrary to curvature sensing, force sensing via elastic materials and Hall Effect units was already published in the literature. Therefore, we wanted to push the limits of this sensing modality and I guided two masters students, of which one was interested in machine learning techniques to real robotic problems, to come up with results. We also tested a new shape (pyramidal soft substrate) for accurately sensing forces and obtained promising results as compared to rectangular or semi-spherical shapes.

In WPI Soft Robotics Lab, one of our philosophies is to test the systems we create for practical purposes, as demonstrated in my soft module control work. As for the force sensor we performed a simple pick and place experiment on an egg using the force sensor mounted on a Kinova Jaco arm. We showed that the sensor provides stable output force data in real-time and we can use both shear and normal force data to successfully perform fragile object manipulation.

The single experiment done with the simple Jaco Manipulator was not as rigorous as we wanted. We included these preliminary results along with the sensor design[21]. To demonstrate that the force sensor was capable of improving grasping performance I recently conducted additional tests with the force sensing unit on a custom robot manipulator design.Its finger and assembly can be seen in Figure 4.11. I briefly show, in Figure 4.13 multiple results on how shear detection can be algorithmically introduced to pick and place operations and how it improved task quality by detecting contact during placement phase.

Snapshots in Figure 4.12 indicate important events during the grasp execution. Experiment set-

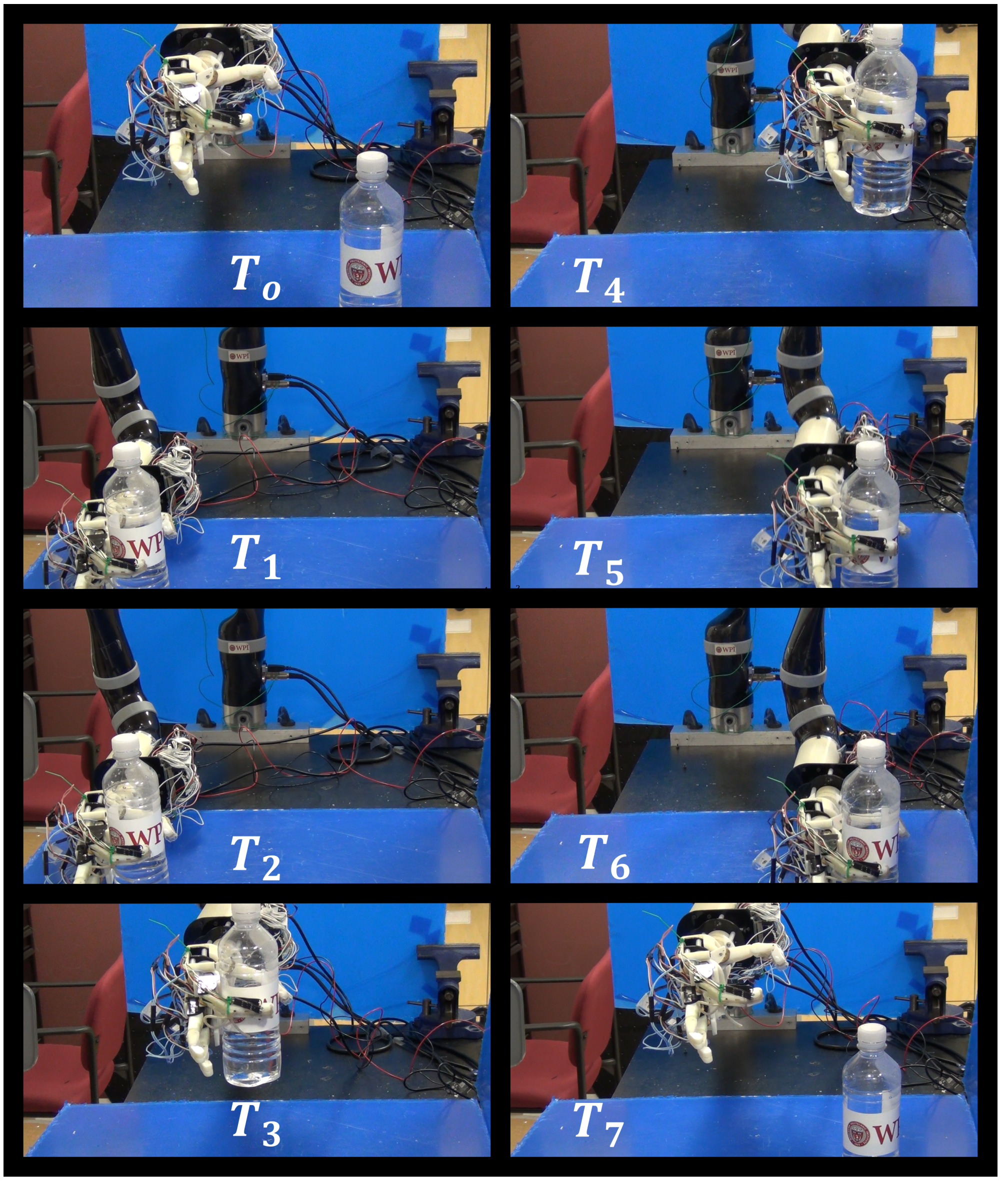

Figure 4.12: Snapshots from grasp experiment are shown. T_0 shows the initial state of the experiment. Hand is moved to the vicinity of the object in T_1. Grasp is initiated and gripper is on-state at T_2. Object is lifted at T_3, shear force increase is observed at this state. Object is moved on air and position to the placement location at T_4 and T_5. Decrease in shear force is captured at T_6 and gripper is turned into off-state. Finally, robot hand is positioned back at the initial state in T_7.

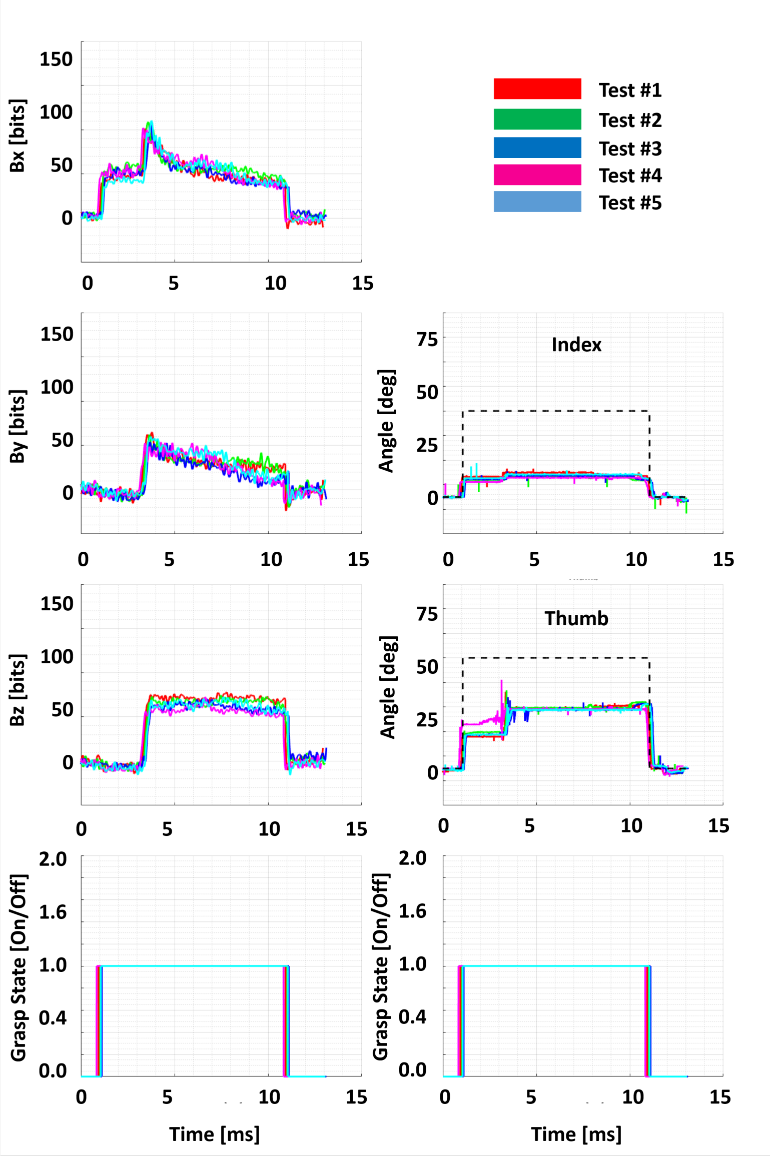

Figure 4.13: Figures on right column show desired angle for thumb and the actual angle measured by joint potentiometer. They are not reaching the commanded angle value due to being in contact with the object. Figures on left column show magnetic field measurements from the 3D sensor. Finally last rows on both columns show whether gripper is in its on/off state. Shear is detected once object is grasped by checking a threshold on B_z measurement. As soon as ground contact is made B_z drops and gripper transition into off-state, autonomously.

tings consists of the Jaco robot arm, our custom designed robotic hand is attached to it, and there is a water bottle. The objective is to grab the water bottle and place it to another pre-determined location, graciously. As we will see, if shear forces measured by the tri-axial force sensor are utilized, the ground contact can be detected and the object can be released without forcing it into the table. In Figure 4.13, the bottom two figures show the gripper on/off state.

Here, I go over the important stages of the pick and place experiment. At t_0 and t_1 gripper is approaching the water bottle and gripper state is turned off. In t_2 gripper state is turned on. Increase in measured magnetic field strengths in axial axis Bx is observed along with a delayed increase in By and Bz values. The delayed increase in measured values correspond with bottle being lifted from the table marked as t_3 in Figure 4.12. Bottle is in contact with the ground at t_6 and the decrease in shear forces is observed by checking whether Bz field magnitudes is lower than a constant threshold value. As soon as a sudden drop is observed, gripper state is turned off and object is released. The gripper turn off instance and drop in Bz values are coincident in Figure 4.12. When the same experiment is performed without a check on measured Bz values, the gripper does not release the object with decrease in shear forces. This behaviour can be observed in Figure 4.14. The gripper stays on for a constant amount of time in all experiments after a significant drop in the measured Bz field is observed. More clearly, this means that manipulator is forcing to push the object into the ground because it is oblivious to ground contact and fails to open the gripper appropriately at contact.

Having shown the capabilities of novel soft mechanisms, next chapter will focus on how I use my previous experience to come up with a new compliant leg design for dynamic locomotion.

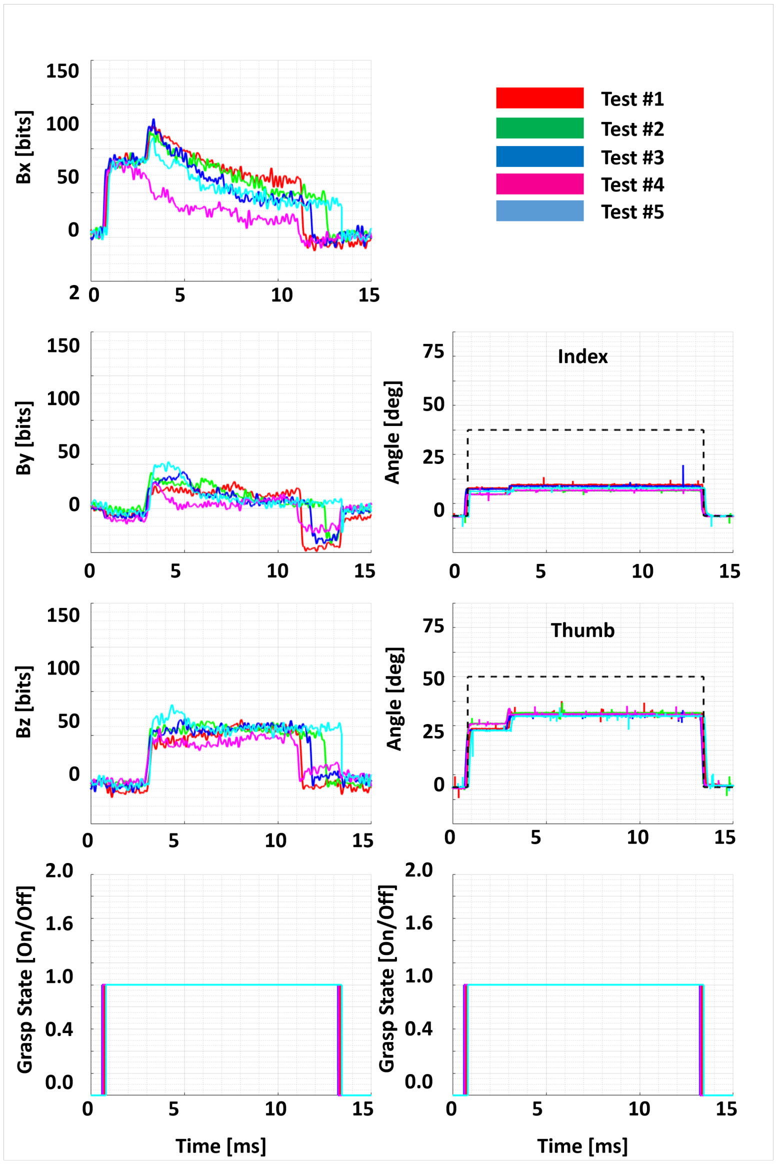

Figure 4.14: Similar to previous figure, left column shows desired angle for thumb and the actual angle measured by joint potentiometer. Right column shows magnetic field measurements from the 3D sensor. Notice that gripper states are not turned off when ground contact is made due to lack of shear detection threshold on B_z measurements.

Table 4.5: Comparison of commercial and published force sensors along with the Pyramidal Ecoflex 0030 sensor presented in this chapter along important properties of size, sampling rate, hysteresis, measured force axes, range and sensitivity.

Sensor Name	L×W×H (mm)	Sampling Rate	Hysteresis	Decoupled Force/Torque Axes	Range (N)	Sensitivity
Tekscan (A101)	15×7×0.2	200 kHz[*]	4.5% FS	1	44	No data provided
Single Tact Sensor	58×8×0.35	1000 Hz	4% FS	1	10	20 mN
OMD-10-SE-10N	15×11×10	1000 Hz	2% FS	3	$Fz = 10$ $Fx = \pm 2.5$ $Fy = \pm 2.5$	2.5 mN
Embedded Microfluidic Channels[95]	50×60×7	100 Hz[†]	Negligible[‡]	3	$Fz = 6$ $Fx = \pm 1$ $Fy = \pm 1$	10 mN
Tomo et al.[88]	55×55×8	100 Hz	No data provided[§]	3	$Fz = 15$ $Fx = \pm 6$ $Fy = \pm 6$	No data provided
Nie et al.[60]	Diameter: 60×11	400 Hz	No data provided	4	$Fz = 40$ $Fx = 15$ $Fy = 15$ $Tz = 0.8$	10 mN
ATI Nano17	Diameter: 17×14.5	7 kHz	No data provided	6	$Fz = 17$ $Fx = 12$ $Fy = 12$	3 mN
Liu et al.[44]	Diameter: 20×8	5 kHz	No data provided	3	$Fz = 0.5$ $Fx = 0.5$ $Fy = 0.5$	10 mN
This Work: Pyramidal Ecoflex 0030	12×12×8	400 Hz	Negligible[¶]	3	$Fz = 1.1$ $Fx = \pm 1.5$ $Fy = \pm 1.5$	5 mN

[1] The value is based on the response time of the piezoresistive material. The bandwidth may vary for different uses.

[2] Reported sampling rate.

[3] The material will exhibit viscoelastic properties.

[4] The material will exhibit viscoelastic properties.

[5] The pyramid sensor exhibits negligible hysteresis for force measurements. A higher hysteresis of 24% is observed in force-displacement response. This behaviour is due to the viscoelastic nature of the material.

5

Compliant Leg Mechanism Design

The classical Raibert Hopper, is an impressive mechanism. Not because of its mechanical complexity but because of its simplicity in achieving a challenging task: e.g. running with legs. It is also of natural interest to a researcher in my position, who has experience in both legged locomotion and soft robotics, to investigate the merit of compliance in its design. The novel leg mechanism design described in this chapter connects and concludes my previous work on soft sensing, actuation and control in two ways: I) a flexible and resilient folded leg is manufactured by step-by-step molding process used for soft sensors and actuators fabrication, II) the force sensor described in the previous chapter is utilized to detect contact states hence enabling reliable switching between different parts (states) of the Raibert controller. Instead of simply integrating the proposed compliant leg, I present experimental evidence on improved efficiency during legged locomotion contributed by the integrated compliant leg. Additionally, I point out the relevant vertical hopping literature to explain the increase in efficiency.

One of the challenges in soft robotics is integrating new material design and fabrication approaches into the existing body of knowledge. This challenge is also important to a researcher in the field because soft robotics has the potential to overcome the mismatch between mechanical compliance of organic life and traditional robots[48]. The recent soft robotic publications[80,24,46] are laudable in terms of their novelty towards that potential. These robotic devices are extremely flexible thus making them safe to interact with. They conform to their surrounding environment, giving them the potential to move into spaces that were once deemed impossible. As another example, soft robotic skins[?] have the potential to change how tactile data is measured and obtained in the decades to come.

However, efforts on making robots softer and more compliant do not always translate well into the real life by generating useful motions or improve our understanding of how to engineer more agile mechanisms. This is not a limitation of researchers but a natural result of our effort to understand and mimic nature. Usually, understanding nature comes with a challenge whose solution is

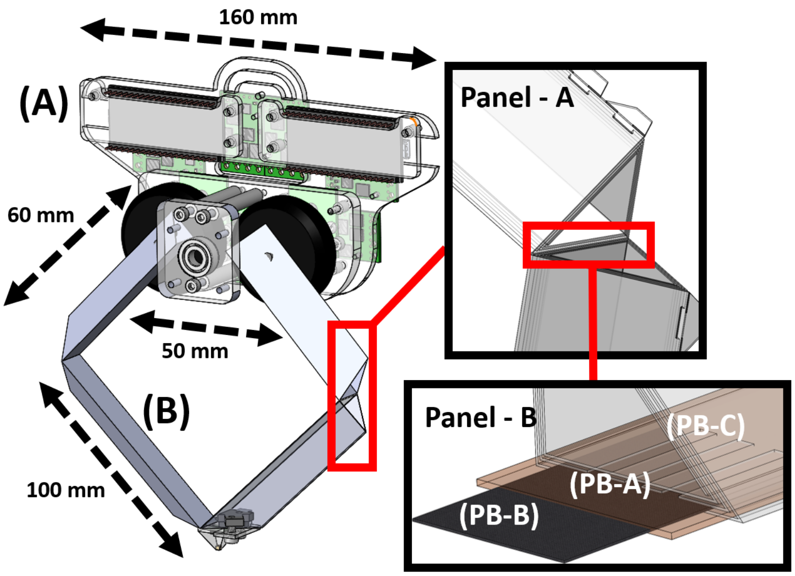

Figure 5.1: Left CAD figure shows the overall hopper mechanism where **(A)** represents the controller board, motors and motor drive circuitry attached to the robot body; and **(B)** represents the fivebar leg mechanism driven by two independent BLDC motors. **Panel-A** shows the origami inspired triangular beam & joint design. **Panel-B** shows the fiber reinforcement layer to the joint in detail. Cuts **(PB-A)** are made between two of bases. Fiberglass cloth **(PB-B)** is mounted on the cuts before folding and covered with Simpact 85 Urethane rubber **(PB-C)**.

easy to verify but difficult to solve. Unfortunately, overemphasis on this fact of nature can lead to less than desired results. For example, despite their significant contributions, the soft quadruped designs[87,85] do not help us understand how to engineer agile robotic systems inspired by biological mammalian quadrupeds. Thus, there appears to be a gap between advances in soft robotics and their integration with the rest of the knowledge in the greater field of robotics.

Some unique soft robotic systems have the potential to create new capabilities that are simply not possible with a rigid body. A good example for a soft machine that exhibits new useful behavior is the universal gripper[6]. Using a deformable design, it provides a convenient solution to the problem of grasping, which is traditionally believed to be algorithmically complex. Another example is the robotic fish[?] , which generates a new motion type with simple algorithms due its utilization of mechanism compliance and softness. However, these examples are rare, and the problem of finding useful, interesting, and new ways to integrate materials into robots remains challenging and important.

The main goal of this chapter is to demonstrate how existing theoretical and practical knowledge in the field of hopping robots can benefit from novel mechanical design approaches: namely soft robotics and origami based foldable mechanisms. To this end, I create a compliant leg mechanism inspired by a modern hopper leg design[15]. Instead of using standard mechanical components for constructing the leg, I use an origami-inspired foldable approach to create the leg body and added fiberglass mat between plastic layers of the origami sheet to increase the leg strength. Figure 5.1 shows the CAD concept of the proposed leg design with plastic layers and fiberglass reinforcement. To my surprise the weight of the foldable leg is significantly lower than a rigid leg machined from acrylic pieces and assembled using standard mechanical components. Moreover, the rigid leg is not as efficient as the foldable/flexible counterpart during jumping experiments. This is an expected result due to the dynamics of hopping[55] which favors elastic energy storage to increase efficiency. The benefit of the fiberglass-reinforced foldable leg design is that the mechanism possesses inherent elasticity around a neutral shape due to the addition of the fiberglass layer without the need for additional spring elements as commonly used in dynamic legged locomotion.

I experimentally demonstrate that the proposed leg design results in superior performance, in terms of efficiency, compared to a rigid counterpart. The mechatronic system I use to conduct ex-

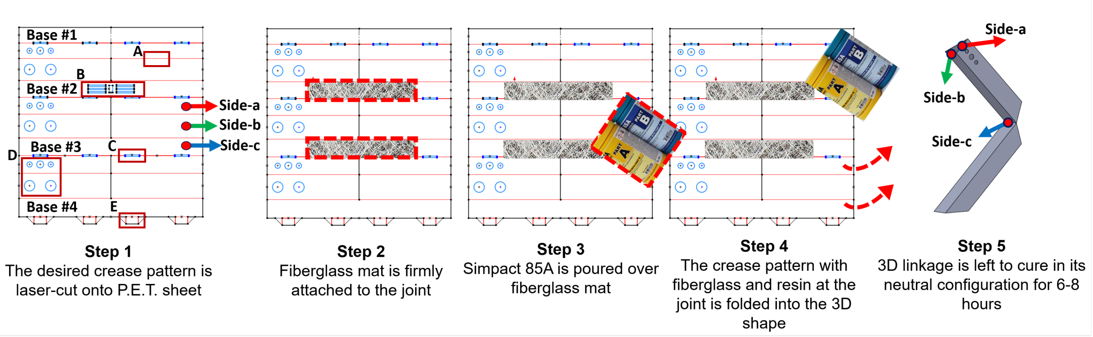

Step 1
The desired crease pattern is laser-cut onto P.E.T. sheet

Step 2
Fiberglass mat is firmly attached to the joint

Step 3
Simpact 85A is poured over fiberglass mat

Step 4
The crease pattern with fiberglass and resin at the joint is folded into the 3D shape

Step 5
3D linkage is left to cure in its neutral configuration for 6-8 hours

Figure 5.2: Manufacturing steps are shown starting from left and ending at the rightmost panel. The A, B, C, D, E labels in Step 1 demonstrate; fold lines, opening for resin to pass through layers, holes for placing the locks, mounting circles to the rotor of the BLDC and locks to keep the fold intact. Side a-b-c of the triangular beam are shown in 2D crease pattern at Step 1 and their respective positions in the 3D structure are shown in Step 5.

periments is inspired by Raibert's original 2D hopper mechanism[75]. I also provide a theoretical background for the experimentally observed performance improvements. I go over the details of the controller and the mechatronic system that implements it.

The main contributions of this chapter are as follows. I introduce a novel leg mechanism: a folded, fiberglass-reinforced, compliant leg design. It is designed to work with hopping robots where relatively high frequency (5-10 Hz) impact exists with loads ranging between 0.3-0.5 kg. The results from the new mechanism are experimentally validated and compared with a rigid counterpart. The folded leg design exhibits compliance, which results in %189 improved mechanical efficiency over jump cycles, and it has a lower leg mass (20-25 g) compared to its rigid counterpart (70-80 g). The secondary contributions can be stated as making a theoretical and practical link between novel robotic manufacturing trends, such as origami and soft robotics, with dynamic legged locomotion and modern system design for hopping platforms. Especially the soft-bodied, tri-axial force sensor recently presented by our group[21] plays a crucial role in contact detection and I experimentally demonstrate that soft force sensors find practical use in settings with frequent and heavy loading.

It is convenient for readers to address what I mean by origami design and soft robotics while presenting them as novel mechanical design and fabrication approaches. Origami based design can mean multiple things. For example, origami inspired structure is utilized[5] to create a modular robot. In this chapter when I write origami based design what I mean is using 2D crease patterns, which can be folded into 3D shapes, to create mechanisms. My use of the word is similar to designs pioneered by Onal et al.[67]. Similar to origami design patterns, soft robotics covers a wide range of meanings due to the rapid popularity it has seen in recent years. I embed a fiberglass mat and a soft resin into the origami structure via manufacturing techniques inspired by recent developments in soft robotics. It is common knowledge to use molds to create organic, complex, flexible/soft shapes[35]. In my leg mechanism, the origami structure becomes the mold where I cure a soft polyurethane and fiberglass cloth together. Resulting mechanism exhibits elasticity at joints with a desired neutral angle, which is useful for passive energy storage during the stance phase.

5.1 Compliant Five-bar Leg Design

A five bar linkage is a suitable 2 degree-of-freedom (DoF) mechanism for planar manipulation. It is possible to mount two independent motors and drive the end effector to Cartesian coordinates within a workspace. In the following, I first explain the details on how to build a lightweight, compliant and folded five-bar mechanism using our proposed approach. Next, I go through the kinematic optimization process of the mechanism for a 2-DoF hopper leg, which presents a nontrivial optimization problem to find a set of link lengths that reach a desired workspace with a well-behaved Jacobian.

Manufacturing Details

I use 2-D crease patterns to generate 3-D shapes by folding. In particular I use patterns to create triangular beams, which are used as links of the leg design. A simple 2-D pattern of three rectangles stacked coincidentally is sufficient to create a triangular shape which is geometrically stable when folded. Lock and key features are included at the connecting edges of the rectangles to affix the structure in its folded and final 3-D shape. The outer layers of the rectangle are laser machined onto a polyethylene terephthalate (PET) film using an Epilog Zing laser engraver. Fold lines are cut in perforations to mark creases with reduced stiffness and make manual folding convenient. The fundamental design concepts behind the way in which I use origami in robotic structures are explained in detail in previous work from our group[66]. Recent examples of folded robots[83,2] show how similar linkage and joint design patterns via origami can be applied to a hexapod. A more recent work[77] extends the foldable design pattern to continuum manipulators.

The next challenge is figuring out how to integrate links in series by joints. A flexure fold joint is designed to connect two separate rectangular patterns. This method generates a structure that functionally acts like a revolute joint, when folded. Moreover, I increase the number of rectangles surrounding the joint to add second or third layers to the structure. In other words, the link has a triangular cross section with multiple triangles stacked radially together by wrapping multiple layers of folded plastic. This stacked pattern makes it structurally stronger. The 2-D crease pattern of two links connected by a joint and its relevant features are shown in Figure 5.2 along with a 3D model of its folded shape. The full crease pattern of the five bar is just a serial connection of the shown crease pattern with appropriate link lengths.

A foldable leg design made out of PET for a jumping robot weighing 0.5-1.0 kg is a significant and novel challenge. Making the legs as light as possible is crucial in legged locomotion to reduce inertial effects and in an autonomous application where battery life is a concern. However, my preliminary work has shown that this idea is not feasible with the original approach utilizing pure origami folding of plastic films. The joints are too weak to handle high frequency (5-10 Hz) mechanical impacts and they get torn easily even with multiple layers.

One way to strengthen the mechanism is trying to increase the number of folded layers. Unfortunately, increasing the number of layers indefinitely is not a realistic option for two reasons. First, it becomes increasingly difficult to fold a linkage mechanism with more than three layers; second the size of the crease pattern increases with the number of layers, making the pattern exceed the area limitations of the laser cutter. Therefore another approach is required if one wants to benefit robotic legs from the lightweight design patterns of origami.

My proposed approach for adding strength to the leg mechanism is embedding fiberglass (3M Bondo) in between folded layers of the PET sheet during the fold process. However simply mounting the fiberglass is not an option. Without curing the fiberglass in a material that acts as a resin, it wouldn't add extra strength let alone keep its shape intact. The suggested resin for the fiberlass mat makes the composite material too thick and rigid, and hence, the folded structure loses its flexure joint properties. Through experimenting with different resin candidates I found Simpact 85A polyurethane rubber from Smooth On (Shore Hardness 85A) to be a good fit. It significantly increases the strength of the joint while maintaining its flexural property. Manufacturing steps of integrating a folded structure with fiberglass mat and resin are as follows: 1) A 2-D crease pattern is lasercut on PET film with 0.17 mm thickness. 2) Small pieces of fiberglass mat are attached to coincide with the flexural fold joints. 3) Simpact 85A is poured on fiberglass mat. 4) The crease pattern is folded to its 3D shape to allow Simpact 85A to be distributed to all layers inside the pattern, completely covering the fiberglass mat. 5) The 3-D form is left to cure for 6-8 hours at room temperature.

The resulting mechanism exhibits stronger joints with inherent compliance at a lighter weight (20-25 g) compared to a rigid mechanism design (70-80 g) made from laser-machined acrylic sheets and standard mechanical components.

KINEMATICS

Several points were taken into account while designing a leg with desired kinematics, which can be seen in Figure 5.3. The five-bar linkage kinematics is non-trivial due to the complex mapping between input angles ϑ_2 and ϑ_5 to the knee angles. Even though close form solutions of ϑ_3 and ϑ_4 exist[62], they alone are not enough to obtain a set of link lengths for mechanism design. Throughout the chapter I use the standard variable convention described by Norton[62] for convenience. A sketch of five-bar angles is also given in Figure 5.4 for further clarification.

As I will explain in Section 5.2 the jumping controller used in this chapter can be kinematically reduced to a revolute-prismatic (RP) manipulator, whose workspace can be defined with two param-

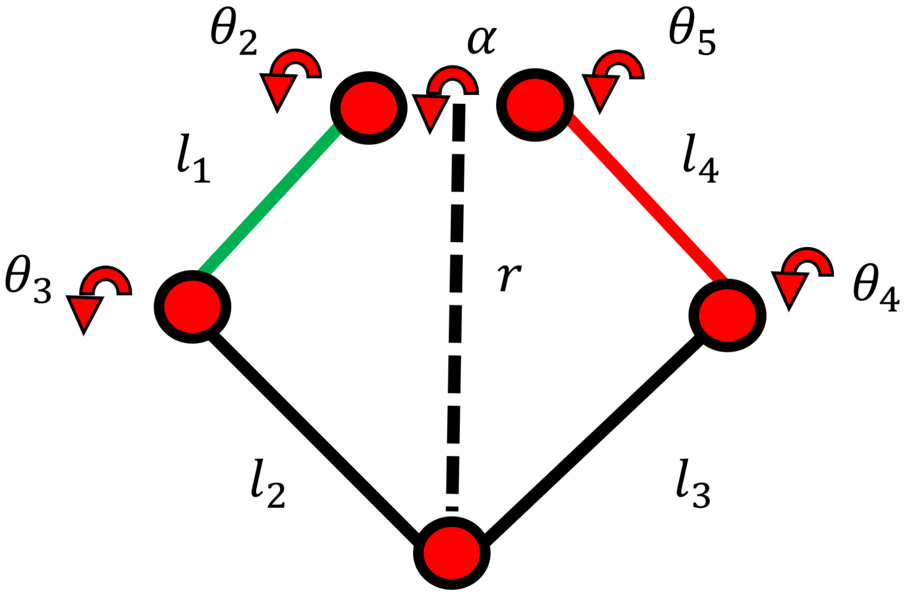

Figure 5.3: Relevant angles and link lengths are shown. α denotes angle of the RP manipulator and r its length. The ϑ_i values are input and output angles of the fivebar mechanism. Whereas l_i denotes fivebar link lengths.

eters (in polar coordinates): α for joint angle and r for radial displacement. The tip of the five-bar mechanism ideally needs to be able to reach all points within the minimum and maximum limits of α and r in a desired workspace.

Once a good match between the ideal RP and five-bar workspaces is obtained, the Jacobian of the five-bar mechanism should also be examined. It is well known that a mechanism loses its ability to apply independent forces in Cartesian space near singularity. Furthermore, all contact forces act along the prismatic joint in the RP manipulator but that is not the case for the five-bar mechanism. To avoid having instabilities between input torques and output forces, a well designed five-bar leg should not magnify the small changes in the joint spaces to the Cartesian space.

I use the condition number[84,57] of the Jacobian to check if the force-to-torque response of the mechanism is well behaved and find the set of link lengths that will minimize the integral of the condition number computed over ϑ_2 and ϑ_5. The limits of the integral are determined by upper and lower values of α and r.

The condition number $\varkappa$ is defined as:

$$\varkappa(J(\vartheta_2, \vartheta_5)) = \left\| J^{-1} \right\| \left\| J \right\|, \tag{5.1}$$

where ϑ_2 and ϑ_5 are five-bar input angles, J is the 2×2 Jacobian matrix and $\|\dot{}\|$ is chosen as 2-norm.

I compute,

$$G = n^{-1} \sum_{r=r_{min}}^{r_{max}} \sum_{= \quad min}^{max} \varkappa(J) \tag{5.2}$$

for all values of α and r. The mapping between RP manipulator space parameters and ϑ_2 and ϑ_5 can be computed via well known inverse kinematic methods, such as using inverse Jacobian or its transpose. The function G denotes the sum of all condition numbers over the RP manipulator workspace. The number n denotes total number of points in the workspace. Note that n depends on the discretization of the workspace and its limits. Finally α_{min}, α_{max}, r_{min} and r_{max} denote limits of the RP workspace.

Since the optimization problem above is too complex to have a closed form solution I perform a numerical analysis over the upper and lower link lengths of the five-bar linkage. Note that the search space is significantly reduced if five-bar link lengths are assumed to be symmetric. The optimization

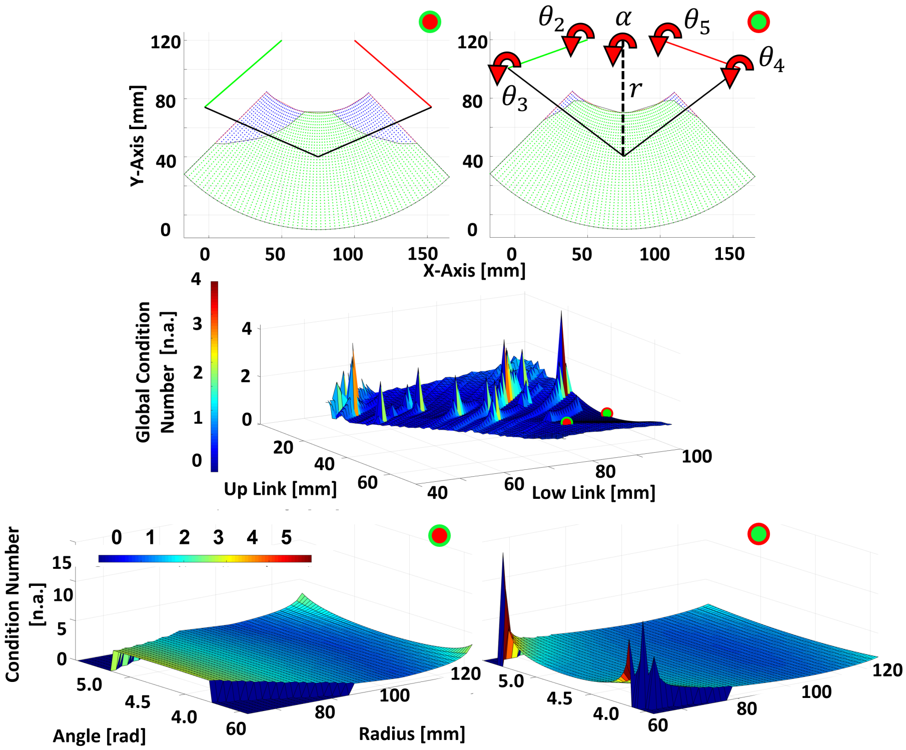

Figure 5.4: The middle row shows the global condition number (G.C.I.) for all link lengths bounded between a minimum and a maximum number. The initial design choice is marked with green outline circle on the surface. The minimum value of the G.C.I. is obtained at the circle with red outline. Top and bottom figures show Cartesian workspace and condition number of the initial design choice and the link lengths resulting in minimum G.C.I., respectively.

results and graphical representations of relevant parameters are provided in Figure 5.4. The set of link lengths obtained from the minimum value of the G function results in 58 mm and 100 mm for upper- and lower-link lengths. The initial design set I manually determined, 62 mm and 89 mm for upper/lower links, resulted in slightly reduced reachable area and higher condition numbers throughout the workspace.

5.2 VERTICAL JUMP THEORY AND RAIBERT CONTROLLER

PLANAR VERTICAL JUMP

Koditschek[36] discusses the dynamic behaviour of vertically hopping mechanisms. A hopping robot in a single axis can be described by two separate dynamic systems switching between a spring-loaded mass model and a free-fall model. The switch mechanism depends on the state vector of the system. Typically, such systems are called hybrid dynamical systems[16]. I use the following system definition to show the effect of active impedance on the efficiency:

$$\mathrm{f_{bf}} = \begin{bmatrix} 0 & 1 \\ 0 & 0 \end{bmatrix} \mathrm{x} + \begin{bmatrix} 0 \\ -g \end{bmatrix} \tag{5.3}$$

$$\mathrm{f_{gls}} = \begin{bmatrix} 0 & 1 \\ -\frac{k}{m} & -\frac{b}{m} \end{bmatrix} \mathrm{x} + \begin{bmatrix} 0 \\ -g \end{bmatrix} \tag{5.4}$$

$$\mathrm{f_{dct}} = \begin{bmatrix} 0 & 1 \\ 0 & -\frac{b}{m} \end{bmatrix} \mathrm{x} + \begin{bmatrix} 0 \\ \frac{F_{in}}{m} \end{bmatrix}, \tag{5.5}$$

where the functions f_{bf}, f_{gls} and f_{dct} depict systems of differential equations representing ballistic flight, gravity-loaded spring, and damped constant-thrust phases of vertical hopping. The parameters m, b, k, and g represent mass, damping, spring coefficient, and gravitational constant, respectively. The state vector $\mathrm{x} = \begin{bmatrix} r, \dot{r} \end{bmatrix}^{\mathsf{T}}$ contains spring length and its time derivative. Note, I keep the

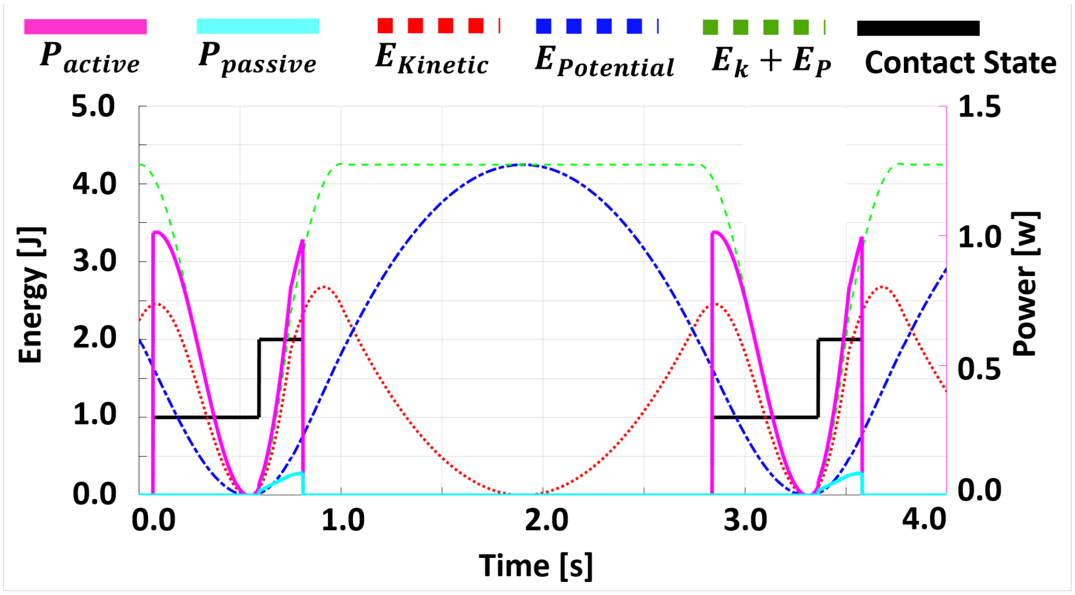

Figure 5.5: The energetics of a vertical hopper is shown. Black solid line is the system mode (flight (0), stance (1) or thrust(2)). Dotted red curve is the kinetic energy and dash-dot blue curve is the potential energy. Note that their sum is constant throughout flight and decreases during stance. This is because I do not include spring energy inside the potential term. The solid magenta line P_a indicates input power during stance for active compliance. The input power to system consists of spring component and a thrust component. The solid cyan line P_p is the power input to the system with passive compliance and it is only composed of thrust force required to regain lost energy due to losses at jump.

notation consistent with the RP workspace discussed in the previous section. Thrust is injected during f_{dct} phase via F_{in} for a constant time interval. Transition between phases f_{bf} and f_{gls} is achieved via guard function $g(\mathrm{x})_i = r$ and transition between f_{gls} and f_{dct} is guaranteed via $g(\mathrm{x})_{ii} = \dot{r}$. After F_{in} is applied in f_{dct}, the system can reset back to f_{bf} or f_{gls} depending on its state. The flows with discrete transition can be used to describe the hybrid dynamics of vertical hopping.

Here, I make a distinction between active and passive impedance. If the system has only passive impedance, which means that the leg contains spring elements, the only power input to the system is during f_{gls} via the F_{in} term. On the other hand if actuators are to generate a spring-like effect, then

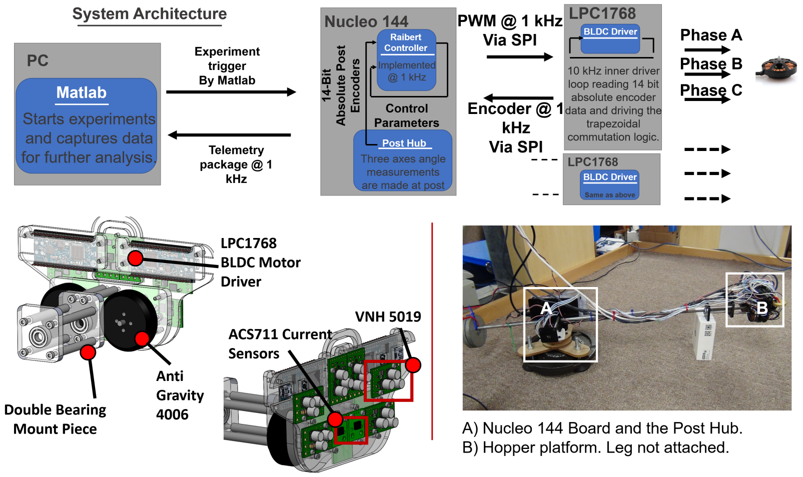
System Architecture
PC
Matlab
Starts experiments and captures data for further analysis.
Experiment trigger By Matlab
Telemetry package @ 1 kHz
Nucleo 144
14-Bit Absolute Post Encoders
Raibert Controller
Implemented @ 1 kHz
Control Parameters
Post Hub
Three axes angle measurements are made at post
PWM @ 1 kHz Via SPI
Encoder @ 1 kHz Via SPI
LPC1768
BLDC Driver
10 kHz inner driver loop reading 14 bit absolute encoder data and driving the trapezoidal commutation logic.
LPC1768
BLDC Driver
Same as above
Phase A
Phase B
Phase C
LPC1768 BLDC Motor Driver
Double Bearing Mount Piece
Anti Gravity 4006
VNH 5019
ACS711 Current Sensors
A
B

A) Nucleo 144 Board and the Post Hub.
B) Hopper platform. Leg not attached.

Figure 5.6: Architectural overview of the system is shown. Matlab running on the mission PC sends the trigger to start the hopping controller and it captures data for a pre determined period of time. The Raibert controller is implemented inside Nucleo 144 along with measurements from three encoders for obtaining hopper orientation/position. BLDC drivers are implemented on seperate microcontroller boards, which is LPC1768, for fast execution of BLDC phase logics. The panel in the middle shows the hopper body CAD model. For clarity, I mark microcontroller, current sensing and driver boards. I also show the double bearing mount piece connecting the body to the post and the BLDC motors. The right panel shows a photograph of the overall testing platform.

spring and damping coefficients in (5.4) and (5.5) are actually generated by the actuator to achieve a specific impedance, which increases the power input to the system. This distinction is well established in robotics[79] and usually it is believed that passive dynamics increases efficiency at the cost of making the system less re-configurable and vice versa for active impedance. Interestingly, active and passive components of locomotion has also been observed in insects[19], but evidence is inconclusive whether it is used for efficiency or for damping the motion during high frequency impacts.

The efficiency effect of active/passive impedance in the simple vertical example is shown in Figure 5.5. In this figure, the cyan curve represents the power to generate thrust during passive case and magenta curves show the effect of active impedance on energy usage. The flows are numerically computed using $m = 1$ kg, $g = 9.81$ m/s^2, $r = 0.07$ m , $k = 200$ N/m, $b = 1$ N/(m/s), $F_{in} = 40$ N and $T_f = 50$ ms (thrust period).

RAIBERT CONTROLLER

The real model of jumping and moving is more complex than the simple vertical hopping explained in the previous section. The seminal Raibert controller considers both the vertical hopping and the stepping control of a two link RP manipulator. While the full dynamics of such a system is outside the scope of this chapter, for the interested reader the work by Ghigliazza et al.[25] is a good starting point to discover more about such dynamics.

Here, I go over the two governing equations of the Raibert controller since they are embedded inside the control architecture and give us an idea about the active versus passive dynamics of different leg designs. The Raibert Control inherently switches between different controllers (to generate thrust, to maintain body orientation, and to maintain linear speed) depending on the state of the system.

The controller running during the flight phase regulates the leg angle so that the foot is positioned at a neutral location for initiating the next jump cycle. This control rule is as follows:

$$x_n = \frac{\dot{x} T_{st}}{2} + k_{pf}(\dot{x_d} - \dot{x}), \tag{5.6}$$

where x_n denotes the desired neutral position of the foot (assumed to be a point at the tip of the five-bar leg mechanism between links 3 and 4), $\dot{x}$ is the horizontal speed of the hopper body, T_{st} is the stance period from the previous jump, k_{pf} is a gain coefficient regulating the forward and backward acceleration. A tip position away from the body center point would decelerate and closer to the body would accelerate the hopper. $\dot{x_d}$ denotes the desired forward speed. Inverse kinematics solutions are performed in real time to obtain the required ϑ_2 and ϑ_5 values from the x_n position. Note that the radial component can be set as a constant number indicating virtual RP leg length (for a rigid leg) or it can be set to the neutral length of the leg spring (for a compliant leg).

During the stance phase, a separate controller stabilizes the body orientation via the friction cone at the ground contact. The following control rule is used during stance:

$$\mathcal{T} = k_{pt}(\gamma_d - \gamma) + k_{dt}\dot{\gamma}, \tag{5.7}$$

where $\mathcal{T}$ is the torque required to stabilize the hopper body. It is generated by the revolute joint in the RP manipulator. The gains k_{pt} and k_{dt} are proportional and derivative terms acting on body angle γ and its derivative $\dot{\gamma}$. Last, γ_d is the desired body angle. Usually, it is picked as zero.

For the rigid leg experiments, I use an active impedance term composed of spring and damping components acting along a virtual leg connecting the five-bar tip with its mid-base position. This active impedance (normal) component along with the body angle control (tangential) component can be passed to the mechanism Jacobian to obtain required joint torques.

5.3 SYSTEM OVERVIEW

This section explains electrical, mechanical and software architectures of the hopper platform in detail. In essence it is a smaller version of the original Raibert hopper platform. My design philosophy is to replicate it using modern microcontroller architectures with mostly off-the-shelf components for ease of replication. Its mechanical components are either laser-machined or made from foldable structures for the same reason.

HOPPER PLATFORM

The overall platform comprises three components. A PC running a MATLAB script, which triggers the experiment and is used for data collection and visualization. The serial communication port transmits data back and forth with the main hopper controller. The telemetry, which contains encoder readings, motor currents and other mission critical data, is broadcast at 1 kHz to the MATLAB script. In total, this data consists of 44 bytes and occupies %17 of the serial bandwidth which runs at 2 MHz.

The second component, where the main hopper controller is attached, is the post as shown in the right panel of Figure 5.6. The post measures three angles of the robot body. They represent the body orientation (rotation around the bar connecting the post and the hopper platform), position of the hopper (running in a circle around the post), and another angle measurement to compute the height of the hopper. All encoders, including the ones attached to BLDC motor shafts, in the system are AS5048A. They are 14-Bit absolute encoders with SPI connection. I choose SPI over I2C due to the known number of connected devices and low overhead in package sizes, with the aim to optimize for speed, precision, and accuracy. The length of the rod connecting the post to the hopper body is 475 mm. The neutral length of the leg is chosen between 60 and 100 mm. A thorough discussion on leg length to rod length for meaningful approximation to running in a 2-D plane can be found in the literature[97]. Finally, contacts are detected via a 3-D soft-bodied force sensor, whose details can be found in our prior work[21].

The main hopping controller is embedded inside a Nucleo 144 board powered by an STM32F767ZI chip clocked at 216 MHz. It is attached to the post base and generates PWM signals, which are passed to motor drivers over SPI at 1 kHz. The Nucleo 144 board handles communications with the PC, post encoders, and motor drivers as shown in Figure 5.6. In addition to encoder measurement, the motor currents are passed to the Nucleo 144 board through analog-to-digital converters provided by the STM32 chip.

Brushless DC Motor Drivers

The third component is the brushless DC (BLDC) motor and its driver. There are two BLDC motors (T-Motors Anti Gravity 4006) on the system, attached to the robot body. They directly drive the upper links of the five-bar mechanism. I use six VNH5019 drivers (12 A continuous supply at 24 V) to drive the gate logic of the two motors. An LPC1768 microcontroller board running at 96 MHz sets the correct motor state based on the absolute encoder readings attached to the motor shaft. The currents drawn by motors are measured by sensors attached in series between the power supply and the VNH5019 drivers.

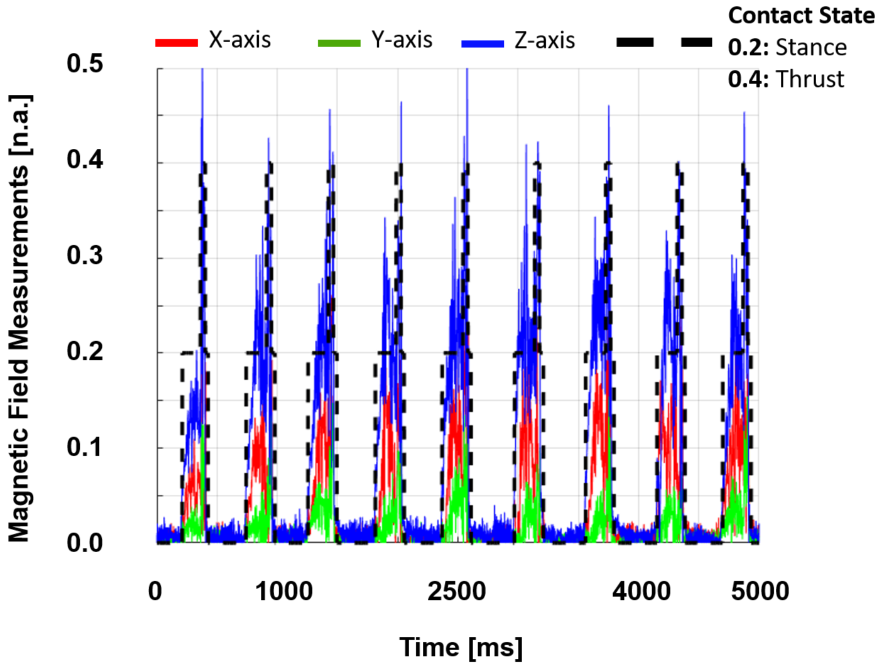

Figure 5.7: Contact detection results via soft force sensor. The red, green and blue curves represents not filtered magnetic filter measurements normalized to 1.0, in x, y and z axes, respectively. Dashed black edges represent contact state. X-Axis represents time in millisecond. Result is from the optimized foldable leg design experiments.

Typical commutation schemes for BLDC consist of trapezoidal, sinusoidal, and field oriented control. In this platform design, I use trapezoidal commutation due to its simplicity in implementation. Since I use the same scheme to analyze different leg designs, any inefficiency coming from the BLDC driver is expected to have a similar effect on all leg performances. A thorough analysis of different BLDC drive schemes is made by Lee et al.[40].

Table 5.1: Comparison between the three different cases tested

Experiment Name	Hopper Mass [g]	Leg Mass [g]	Average System Energy [J]	Average Input Energy [J]	$\mu = E_{sys}/E_{in}$
Not Opt. Rigid	350	74.2	0.09 ± 0.010	13.04 ± 1.55	0.69
Not Opt. Foldable	350	23.9	0.08 ± 0.007	5.88 ± 0.73	1.36
Opt Foldable	350	22.1	0.16 ± 0.027	7.97 ± 2.54	2.00

5.4 EXPERIMENT RESULTS

The performance of Raibert controller depends heavily on contact detection and separating different states of the motion from one another. In my experiments, all ground contacts were detected precisely by our custom tri-axial soft-bodied force sensors. Contact detection results using these sensors are shown in Figure 5.7. In this figure, it is apparent that the z-axis force measurements (in blue, representing vertical force) are more prominent than other axes. This is expected as this axis corresponds to forces due to the whole weight of the robot and the impact forces. The red curve represents forces in the horizontal direction, it represents shear forces. The green curve should theoretically be zero, because this is a 2-D hopper. However, some deviation is observed, which may be due to a slight angle of the body as it makes contact with the ground (i.e. the connecting rod not being strictly horizontal but moving in a circular arc around the post pivot). It can be seen from dashed black lines that this data can be utilized with no filtering to track contact states.

I conduct vertical hopping experiments by setting the desired forward speed for the Raibert controller to zero. The same approach is applied to three different leg designs to compare their performance experimentally: rigid, foldable, and an optimized iteration of the foldable leg. I measure the robot height and its numerical derivative through the absolute encoder attached to the rod, which connects the hopper body to the post, for obtaining kinetic and potential energies in each experiment. Current sensors attached to the BLDC motor drivers and the voltage level of the power supply are used to measure the power drawn by the system in each one of the experiments. Results of these measurements for 2.5 s of experiments can be seen in Figure 5.8. The sum of kinetic and potential energies and their individual curves are similar for all experiments.

The frequency of jumps is similar in rigid and manually designed foldable leg experiments (7 jumps in 2.5 s) and slightly lower (5 jumps in 2.5 s) in the optimized foldable design, mostly due to changes in the dynamic behaviour via the introduction of compliance and kinematics of the optimized five-bar. PID control gains are system dependent and it is hard to reuse them. However, their relative values may be of value. For the stance phase k_p being tuned as 1200 for the rigid leg, as 500 in foldable leg, and as 400 in the optimized the foldable leg indicate the level of effort required to apply thrust to the robot with each leg prototype for repeated hopping. The governing k_p gain in both foldable designs was similar whereas k_p in the rigid leg was significantly larger. Note that this choice is required for the rigid leg due to the lack of passive energy storage capacity. Therefore all the impedance during stance, along with the thrust force, needs to be generated actively by BLDC motors. On the other hand the foldable designs can store the kinetic energy at the impact due to their embedded elasticity at their joints. This storing capacity results in lower k_p gains during stance mode, which significantly reduces the power consumed in the foldable designs. The power consumption of both BLDC motors on each experiment can be seen on the magenta curves in Figure 5.8 and the right-hand-side y-axis represent power consumed at each control cycle in watts. Significant power consumption during active impedance and thrust phases in the rigid design can be observed when compared with the foldable counterpart.

A surprising observation is the near-constant energy consumption during flight phases of the foldable legs. This is due to slight position differences between the neutral length of the compliant leg and the programmed reference point. It tells us that the leg is consuming energy to stay in its ballistic flight configuration. Note that this phenomenon is not observed in the rigid leg, whose energy curves return near zero during the flight phase.

A skeptic might wonder whether extra power consumption of foldable legs during flight can counterbalance their benefits during the stance phase. That is not the case as can be observed in the bottom row of Figure 5.8. Using average jump period timings (flight and stance phase periods added together) in each experiment I compute the moving average energy input to the each system and used this number to compute the efficiency, as $\mu = E_{system}/E_{Input}$, at each control cycle. Foldable designs outperform rigid legs consistently. Significant parameters and results of the experiments are tabulated in Table 5.1.

The efficiency curves are periodic. At the bottom-most point of the jump, vertical speed and position are zero, driving the system energy to zero, too. However in the foldable case the spring effect of the leg helps the motors lift the body upwards. The spring energy in the foldable designs is not included in the plots since this is an internal potential energy stored within the system. The overall efficiency of the mechanism is between $\%0.05$ and $\%3.25$. This value is lower compared to the efficiency of the human muscular system measured as $\%20.0 - 30.0$[73]. Nevertheless the improvement of the compliant leg design over the rigid counterpart persists.

Snapshots from a single jump period along with time series data of vertical position and speed are shown in Figure 5.9 for the optimized foldable leg prototype. Vertical position, which is the solid blue curve, follows a periodic trajectory. At time instance t_0 the robot is under free fall. The height change in this phase behaves like a parabola and there is an approximately linear decrease in the speed, shown as a solid red curve. As the robot is entering stance phase depicted in t_1, the linear decrease in speed is disturbed due to complex ground contact dynamics. As the robot leg compresses the height decreases as well. Shortly after the body up speed changes sign, thrust period is entered as shown in t_2. At this point, a small amount of power is injected to recover the lost energy from the previous cycle. Due to passive compliance of the leg design, speed gain in stance period right before thrust is generated by the leg itself. In t_3, hopper reaches the maximum flight height and enters the next jump cycle.

5.5 Discussion

This chapter introduced a new foldable, fiberglass-reinforced, and compliant mechanism design to be used as 2-DoF legs in robotic platforms as the main contribution. Integrating this new design and fabrication methodology with a well-known control problem in robotics, that is the Raibert hopping controller, has shown that this new design is relevant to the existing body of robotics knowledge. Due to the uncertain nature of research and difficulty of creating new and useful machines, there is an abundance of conceptual robots with no real application. My leg design has shown improved performance in a canonical robotic system demonstrating a use case for new design and manufacturing methods that embrace soft materials and body compliance in general.

As a secondary contribution, I describe a simple and effective hopping platform, its electrical details, and controller architecture. I use an off-the-shelf microcontroller and sensor boards along with rapid-prototyped parts, making the design accessible to others in this field. I also provide an algorithmic approach to designing desired workspaces for five-bar mechanisms with well behaved Jacobians, which is especially important for flexural folded mechanisms under heavy periodic loads. I consider these to be valuable technical contributions.

The comparison for efficiency is made between a rigid leg design and a folded-compliant leg design. The rigid leg is designed with acrylic and it does not contain any spring elements. It is reasonable to expect that a rigid leg design with torsional spring at joints (or a linear spring connecting multiple joints/points on the mechanism) would increase efficiency similar to the folded design. However, this efficiency increase would come with more detailed/potentially-complex mechanical design and with additional weight. For the scope of the compliant hopper leg work, we use the non-compliant rigid leg design as a benchmark for showing efficiency increase.

One challenge I encountered was folding the fiberglass reinforced sheets with the liquid resin. Even though it is not time consuming, this process takes significant manual experience to be completed properly. I believe additive manufacturing, especially recent techniques developed for flexible, soft, and multi-material components will make it much easier to build similar designs[100].

Force sensor shielding was another challenge. Contact detection threshold for the force sensor would change under external effects from ferromagnetic materials and this difference could cause sensor failure. Another challenge related to magnetic sensor was small cuboid magnets flipping inside soft substrate during rapid hopping movements. This was solved by wrapping the magnet with a small acrylic frame and embedding the composite inside the soft silicone.

As for future work and final remarks I would like to discuss three points. First one is agility in robotic design. Soft and compliant robotics grew out of the very real need to make robots more like natural organisms: less rigid components, more mechanical compliance, multi-material links/joints, and variable stiffness capabilities. The result of this endeavour has introduced novel modes of locomotion, grasping and more natural physical behaviours by the growing soft robotics community. Occasionally what was deemed algorithmically difficult has been solved by mechanical properties of compliant mechanisms.

One way to solve the agility problem is to change rigid parts with softer or more flexible designs. In that case using previous controllers and theories are important for creating valuable use cases and verifying experimentally obtained results in comparison with traditional approaches that use rigid mechanisms. The future, unfortunately, might not be like the past. Instead of writing down exact equations for describing motions of dynamic systems, we might want to anchor them in strong theories like for vertical hopping and develop new control algorithms that embrace body elasticity.

Second potential future work would be programmable compliance. Passive compliance not being reconfigurable is a limitation of my current work. However, through material optimization and precise torque control via BLDC motors, the problem of non-reconfigurable compliance can be addressed. More advanced drive technologies such as field oriented control would allow the system to be programmed to different stiffness values. If improved energy efficiency is needed, the system should be driven near its neutral setting. To this end, advanced material characterization of fiber reinforced leg design and automating its manufacture process would be important the next steps.

Last direction for future work is incremental improvements over the current compliant design. Scaling up the mechanism is an interesting idea. It would be trivial to increase link lengths by a couple of times their current lengths but developing folded structures for a mechanisms that is more than a single magnitude of order larger would be complex due to detailed crease patterns for reinforcing extra material. Performing life-cycle tests on mechanisms and comparing different material compositions on overall mechanism compliance would also be interesting areas for research.

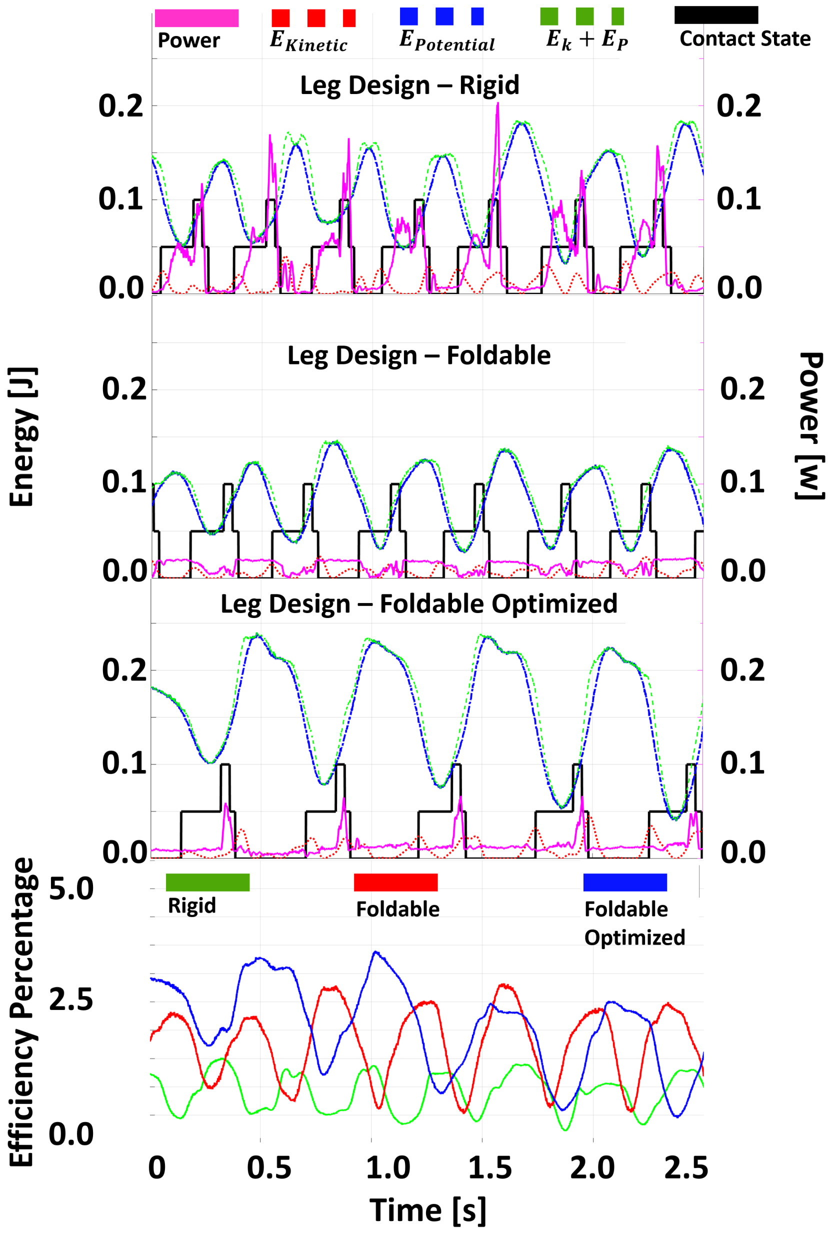

Figure 5.8: Energy (sum of kinetic and potential) and power input to the system when driven with each leg design is shown on top three rows. The last row compares efficiency of three leg designs. I use a moving average with a window size equivalent to average jump period to compute energy input from power values computed at each control cycle. Solid black edges indicate ballistic flight, stance phase and thrust phase.

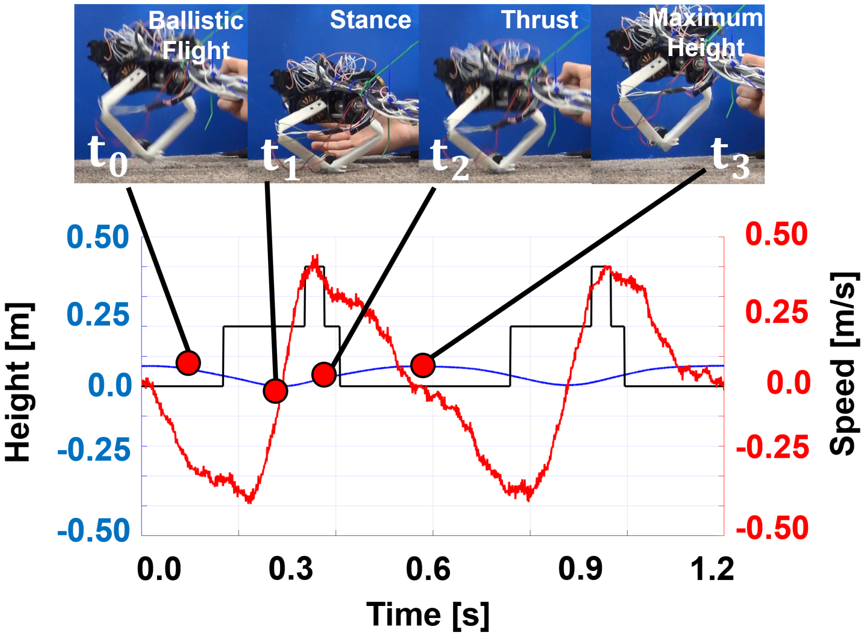

Figure 5.9: Phase sequence during a single jump with the foldable optimized leg is shown. The sequences demonstrate the ballistic flight before touchdown t_0, leg being loaded under weight of the hopper t_1, thrust generating energy for the next jump cycle t_2 and maximum jump height at the next jump cycle t_3. The x-axis represent time in s, the left y-axis is hopper height in m and the right y-axis represents hopper speed in m/s. The red and blue curves represent height and speed, respectively. Finally, the solid black edges represent jump phases.

6

Conclusion

Throughout the thesis, I wrote about most of the work on material compliance I have done during my PhD. One paper I omit was my collaborative work on soft biological tissue palpation[8], where I created a soft actuation and sensing module to automatically detect potentially cancerous tissue by measuring contact stiffness. By the time I completed my work on the curvature sensor, soft module control, and force sensing, I had gained significant practical knowledge on how to manufacture and build highly flexible/stretchable mechatronic sensors, actuators and corresponding control systems aimed to be used with robots.

I was interested in continuum manipulator control and design. However, I saw a number of shortcomings in the existing octopus-inspired manipulation approaches. I also thought replicating the joint-linkage structure with soft modules was not the best way to utilize these mechanisms.

I already knew about Raibert's work from my previous experience with ZMP-based robot walkers. My hunch was that his control ideas, which naturally embrace compliance, could create a connection to soft-bodied robot design. While reading through Raibert's book[75], I was inspired by his forecast on how a flexible bodied legged robot could potentially use its flexibility to achieve cheetah-like running with extremely simple controllers. Very simply, one can imagine a virtual leg connecting the middle of the curved body to the touch point of the legs. It is important to remember that at each stance, feet are positioned close to one another so that they all act like a single leg. In theory, such a mechanism would be able to replicate the original single leg hopper mechanism.

My original goal was to create an autonomous walking system that utilized my knowledge from soft and origami inspired robotics. However, it turned out that building a complete running system from scratch with such novel soft robotic design elements is a little too much for a single PhD thesis. So I pivoted to working on a single leg design and how legged robotics can benefit from it by making it quite compliant and lightweight using manufacturing techniques that can be found in the previous chapter of my thesis. Moreover, the leg mechanisms demonstrated the sensing quality of my tri-axial force sensors, discussed in the earlier chapters. Interestingly, researchers in[20] built a quadruped mechanism using standard mechanical components. Therefore next steps along this line could be creating compliant body motions with multi-material design patterns and anchoring the motion trajectories of them in simpler theories of running.

Robotics have improved along with computer science over the past half decade and there is an overemphasis in robotics community on finding algorithmic solutions to physical problems. My research tries to balance this trend by putting emphasis on smart mechanism design. Especially, my work on compliant leg mechanism experimentally shows that we should be reasoning about material properties and algorithms simultaneously, while designing agile robots. The result of this multi-disciplinary way of thinking is increased mechanical efficiency. I think the trend to make robots more agile will continue and we will see complex mechanisms handling complicated tasks in the real world with seamless effort. This kind of future will require smart mechanical design combined with good algorithms to exploit mechanism dynamics efficiently.

References

[1] (2001). Index. In E. P. Furlani (Ed.), *Permanent Magnet and Electromechanical Devices*, Electromagnetism (pp. 513 – 518). San Diego: Academic Press.

[2] Agheli, M., Faal, S. G., Chen, F., Gong, H., & Onal, C. D. (2014). Design and fabrication of a foldable hexapod robot towards experimental swarm applications. In *2014 IEEE International Conference on Robotics and Automation (ICRA)* (pp. 2971–2976).

[3] Beal, D. N., Hover, F. S., Triantafyllou, M. S., Liao, J. C., & Lauder, G. V. (2006). Passive propulsion in vortex wakes. *Journal of Fluid Mechanics*, 549, 385–402.

[4] Beccai, L., Roccella, S., Ascari, L., Valdastri, P., Sieber, A., Carrozza, M. C., & Dario, P. (2008). Development and experimental analysis of a soft compliant tactile microsensor for anthropomorphic artificial hand. *IEEE/ASME Transactions on Mechatronics*, 13(2), 158–168.

[5] Belke, C. H. & Paik, J. (2017). Mori: A modular origami robot. *IEEE/ASME Transactions on Mechatronics*, 22(5), 2153–2164.

[6] Brown, E., Rodenberg, N., Amend, J., Mozeika, A., Steltz, E., Zakin, M. R., Lipson, H., & Jaeger, H. M. (2010). Universal robotic gripper based on the jamming of granular material. *Proceedings of the National Academy of Sciences*, 107(44), 18809–18814.

[7] Butterfass, J., Grebenstein, M., Liu, H., & Hirzinger, G. (2001). Dlr-hand ii: next generation of a dextrous robot hand. In *Proceedings 2001 ICRA. IEEE International Conference on Robotics and Automation (Cat. No.01CH37164)*, volume 1 (pp. 109–114 vol.1).

[8] Campisano, F., Ozel, S., Ramakrishnan, A., Dwivedi, A., Gkotsis, N., Onal, C. D., & Valdastri, P. (2017). Towards a soft robotic skin for autonomous tissue palpation. In *2017 IEEE International Conference on Robotics and Automation (ICRA)* (pp. 6150–6155).

[9] Chen, T., Goodfellow, I. J., & Shlens, J. (2015). Net2net: Accelerating learning via knowledge transfer. *CoRR*, abs/1511.05641.

[10] Cho, C. & Ryuh, Y. (2016). Fabrication of flexible tactile force sensor using conductive ink and silicon elastomer. *Sensors and Actuators A: Physical*, 237(C), 72–80.

[11] Chollet, F. et al. (2015). Keras. **`https://github.com/fchollet/keras`**.

[12] Cianchetti, M., Arienti, A., Follador, M., Mazzolai, B., Dario, P., & Laschi, C. (2011). Design concept and validation of a robotic arm inspired by the octopus. *Materials Science and Engineering: C*, 31(6), 1230 – 1239. Principles and Development of Bio-Inspired Materials.

[13] Clark, J. J. (1988). A magnetic field based compliance matching sensor for high resolution, high compliance tactile sensing. In *Proceedings. 1988 IEEE International Conference on Robotics and Automation* (pp. 772–777 vol.2).

[14] Dahiya, R. S., Metta, G., Valle, M., & Sandini, G. (2010). Tactile sensing—from humans to humanoids. *IEEE Transactions on Robotics*, 26(1), 1–20.

[15] De, A. & Koditschek, D. E. (2015). The penn jerboa: A platform for exploring parallel composition of templates. *CoRR*, abs/1502.05347.

[16] der, S. A. J. v. & Schumacher, J. M. (1999). *Introduction to Hybrid Dynamical Systems*. Berlin, Heidelberg: Springer-Verlag.

[17] Dobrzynski, M. K., Pericet-Camara, R., & Floreano, D. (2011). Contactless deflection sensor for soft robots. In *2011 IEEE/RSJ International Conference on Intelligent Robots and Systems* (pp. 1913–1918).

[18] Dollar, A. M. & Howe, R. D. (2006). A robust compliant grasper via shape deposition manufacturing. *IEEE/ASME Transactions on Mechatronics*, 11(2), 154–161.

[19] Dudek, D. M. & Full, R. J. (2006). Passive mechanical properties of legs from running insects. *Journal of Experimental Biology*, 209(8), 1502–1515.

[20] Duperret, J. & Koditschek, D. E. (2017). Empirical validation of a spined sagittal-plane quadrupedal model. In *Proceedings - IEEE International Conference on Robotics and Automation* (pp. 1058–1064).

[21] Dwivedi, A., Ramakrishnan, A., Reddy, A., Patel, K., Ozel, S., & Onal, C. D. (2018). Design, modeling, and validation of a soft magnetic 3-d force sensor. *IEEE Sensors Journal*, 18(9), 3852–3863.

[22] Erbatur, K., Seven, U., Taşkiran, E., Koca, □., Yilmaz, M., Ünel, M., Kiziltaş, G., Sabanovic, A., & Onat, A. (2009). Suralp: A new full-body humanoid robot platform. In *2009 IEEE/RSJ International Conference on Intelligent Robots and Systems* (pp. 4949–4954).

[23] Gafford, J., Doshi-Velez, F., Wood, R., & Walsh, C. (2016). Machine learning approaches to environmental disturbance rejection in multi-axis optoelectronic force sensors. *Sensors and Actuators A: Physical*, 248, 78 – 87.

[24] Galloway, K. C., Becker, K. P., Phillips, B., Kirby, J., Licht, S., Tchernov, D., Wood, R. J., & Gruber, D. F. (2016). Soft robotic grippers for biological sampling on deep reefs. *Soft Robotics*, 3(1), 23–33. PMID: 27625917.

[25] Ghigliazza, R., Altendorfer, R., Holmes, P., & Koditschek, D. (2005). A simply stabilized running model. *SIAM Review*, 47(3), 519–549.

[26] Hannan, M. W. & Walker, I. D. (2003). Kinematics and the implementation of an elephant's trunk manipulator and other continuum style robots. *Journal of robotic systems*, 20 2, 45–63.

[27] Holling, H., Boland, H., & Russ, E. (1961). Investigation of arterial obstruction using a mercury-in-rubber strain gauge. *American Heart Journal*, 62(2), 194 – 205.

[28] Homberg, B. S., Katzschmann, R. K., Dogar, M. R., & Rus, D. (2015). Haptic identification of objects using a modular soft robotic gripper. In *2015 IEEE/RSJ International Conference on Intelligent Robots and Systems (IROS)* (pp. 1698–1705).

[29] Ilievski, F., Mazzeo, A. D., Shepherd, R. F., Chen, X., & Whitesides, G. M. (2011). Soft robotics for chemists. 50, 1890–1895.

[30] Jamone, L., Metta, G., Nori, F., & Sandini, G. (2006). James: A humanoid robot acting over an unstructured world. In *2006 6th IEEE-RAS International Conference on Humanoid Robots* (pp. 143–150).

[31] Jamone, L., Natale, L., Metta, G., & Sandini, G. (2015). Highly sensitive soft tactile sensors for an anthropomorphic robotic hand. *IEEE Sensors Journal*, 15(8), 4226–4233.

[32] Katragadda, R. B. & Xu, Y. (2007). A novel intelligent textile technology based on silicon flexible skins. In *2007 IEEE 20th International Conference on Micro Electro Mechanical Systems (MEMS)* (pp. 301–304).

[33] Khondoker, M. A. H. & Sameoto, D. (2016). Fabrication methods and applications of microstructured gallium based liquid metal alloys. *Smart Materials and Structures*, 25(9), 093001.

[34] Kim, K., Lee, K. R., Kim, W. H., Park, K.-B., Kim, T.-H., Kim, J.-S., & Pak, J. J. (2009). Polymer-based flexible tactile sensor up to 32×32 arrays integrated with interconnection terminals. *Sensors and Actuators A: Physical*, 156(2), 284 – 291.

[35] Kim, S., Laschi, C., & Trimmer, B. (2013). Soft robotics: a bioinspired evolution in robotics. *Trends in Biotechnology*, 31(5), 287 – 294.

[36] Koditschek, D. E. & Bühler, M. (1991). Analysis of a simplified hopping robot. *The International Journal of Robotics Research*, 10(6), 587–605.

[37] Kramer, R. K., Majidi, C., Sahai, R., & Wood, R. J. (2011a). Soft curvature sensors for joint angle proprioception. In *2011 IEEE/RSJ International Conference on Intelligent Robots and Systems* (pp. 1919–1926).

[38] Kramer, R. K., Majidi, C., & Wood, R. J. (2011b). Wearable tactile keypad with stretchable artificial skin. In *2011 IEEE International Conference on Robotics and Automation* (pp. 1103–1107).

[39] Ledermann, C., Wirges, S., Oertel, D., Mende, M., & Woern, H. (2013). Tactile sensor on a magnetic basis using novel 3d hall sensor - first prototypes and results. In *2013 IEEE 17th International Conference on Intelligent Engineering Systems (INES)* (pp. 55–60).

[40] Lee, S. (2009). A comparison study of the commutation methods for the three-phase permanent magnet brushless dc motor.

[41] Li, C., Wu, P., Lee, S., Gorton, A., Schulz, M. J., & Ahn, C. H. (2008). Flexible dome and bump shape piezoelectric tactile sensors using pvdf-trfe copolymer. *Journal of Microelectromechanical Systems*, 17(2), 334–341.

[42] Lin, H.-T., Leisk, G. G., & Trimmer, B. (2011). Goqbot: a caterpillar-inspired soft-bodied rolling robot. *Bioinspiration and Biomimetics*, 6(2), 026007.

[43] Lipomi, D., Vosgueritchian, M., Tee, B., L Hellstrom, S., Lee, J., Fox, C., & Bao, Z. (2011). Skin-like pressure and strain sensors based on transparent elastic films of carbon nanotubes. 6, 788–92.

[44] Liu, Y., Han, H., Liu, T., Yi, J., Li, Q., & Inoue, Y. (2016). A novel tactile sensor with electromagnetic induction and its application on stick-slip interaction detection. *Sensors*, 16 4, 430.

[45] Luo, M., Agheli, M., & Onal, C. D. (2014a). Theoretical modeling and experimental analysis of a pressure-operated soft robotic snake. *Soft Robotics*, 1(2), 136–146.

[46] Luo, M., Pan, Y., Skorina, E. H., Tao, W., Chen, F., Ozel, S., & Onal, C. D. (2015). Slithering towards autonomy: a self-contained soft robotic snake platform with integrated curvature sensing. *Bioinspiration and Biomimetics*, 10(5), 055001.

[47] Luo, M., Tao, W., Chen, F., Khuu, T. K., Ozel, S., & Onal, C. D. (2014b). Design improvements and dynamic characterization on fluidic elastomer actuators for a soft robotic snake. In *2014 IEEE International Conference on Technologies for Practical Robot Applications (TePRA)* (pp. 1–6).

[48] Majidi, C. (2014). Soft robotics: A perspective—current trends and prospects for the future. *Soft Robotics*, 1(1), 5–11.

[49] Majidi, C., Kramer, R., & Wood, R. J. (2011). A non-differential elastomer curvature sensor for softer-than-skin electronics. *Smart Materials and Structures*, 20(10), 105017.

[50] Marchese, A. D., Katzschmann, R. K., & Rus, D. (2014a). Whole arm planning for a soft and highly compliant 2d robotic manipulator. In *2014 IEEE/RSJ International Conference on Intelligent Robots and Systems* (pp. 554–560).

[51] Marchese, A. D., Komorowski, K., Onal, C. D., & Rus, D. (2014b). Design and control of a soft and continuously deformable 2d robotic manipulation system. *2014 IEEE International Conference on Robotics and Automation (ICRA)*, (pp. 2189–2196).

[52] Marchese, A. D., Onal, C. D., & Rus, D. (2014c). Autonomous soft robotic fish capable of escape maneuvers using fluidic elastomer actuators. *Soft Robotics*, 1(1), 75–87. PMID: 27625912.

[53] Margheri, L., Laschi, C., & Mazzolai, B. (2012). Soft robotic arm inspired by the octopus: I. from biological functions to artificial requirements. *Bioinspiration and Biomimetics*, 7(2), 025004.

[54] Mazzolai, B., Margheri, L., Cianchetti, M., Dario, P., & Laschi, C. (2012). Soft-robotic arm inspired by the octopus: Ii. from artificial requirements to innovative technological solutions. 7, 025005.

[55] McGeer, T. (1990). Passive dynamic walking. *The International Journal of Robotics Research*, 9(2), 62–82.

[56] Menguc, Y., Park, Y.-L., Pei, H., Vogt, D., M. Aubin, P., Winchell, E., Fluke, L., Stirling, L., Wood, R., & Walsh, C. (2014). Wearable soft sensing suit for human gait measurement. 33, 1748–1764.

[57] Merlet, J. P. (2007). Jacobian, manipulability, condition number and accuracy of parallel robots. In S. Thrun, R. Brooks, & H. Durrant-Whyte (Eds.), *Robotics Research* (pp. 175–184). Berlin, Heidelberg: Springer Berlin Heidelberg.

[58] Monteiro, C., Ferreira, M., Silva, S., Kobelke, J., Schuster, K., Bierlich, J., & Frazão, O. (2016). Fiber fabry-perot interferometer for curvature sensing. *Photonic Sensors*, 6.

[59] Nicholls, H. R. & Lee, M. H. (1989). A survey of robot tactile sensing technology. *The International Journal of Robotics Research*, 8(3), 3–30.

[60] Nie, Q. & Sup, F. C. (2017). A soft four degree-of-freedom load cell based on the hall effect. *IEEE Sensors Journal*, 17(22), 7355–7363.

[61] Noda, K., Hoshino, K., Matsumoto, K., & Shimoyama, I. (2006). A shear stress sensor for tactile sensing with the piezoresistive cantilever standing in elastic material. *Sensors and Actuators A: Physical*, 127(2), 295 – 301. MEMS 2005 Special Issue.

[62] Norton, R. (2004). *Design of Machinery: An Introduction to the Synthesis and Analysis of Mechanisms and Machines*. McGraw-Hill series in mechanical engineering. McGraw-Hill Higher Education.

[63] of Automotive Engineers., S. (1969-01-01). Exploring the potential of a quadruped. *S.A.E. transactions.*, 78, 836,843.

[64] Onal, C. D. & Rus, D. (2012). A modular approach to soft robots. In *2012 4th IEEE RAS EMBS International Conference on Biomedical Robotics and Biomechatronics (BioRob)* (pp. 1038–1045).

[65] Onal, C. D. & Rus, D. (2013). Autonomous undulatory serpentine locomotion utilizing body dynamics of a fluidic soft robot. *Bioinspiration and biomimetics*, 8 2, 026003.

[66] Onal, C. D., Tolley, M. T., Wood, R. J., & Rus, D. (2015). Origami-inspired printed robots. *IEEE/ASME Transactions on Mechatronics*, 20(5), 2214–2221.

[67] Onal, C. D., Wood, R. J., & Rus, D. (2011). Towards printable robotics: Origami-inspired planar fabrication of three-dimensional mechanisms. In *2011 IEEE International Conference on Robotics and Automation* (pp. 4608–4613).

[68] Ozel, S., Keskin, N. A., Khea, D., & Onal, C. D. (2015). A precise embedded curvature sensor module for soft-bodied robots. *Sensors and Actuators A: Physical*, 236, 349 – 356.

[69] Ozel, S., Skorina, E. H., Luo, M., Tao, W., Chen, F., Pan, Y., & Onal, C. D. (2016). A composite soft bending actuation module with integrated curvature sensing. In *2016 IEEE International Conference on Robotics and Automation (ICRA)* (pp. 4963–4968).

[70] Park, Y.-L., Chau, K., Black, R. J., & Cutkosky, M. R. (2007). Force sensing robot fingers using embedded fiber bragg grating sensors and shape deposition manufacturing. *Proceedings 2007 IEEE International Conference on Robotics and Automation*, (pp. 1510–1516).

[71] Peirs, J., Clijnen, J., Reynaerts, D., Brussel, H. V., Herijgers, P., Corteville, B., & Boone, S. (2004). A micro optical force sensor for force feedback during minimally invasive robotic surgery. *Sensors and Actuators A: Physical*, 115(2), 447 – 455. The 17th European Conference on Solid-State Transducers.

[72] Quigley, M., Conley, K., P Gerkey, B., Faust, J., Foote, T., Leibs, J., Wheeler, R., & Y Ng, A. (2009). Ros: an open-source robot operating system.

[73] R Umberger, B., G.M. GERRITSEN, K., & Martin, P. (2003). A model of human muscle energy expenditure. 6, 99–111.

[74] Raibert, M. H. (1986). *Legged Robots That Balance*. Cambridge, MA, USA: Massachusetts Institute of Technology.

[75] Raibert, M. H., Brown, H. B., Chepponis, M., Koechling, J., Hodgins, J. K., Dustman, D., Brennan, W. K., Barrett, D. S., Thompson, C. M., Hebert, J. D., Lee, W., & Borvansky, L. (1989). *Dynamically Stable Legged Locomotion (September 1985-September 1989)*. Technical report, Cambridge, MA, USA.

[76] Rygg, L. A. (1893). Mechanical horse. US Patent 491,927.

[77] Santoso, J., Skorina, E. H., Luo, M., Yan, R., & Onal, C. D. (2017). Design and analysis of an origami continuum manipulation module with torsional strength. In *2017 IEEE/RSJ International Conference on Intelligent Robots and Systems (IROS)* (pp. 2098–2104).

[78] Saunders, F., Golden, E., White, R., & Rife, J. (2011). Experimental verification of soft-robot gaits evolved using a lumped dynamic model. 29, 823–830.

[79] Semini, C., Barasuol, V., Boaventura, T., Frigerio, M., Focchi, M., Caldwell, D. G., & Buchli, J. (2015). Towards versatile legged robots through active impedance control. *The International Journal of Robotics Research*, 34(7), 1003–1020.

[80] Shepherd, R. F., Ilievski, F., Choi, W., Morin, S. A., Stokes, A. A., Mazzeo, A. D., Chen, X., Wang, M., & Whitesides, G. M. (2011). Multigait soft robot. *Proceedings of the National Academy of Sciences*.

[81] Skorina, E. H., Luo, M., Ozel, S., Chen, F., Tao, W., & Onal, C. D. (2015). Feedforward augmented sliding mode motion control of antagonistic soft pneumatic actuators. In *2015 IEEE International Conference on Robotics and Automation (ICRA)* (pp. 2544–2549).

[82] Sohgawa, M., Mima, T., Onishi, H., Kanashima, T., Okuyama, M., Yamashita, K., Noda, M., Higuchi, M., & Noma, H. (2009). Tactle array sensor with inclined chromium/silicon piezoresistive cantilevers embedded in elastomer. In *TRANSDUCERS 2009 - 2009 International Solid-State Sensors, Actuators and Microsystems Conference* (pp. 284–287).

[83] Soltero, D. E., Julian, B. J., Onal, C. D., & Rus, D. (2013). A lightweight modular 12-dof print-and-fold hexapod. In *2013 IEEE/RSJ International Conference on Intelligent Robots and Systems* (pp. 1465–1471).

[84] Stamper, R. E., Tsai, L.-W., & Walsh, G. C. (1997). Optimization of a three dof translational platform for well-conditioned workspace. In *Proceedings of International Conference on Robotics and Automation*, volume 4 (pp. 3250–3255 vol.4).

[85] Stokes, A. A., Shepherd, R. F., Morin, S. A., Ilievski, F., & Whitesides, G. M. (2014). A hybrid combining hard and soft robots. *Soft Robotics*, 1(1), 70–74.

[86] Tenzer, Y., Jentoft, L. P., & Howe, R. D. (2014). The feel of mems barometers: Inexpensive and easily customized tactile array sensors. *IEEE Robotics Automation Magazine*, 21(3), 89–95.

[87] Tolley, M. T., Shepherd, R. F., Mosadegh, B., Galloway, K. C., Wehner, M. J., Karpelson, M., Wood, R. J., & Whitesides, G. M. (2014). A resilient , untethered soft robot.

[88] Tomo, T. P., Somlor, S., Schmitz, A., Jamone, L., Huang, W., Kristanto, H., & Sugano, S. (2016a). Design and characterization of a three-axis hall effect-based soft skin sensor. *Sensors*, 16(4).

[89] Tomo, T. P., Wong, W. K., Schmitz, A., Kristanto, H., Somlor, S., Hwang, J., & Sugano, S. (2016b). Snr modeling and material dependency test of a low-cost and simple to fabricate

3d force sensor for soft robotics. In *2016 IEEE/SICE International Symposium on System Integration (SII)* (pp. 428–433).

[90] Torres-Jara, E., Vasilescu, I., & Coral, R. (2006). A soft touch: Compliant tactile sensors for sensitive manipulation.

[91] Trivedi, D., Rahn, C. D., Kier, W. M., & Walker, I. D. (2008). Soft robotics: Biological inspiration, state of the art, and future research. *Appl. Bionics Biomechanics*, 5(3), 99–117.

[92] Valdastri, P., Roccella, S., Beccai, L., Cattin, E., Menciassi, A., Carrozza, M., & Dario, P. (2005). Characterization of a novel hybrid silicon three-axial force sensor. *Sensors and Actuators A: Physical*, 123-124, 249 – 257. Eurosensors XVIII 2004.

[93] Viry, L., Levi, A., Totaro, M., Mondini, A., Mattoli, V., Mazzolai, B., & Beccai, L. (2014). Flexible three-axial force sensor for soft and highly sensitive artificial touch. *Advanced Materials*, 26(17), 2659–2664.

[94] Vogt, D. M., Menguc, Y., Park, Y.-L., Wehner, M. J., Kramer, R., Majidi, C., Jentoft, L. P., Tenzer, Y., Howe, R., & Wood, R. J. (2013a). Progress in soft , flexible , and stretchable sensing systems *.

[95] Vogt, D. M., Park, Y., & Wood, R. J. (2013b). Design and characterization of a soft multi-axis force sensor using embedded microfluidic channels. *IEEE Sensors Journal*, 13(10), 4056–4064.

[96] VUKOBRATOVIĆ, M. & BOROVAC, B. (2004). Zero-moment point — thirty five years of its life. *International Journal of Humanoid Robotics*, 01(01), 157–173.

[97] Westervelt, E. R., Grizzle, J. W., Chevallereau, C., & et al. (2007). Feedback control of dynamic bipedal robot locomotion.

[98] Yang, Y. & Chen, Y. (2018). Innovative design of embedded pressure and position sensors for soft actuators. *IEEE Robotics and Automation Letters*, 3(2), 656–663.

[99] Yi, J., Zhu, X., Zhang, H., Shen, L., & Qiao, X. (2012). Spatial shape reconstruction using orthogonal fiber bragg grating sensor array. *Mechatronics*, 22(6), 679 – 687. Special Issue on Intelligent Mechatronics (LSMS2010 and ICSEE2010).

[100] Yirmibesoglu, O. D., Morrow, J., Walker, S., Gosrich, W., Cañizares, R., Kim, H., Daalkhaijav, U., Fleming, C., Branyan, C., & Menguc, Y. (2018). Direct 3d printing of silicone elastomer soft robots and their performance comparison with molded counterparts. In *2018 IEEE International Conference on Soft Robotics (RoboSoft)* (pp. 295–302).

[101] Yousef, H., Boukallel, M., & Althoefer, K. (2011). Tactile sensing for dexterous in-hand manipulation in robotics—a review. *Sensors and Actuators A: Physical*, 167(2), 171 – 187. Solid-State Sensors, Actuators and Microsystems Workshop.

[102] Youssefian, S., Rahbar, N., & Torres-Jara, E. (2014). Contact behavior of soft spherical tactile sensors. *IEEE Sensors Journal*, 14(5), 1435–1442.